1990

A primitive variable, strongly implicit calculation procedure for two and three-dimensional unsteady viscous flows: applications to compressible and incompressible flows including flows with free surfaces

Kuo-Huey Chen
Iowa State University

INFORMATION TO USERS

The most advanced technology has been used to photograph and reproduce this manuscript from the microfilm master. UMI films the text directly from the original or copy submitted. Thus, some thesis and dissertation copies are in typewriter face, while others may be from any type of computer printer.

The quality of this reproduction is dependent upon the quality of the copy submitted. Broken or indistinct print, colored or poor quality illustrations and photographs, print bleedthrough, substandard margins, and improper alignment can adversely affect reproduction.

In the unlikely event that the author did not send UMI a complete manuscript and there are missing pages, these will be noted. Also, if unauthorized copyright material had to be removed, a note will indicate the deletion.

Oversize materials (e.g., maps, drawings, charts) are reproduced by sectioning the original, beginning at the upper left-hand corner and continuing from left to right in equal sections with small overlaps. Each original is also photographed in one exposure and is included in reduced form at the back of the book.

Photographs included in the original manuscript have been reproduced xerographically in this copy. Higher quality 6" x 9" black and white photographic prints are available for any photographs or illustrations appearing in this copy for an additional charge. Contact UMI directly to order.

UMI

University Microfilms International
A Bell & Howell Information Company
300 North Zeeb Road, Ann Arbor, MI 48106-1346 USA
313/761-4700 800/521-0600

Order Number 9110487

A primitive variable, strongly implicit calculation procedure for two and three-dimensional unsteady viscous flows: Applications to compressible and incompressible flows including flows with free surfaces

Chen, Kuo-Huey, Ph.D.

Iowa State University, 1990

U·M·I
300 N. Zeeb Rd.
Ann Arbor, MI 48106

A primitive variable, strongly implicit calculation procedure for two and three-dimensional unsteady viscous flows: Applications to compressible and incompressible flows including flows with free surfaces

by

Kuo-Huey Chen

A Dissertation Submitted to the
Graduate Faculty in Partial Fulfillment of the
Requirements for the Degree of
DOCTOR OF PHILOSOPHY

Major: Mechanical Engineering

Approved:

Signature was redacted for privacy.

In Charge of Major Work

Signature was redacted for privacy.

For the Major Department

Signature was redacted for privacy.

For the Graduate College

Iowa State University
Ames, Iowa
1990

TABLE OF CONTENTS

LIST OF TABLES

[1] Source: Ref. [86].

LIST OF FIGURES

ACKNOWLEDGMENTS

I wish to express my sincere gratitude to my major advisor, Professor Richard H. Pletcher. I have benefited from the many creative ideas and useful suggestions that he has put forth in my weekly meeting and daily chatting with him. It is because of his able guidance that I could progress in my graduate studies at Iowa State.

I am also grateful to one of my friends, Cherng-Yeu Shen, at Arizona State University for discussions about numerical methods, especially about the SIP scheme. The partial financial support provided by the Mechanical Engineering Department of Iowa State University and the Air Force Office of Scientific Research through Grant No. AFOSR-89-0403 is also appreciated. I am also grateful for support received through a block grant from the Iowa State University Computation Center for part of the computations in this research.

Also, I wish to thank my wife, Hsiufen, for her encouragement and help for my graduate study and for sharing every moment of my anguish during the past five years. Also, I owe much to my daughter, Margaret, and my son, Oliver, for tolerating my absence for most of the weekends and evenings.

NOMENCLATURE

Roman Symbols

d	diameter of the cylinder
e	internal energy per unit mass
f	frequency of the vortex shedding motion
f_{ij}	quantity related to rotation
$\vec{g}$	vector notation for gravity
g_i	index notation for gravity
h_i	index notation for rotation arm
i	ξ or η_1 index of numerical solution
$\vec{i}_\xi$	local unit vector along the ξ direction
$\vec{i}_\eta$	local unit vector along the η direction
$imax$	maximum grid index in ξ or η_1 direction
j	η or η_2 index of numerical solution
$jmax$	maximum grid index in η or η_2 direction
k	η_3 index of numerical solution
k	thermal conductivity
k	iteration index
$kmax$	maximum grid index in η_3 direction

n	time index
$\vec{n}$	local unit normal vector
p	pressure
t	time
p	pressure
q	Cartesian vector of primitive variables
$\vec{q}$	vector notation for heat conduction
rms	root mean square
s	explicit smoothing parameter for free surface
s_{ij}	element of rotation matrix due to free surface angle
u_i	index notation for velocity
x_i	index notation for coordinates
z_i	index notation for transformed coordinates
$A^1_{i,j}$ - $A^9_{i,j}$	element of the coefficient matrix for two-dimensional equations
$A^b_{i,j,k}$ - $A^w_{i,j,k}$	element of the coefficient matrix for three-dimensional equations
ADI	alternating direction implicit
AF	approximate factorization
C_f	skin-friction coefficient
C_L	lift coefficient ($=\frac{lift\ \ force}{\rho V_\infty^2 d \cdot 1}$)
C_p	specific heat
C_p	pressure coefficient
C_1	Sutherland constant
C_2	Sutherland constant

D	hydraulic diameter
E	Cartesian flux vector in x direction
$\hat{E}$	transformed flux vector in x direction
E_l	quantity related to rotation
E_t	total energy per unit volume
F	Cartesian flux vector in y direction
F	free surface height function
$\hat{F}$	transformed flux vector in y direction
F_r	Froude number
J	transformation Jacobian
$[L]$	lower diagonal matrix defined in SIP method
$\vec{M}$	vector notation for momentum equations
M_∞	Mach number
Nu	local Nusselt number
$\bar{N}u$	averaged Nusselt number
$[P]$	auxiliary matrix defined in SIP method
Pr	Prandtl number
$P0$	atmospheric pressure or saturated vapor pressure
Q	external energy
Q	Cartesian vector of conservative variables
$\hat{Q}$	transformed vector of conservative variables
R	gas constant
Re	Reynolds number
SOR	successive overrelaxation

St	Strouhal number $(=\frac{fd}{V_\infty})$
T	temperature
U	contravariant velocity component
$[U]$	upper diagonal matrix defined in SIP method
V	contravariant velocity component
$\vec{V}$	vector notation for velocity
We	Weber number

Greek Symbols

α	partial cancellation parameter in SIP method
α	parameter in the Roberts grid transformation
α_{ij}	element of the transformation matrix
β	parameter in the Roberts grid transformation
$\beta_{cr,li}$	quantity related to rotation
$\beta_{t,li}$	quantity related to rotation
$\beta_{cp,li}$	quantity related to rotation
γ	Ratio of constant specific heats
δ	Kronecker delta function
ϵ	convergence criterion
$\zeta_{i,j}$	metric terms defined in three-dimensional equations
η	vertical transformed coordinate
$\eta_{i,j}$	metric terms defined in three-dimensional equations
$\eta_{i,jj}$	metric terms defined in three-dimensional equations

θ	circumferential direction
Γ	surface tension coefficient
Δ	increment of change
κ	local curvature term at the free surface
κ_1	local curvature term at the free surface
κ_2	local curvature term at the free surface
$\lambda_{i,j,k}$	off-diagonal coefficient terms
λ_{ni}	quantity related to rotation
μ	dynamic viscosity
ν	kinematic viscosity
ξ	horizontal transformed coordinate
ρ	density
σ_1 σ_2	parameter controlling the local time step
τ	transformed time
τ^*	pseudotime
τ_{xx}	shear stress
τ_{xy}	shear stress
τ_{yy}	shear stress
τ_{1i}	index notation for the first tangential unit vector
τ_{2i}	index notation for the second tangential unit vector
$\tau_{1,ni}$	quantity related to rotation
$\tau_{2,ni}$	quantity related to rotation
ϕ_r	free surface rotation angle
χ	multiplication factor in grid adjustment procedure

ψ_i	index notation for three rotation transformations
ω	rotational speed
ω	explicit smoothing parameter
Φ	dissipation function

Subscripts

x	derivative or value with respect to x
y	derivative or value with respect to y
ξ	derivative or value with respect to ξ
η	derivative or value with respect to η
ref	reference value
∞	freestream value

Superscripts

p	provisional grid in the grid generation scheme
$*$	nondimensional value
$-$	lagged value in Newton linearization method
$\tilde{}$	dimensional quantity

1. INTRODUCTION

For many years engineers and scientists have been interested in predicting unsteady flow phenomena using numerical techniques. Strictly speaking, nearly all flows possess more or less unsteadiness. Steady state flows are rarely found in nature and, even with a well-controlled device in the laboratory, they are still quite difficult to achieve over a long period of time. Of course, for practical engineering purposes, the flow pattern can often be assumed to be steady in a time-averaged sense. However, for certain types of flows, steady state solutions may not exist at all, and only transient solutions can be obtained. The flow pattern inside the cylinder of an internal combustion engine, the vortex shedding flow behind a blunt body and the flow pattern related to free surface motion [1], [2], [3] to name a few, are some typical unsteady flows of practical interest. On the other hand, an understanding of the basic nature of unsteady fluid flows in various applications has always been the goal of many researchers.

In the early days, due to the limitations of computational tools and the lack of efficient numerical algorithms, one could only hope to solve a simplified set of the Navier-Stokes equations to obtain some limited but frequently useful flow information. Although numerical results from the simplified equations could also contribute to design work to some extent, wind tunnel test results played a major role in most

of the design work for both internal and external configurations at that time. This trend has gradually changed in the past two decades due to increases in computational efficiency in both the solution algorithm and computer hardware and decreasing costs for computational studies relative to experimental studies. The emergence of supercomputers in the late 1970s marked a new era in the advance of computer technology. Today the wide spread availability of high speed supercomputers with a large internal memory and multiprocessor or vector processor architectures, such as Cray series of computers, is certainly a requirement for performing a simulation of complicated three-dimensional unsteady flows. In addition, high speed workstations, which emerged on the market only in the past several years provide an alternate means for obtaining certain unsteady flow calculations at a fairly low cost.

Although truly three-dimensional unsteady viscous flow simulations are still very demanding in terms of computer resources, they can be achieved nowadays with the use of supercomputers and high speed workstations. In fact, some three-dimensional unsteady viscous flow simulations have been reported in the literature [4], [5], [6] recently, for the full space shuttle launch configuration including the solid rocket booster and external fuel tank. However, because the enormous amounts of computer time and memory needed for three-dimensional viscous calculations, a definite need still exists for improved numerical algorithms for these flows. The present research has been devoted to developing a numerical solution algorithm to efficiently solve unsteady flow problems. Both compressible and incompressible flows are considered. Three-dimensional liquid sloshing flows are an application of major interest in the present study.

In the following several sections, some pertinent literature related to the present

research is reviewed. This is followed by a section on the scope of this study. Finally, this chapter is concluded with an outline of the thesis.

1.1 Overview

1.1.1 Two-dimensional compressible flows

Over the past two decades, a number of different finite-difference schemes have been proposed to solve the Navier-Stokes equations [7]. Traditionally, they have been classified as methods for either compressible or incompressible flows. Most of the formulations for compressible flows have utilized conservative variables [8], [9], [10] which include density, instead of pressure, as a primary variable, and the equations have generally been cast in a strong conservation law form and solved in a coupled (simultaneously) manner. Among these compressible numerical formulations, the most successful methods are based on time-marching, shock-capturing algorithms. Such formulations are advantageous in that the same solution algorithm may be used for both steady and unsteady flow calculations. By using a strong conservation law form of the governing equations, flow discontinuities such as shock waves or contact discontinuities can be automatically captured as the solution develops without special treatment [11]. However, the recent work of Karki and Patankar [12] and Van Doormaal et al. [13] applied the SIMPLE type [14] segregated (one variable from one equation at a time) solution procedure and successfully solved flows with embedded shocks. This approach, however, is still in an early stage of development for flows with shocks.

Methods for incompressible flows, on the other hand, have employed a wider range of dependent variables, including derived as well as primitive, and the equations

have generally been solved in a segregated manner. For two-dimensional flow calculations, the derived variable approaches, e.g., streamfunction/vorticity formulations, require fewer unknowns to be determined than the original Navier-Stokes equations and satisfy the continuity equation automatically [15]. However, if pressure information is required, an additional equation (a Poisson equation) must be solved. This approach becomes much less attractive in three dimensions because more equations must be solved for a larger number of unknowns than would be required by solving the original Navier-Stokes equations. This approach includes the vorticity/velocity formulation [16], [17] and vorticity/vector potential formulation [18]. Six equations are required to close the system.

On the other hand, the primitive variable approaches for incompressible flows do not satisfy the continuity equation (or the so-called *compatibility condition*) automatically and some type of correction scheme must be applied to both the pressure and the velocity fields to satisfy this compatibility condition as the solution develops. The widely used schemes of the SIMPLE family [14] are in this category. Recently, a new time accurate, primitive variable approach has become more and more popular for solving incompressible flows [19], [20], [21]. This method is known as the *artificial compressibility method*, and was initially proposed by Chorin [22] for steady flow calculations. Recent versions of this method solve the algebraic system of equations in a coupled manner similar to the approaches most commonly used for the compressible Navier-Stokes equations. This method will be discussed in more detail in the next section.

Numerical methods developed for compressible flows have not been, in general, suitable for efficiently solving low Mach number or incompressible flows. The reasons

usually offered for this are : (1) roundoff error due to using density as a primary variable [23], [24], (2) truncation errors due to applying approximate factorization in multiple dimensional problems [25], and (3) a time step (or CFL number) constraint due to near infinite acoustic speed [7]. Issa [23] showed that when the density was used as a dependent variable in calculating low Mach number flows, the accuracy of evaluating the pressure gradients in the momentum equations was very sensitive to tiny variations in the density. The roundoff error due to this sensitivity to small variations in density sometimes can grow and dramatically slow down the convergence rate of the calculation. To circumvent this problem, pressure can be chosen as a primary variable instead of density because the variation of pressure is generally significant for all flow regimes. This idea has been used [26] in solving low Mach number steady flows by a coupled space marching procedure which involves using multiple sweeps to account for the upstream propagation of pressure signals. But this space marching procedure is only effective for flows with a dominant flow direction. Recently, a similar idea, although different in detail, was proposed to alleviate the above problems using a segregated algorithm [12]. Feng and Merkle [27] also employed pressure as a primary variable in a scheme that utilized a preconditioning technique to scale all eigenvalues of the coupled system of equations to the same order of magnitude in order to accelerate convergence for low Mach number steady flows.

The approximate factorization (AF) procedure is often used for compressible flow calculations in multiple dimensional problems. This procedure was first proposed by Warming and Beam [28] and has been very widely used since it splits the numerical solution procedure in the multiple dimensional problems into several one-dimensional operators which permits the solution to be obtained in the domain of

interest one direction at a time. The advantage of doing this is that in each direction, the coefficient matrix becomes block tridiagonal, and the system can be solved very efficiently with modest computer storage. However, the error due to this factorization procedure becomes worse and worse as the flow Mach number becomes smaller and smaller [25]. Instead of utilizing the AF scheme, a strongly implicit procedure (SIP) proposed by Stone [29] is used in this study to solve the algebraic equations. The modified form of the SIP algorithm (MSIP) proposed by Schneider and Zedan [30] exhibits faster convergence and less sensitivity to the relaxation-type parameter of the method than the original SIP algorithm. The MSIP algorithm was extended to handle a coupled 4×4 block system in the present work. The SIP method will be discussed in more detail in another section in this chapter and in Chapter 4.

There are many applications in which it would be convenient to use the same algorithm for Mach numbers ranging from incompressible to transonic. The search for an algorithm suitable for all speeds goes back at least to the work of Harlow and Amsden [31]. More recent work on the subject includes contributions from Karki and Patankar [12] and Van Doormaal et al. [13]. The main contribution of the present research on two-dimensional flows is to point out a solution strategy that could be applied to a number of difference formulations to permit efficient computation over a wider range of Mach numbers. The specific difference stencil used in the present work may not be optimum for all cases, and can clearly be improved. The form used, however, does serve to illustrate the advantages of the overall approach.

1.1.2 Three-dimensional incompressible liquid sloshing flows

The liquid sloshing motion inside a container has long been of interest to engineers and researchers. Liquid sloshing occurs in many important practical applications such as in oil tankers, railroad tank cars, missiles, satellites and spacecraft [32], [33], [34]. The major concern about the liquid sloshing motion within a container is that a substantial periodic force may be generated by this motion which may affect the stability of the moving vehicle. If the sloshing frequency is near the natural frequency of the vehicle structure, resonance may increase the likelihood of structural damage or an instability resulting from the motion.

The sloshing motion is usually induced by the motion of the container, which causes changes in the original equilibrium pressure field within the fluid. This type of motion usually involves the presence of a free surface which is the interface between the liquid and air or other type of gas. The presence of the free surface adds another difficulty in analysis to an already complicated fluid motion, since the free surface position usually is not known *a priori* and has to be determined as part of the solution. The container may undergo several different kinds of motion ranging from a simple linear acceleration or rotation to more complicated combinations of these. To conveniently analyze the motion, it is usually necessary to transform the governing equations to a noninertial coordinate system [35].

The sloshing motion of liquid is governed by the incompressible Navier-Stokes equations. The motion of the liquid is generally three-dimensional, time-dependent and sufficiently complex that no major simplification to the general equations is possible. The accurate simulation of such motion is a formidable problem primarily because of the computational resources required, and few, if any, three-dimensional

time-dependent simulations have been reported in the literature.

Generally, incompressible flows have been solved successfully using both primitive variables (velocity components and pressure) or derived variables such as stream-function and vorticity as mentioned earlier. Although the methods based on derived variables work well in two dimensions, in three dimensions, they require the solution of more equations than the methods based on primitive variables. As a result, the methods based on derived variables have not been widely used by others for solving complex three-dimensional flows, and were not selected for use in the present study.

The most frequently used approaches for solving the time-dependent, incompressible Navier-Stokes equations in primitive variables fall into two broad categories. The first is generally known as the method of fractional steps [36], [37]. In this approach, the solution is advanced one time increment in two or more steps. In the first step, the momentum equations are solved for an approximate velocity field that is generally not divergence free (may not conserve mass). In the second step, the pressure field which corresponds to a divergence-free velocity field is computed and the velocity is corrected to conserve mass. This step generally leads to a Poisson equation for pressure. The SIMPLE type schemes mentioned in the previous section belong to this category.

The second approach is known as the artificial (or pseudo) compressibility method. In this method a fictitious time derivative of pressure is added to the continuity equation so that the solution of the set of conservation equations can be marched in time. Originally, this method was thought to be only applicable to steady flow problems. For these, the entire time dependence was fictitious but the solution approached the correct steady state solution asymptotically with time. More recently, investigators

[19], [20], [21] have suggested that the procedure can be made accurate with respect to time by considering the time-like variable appearing in the fictitious time term added to the continuity equation to be a pseudotime. For each physical time step, the pseudotime is advanced several increments in an iterative fashion. When the variables no longer change with pseudotime, the fictitious time term is zero and the solution satisfies the correct form of the continuity equation for incompressible flows at the specified physical time. It is clearly desirable to keep the number of subiterations to a minimum in this dual time-stepping procedure.

Methods for dealing with the free surface in the simulations also fall into two categories: free surface "fitting" (or "tracking") and free surface "capturing". In surface fitting, the calculations are carried out in a transformed coordinate system that conforms to the shape of the free surface [1], [2], [38]. Appropriate boundary conditions are applied at the free surface, and the surface location changes with time as dictated by the velocities computed at grid points falling on the free surface. Generally, the grid points are moved after each time step as a new surface conforming grid is constructed. The new grid "adapts" to the changed geometry of the computational domain.

With surface capturing, the free surface is located or "captured" by a computation over a larger domain that includes a fluid of much smaller density and viscosity fictitiously placed over the free surface. In the liquid sloshing problem, the second fluid would have very little influence on the motion of the denser liquid. The governing equations are solved throughout both fluids. Steep gradients in fluid density indicate the location of the free surface. Several variations in the surface capturing procedure have been reported in the literature [39]. Generally, a fixed grid is used

with this method although the grid could be altered between time steps to provide a finer grid in the neighborhood of the evolving interface. An excellent review paper by Floryan and Rasmussen [40] provides more than 100 references about both surface "fitting" and "capturing" methods. Interested readers may refer to this review article.

The present study utilizes the surface "fitting" approach for the free surface and the artificial compressibility method to provide the essential pressure-velocity coupling without the need for deriving a complex pressure Poisson equation. In the present analysis, a partially filled spherical container is assumed to be undergoing a general motion characteristic of that experienced by a spin-stabilized satellite. Therefore, a general formulation of the governing equations is essential to efficiently describe the liquid motion. Chakravarthy [41] investigated laminar incompressible flow motion within liquid filled shells under rotation but without the presence of free surfaces. Vaughn, Oberkampf and Wolfe [35] solved the three-dimensional incompressible Navier-Stokes equations for a fluid-filled cylindrical canister that was both spinning and nutating. The equations were transformed to a noninertial frame to easily describe the the flow motion under this spinning and nutating condition. Again the container was completely filled with fluid and no free surface was present. It was observed from a literature review that liquid sloshing problems have generally been restricted to either cylindrical [42] or rectangular [39] geometries.

Some preliminary work on sloshing in spherical containers was reported by Kassinos and Prusa [38], in which the general motion of the spherical container was accounted for by a complete coordinate transformation using several successive axis rotations and a translation. The mathematical formulation of Kassinos and Prusa,

which is applicable to sloshing phenomena under a variety of conditions, was adopted in this study. However, a completely different numerical approach was used to solve the governing equations in the present study. In the approaches used by Kassinos and Prusa [38] (a type of fractional step method), the compatibility condition for an incompressible fluid was satisfied indirectly by solving a Poisson equation derived from the continuity and momentum equations to obtain the pressure. The algebraic form of the governing equations was then solved by a Gauss-Seidel method in a segregated manner, i.e., one equation solved for each variable.

Since the long-term goal of the research project of which present study is a part is to numerically simulate the interaction between the liquid sloshing motion of the container and the satellite structure, several important features of the present formulation were designed to handle the future interaction. Due to the elasticity of the structure to which the container is attached, the motion of the container will be affected by the structure deformation, and likewise, the structure will be affected by the liquid sloshing motion within the container. In order to simulate the liquid motion aboard a satellite, it is not realistic to simply simulate the liquid motion alone using a prescribed motion of the container. The simulation should be accomplished by considering the interaction between the motion of the liquid and the dynamics of the structure itself (determined from a numerical solution of the equations governing the dynamics of the structure) at each time step. The motion of the container cannot be precisely determined in advance in this interaction procedure. The current formulation was designed in such a way that it is ready to accept the instantaneous container position, angular velocity, and acceleration as input to construct the related quantities in the code. Based on this information, the present CFD code will compute

the flow solution, including the new position of the free surface, and pass the location of the center of gravity of the fluid and the container, and the resulting sloshing force and moment at the current time back to the structural code. The interaction will continue indefinitely or until a final steady state solution is reached. To date such an interaction has not been simulated, although the current formulation has been designed in accordance with this future goal.

With the adoption of the artificial compressibility method for solving the three-dimensional incompressible equations, the numerical solution algorithm for both the two and three-dimensional equations is identical except that the coupled two and three-dimensional SIP solvers are slightly different in form. The SIP method will be briefly described in the following section and further details will be provided in Chapter 4 and Appendix F.

1.1.3 Methods for solving the algebraic equations

Methods for solving the algebraic system of equations arising from differencing of partial differential equations usually fall into two main strategies [7]: one is the direct solution method and the other is the iterative solution method. In general, a direct solution method involves a form of Gaussian elimination and requires an amount of storage (especially for the three-dimensional algebraic system of equations occurring in the present study) which is beyond the memory capacity of most current computers. On the other hand, since the Navier-Stokes equations are a set of highly coupled nonlinear equations, even when a direct solution method is used, some type of "iterative" procedure may be needed to remove (or at least minimize) the errors due to the linearization procedure. For these reasons, the direct solution method

was not used to solve the matrix system in this study; instead, an iterative solution method was adopted.

Several different iterative methods are currently being used in CFD applications [7]. A point Gauss-Seidel method is the simplest iterative method. It is extremely easy to program but converges relatively slowly, and for some difficult problems the scheme may diverge readily due to a very low degree of solution coupling. A variation of the point Gauss-Seidel method is called the successive over-relaxation (SOR) method. In this method an over-relaxation parameter is introduced to accelerate the convergence rate. The above two methods are considered as "explicit" iterative schemes since the unknowns at the neighboring points are treated explicitly. Another type of iterative method is known as a semi-implicit iterative (or block iterative) procedure. The most widely used methods belonging to this category are SOR by lines (SLOR) and the alternating direction implicit (ADI) method. The reason they are called "semi-implicit" is that in multi-dimensional problems, these methods treat the unknowns implicitly only in one direction at a time and lag the unknowns in the other direction(s) to the right hand side (RHS) of the matrix system of equations. These methods usually lead to a tridiagonal matrix system for a scalar equation or a block tridiagonal matrix for vector equations. They are presently very popular because less computer memory is required to store the coefficient matrix and efficient tridiagonal matrix solvers are readily available (see [7]). In multi-dimensional flow problems, the lagging of the unknowns to the RHS can sometimes result in very slow convergence or even solution divergence for some difficult problems. In spite of the above problems, the semi-implicit iterative methods are still widely used in the CFD community due to their relative simplicity and modest memory requirement.

Another type of iterative method is known as the strongly implicit method [43]. It has a faster convergence rate than the methods mentioned previously such as SOR, SLOR and ADI. One version of the strongly implicit method which is beginning to gain favor for solving fluid flow problems is the strongly implicit procedure (SIP) proposed by Stone [29]. It is called "strongly implicit" because the method treats all unknowns in a 2-D plane for two-dimensional problems and a 3-D cube for three-dimensional problems in a strongly implicit manner. No unknowns at the neighboring points are lagged to the RHS of the matrix system. Due to this strongly implicit treatment for the governing equations, the coupling between the unknowns at each grid point is greatly enhanced.

For two-dimensional flows, Schneider and Zedan [30] proposed a modified strongly implicit procedure (MSIP) which extended Stone's 5-point SIP formula to a 9-point formula. They showed that MSIP was better than SIP in that it was less parameter dependent, less sensitive to the grid aspect ratio, and exhibited a faster convergence rate. The MSIP scheme reduces to Stone's 5-point SIP if the coefficients at the four corner points of the difference molecule are set to zero. Zedan and Schneider [44] also extended Stone's 5-point formula to a vector (or coupled) equation. This extension is very straightforward. For three-dimensional equations, Weinstein, Stone and Kwan [45] derived a 7-point SIP formula for both scalar and coupled equations. Zedan and Schneider [46], following the same MSIP idea for two-dimensional equations again, extended the 7-point formula to a 19-point formula for a scalar three-dimensional equation.

Despite the fact that Stone's SIP method was first introduced about two decades ago, it has only recently been widely used in the CFD community, mainly because

it requires somewhat more computer memory than other iterative schemes and this additional memory has only become readily available in recent years. Several applications using the SIP method to solve fluid flow problems can also be found in Walters, Dwoyer and Hassan [47], Reddy and Rubin [48] and Khosla and Rubin [49] and Ramakrishnan and Rubin [50]. In the present study, the 9-point MSIP method and the 7-point SIP method will be used to solve, respectively, the coupled two-dimensional compressible Navier-Stokes equations and the coupled three-dimensional incompressible Navier-Stokes equations.

1.2 Scope of the Present Study

It has been the goal of the present research to develop a numerical algorithm to efficiently compute two and three-dimensional unsteady viscous flows. Special effort was devoted to implementing the present numerical procedure in a manner to permit the calculation of compressible flows at all speeds, i.e., over a wide range of Mach numbers, and to predicting three-dimensional incompressible liquid sloshing flows. A unified approach to solve both the two-dimensional compressible equations and the three-dimensional incompressible equations was achieved by choosing the primitive variables, (u, v, p, T) for two-dimensional compressible flows and (u, v, w, p) for three-dimensional incompressible flows, as the dependent variables in the governing equations and solving the resulting algebraic system of equations by a coupled strongly implicit procedure. One of the main goals of the present research was to see if the use of pressure as a dependent variable would permit the computation of low Mach number nearly incompressible flows with the compressible formulation of the governing equations while still providing a shock capturing capability for shock-

embedded flows.

The CSIP method has not been widely used for coupled Navier-Stokes calculations. The test of the performance of this method for a wide variety of flow problems, including an unsteady two-dimensional vortex shedding flow over a circular cylinder and several truly unsteady three-dimensional liquid sloshing flows under complicated boundary conditions, was another objective of this research. Also by using the CSIP method instead of more traditional line solvers, it was hoped to enhance the robustness of the solution procedure although more computer storage would be required with this method.

Free surface motion has long been a topic of interest for theoretical, experimental and numerical fluid analysts. To accurately predict this type of complex flow numerically was also one of the main goals in this study. Considerable effort was devoted to adapting the present algorithm to deal with this formidable problem. Several test cases for both compressible and incompressible flows have been solved in this study. They include:

1. Two-dimensional compressible flows
    (a) Developing flow in a channel inlet
    (b) Driven cavity
    (c) Steady flow over a circular cylinder
    (d) Unsteady vortex shedding flow over a circular cylinder
    (e) Supersonic shock-boundary layer interaction
2. Three-dimensional incompressible flows

(a) Steady and unsteady driven cavity flow

(b) Liquid flows with free surfaces

i. Initially capped axisymmetric spin-up with glycerin

ii. Initially capped axisymmetric spin-up with kerosene

iii. Gradual axisymmetric spin-up with glycerin

iv. Impulsive axisymmetric spin-up with glycerin

v. Initially capped asymmetric spin-up with glycerin (two cases)

All of these cases not only provide a means to evaluate the present numerical algorithm, but also provide a challenging opportunity for the present code to handle complicated three-dimensional liquid flow problems.

1.3 Outline of the Thesis

The motivation and objectives of the present research and some pertinent literature have been reviewed in this chapter. In the next several chapters, the computation methodology for solving fluid flows with the present solution procedure will be described. Chapter 2 details the mathematical formulation of the governing equations in generalized nonorthogonal coordinates for both two-dimensional compressible and three-dimensional incompressible flows. Several successive coordinate rotations for the three-dimensional incompressible equations are required to obtain equations suitable to describe the fluid motion under a complicated rotation and nutation. Boundary conditions for various types of flow problems encountered in this study are derived for two and three-dimensional geometries in Chapter 3. Chapter 4 deals with

details of the present numerical algorithm and includes discussion of the discretization method, the linearization method, the artificial compressibility method, and the coupled strongly implicit procedure. Results for steady and unsteady compressible flows and unsteady liquid sloshing flows are presented in Chapter 5. Discussion of these results is also contained in Chapter 5. Concluding remarks and recommendations about the present research are given in Chapter 6. Chapters 8 to 13 are the appendix sections which provide some detailed derivations to supplement the main body of the present thesis.

2. MATHEMATICAL FORMULATION OF THE GOVERNING EQUATIONS

In this chapter the mathematical equations which model fluid flow are presented. These equations are the Navier-Stokes equations. They state the conservation of mass, momentum and energy. The usual form of these equations for a Newtonian fluid with the Stokes hypothesis [7] can be expressed as follows:

$$\frac{D\rho}{Dt} + \rho \nabla \cdot \vec{V} = 0 \tag{2.1}$$

$$\rho \frac{D\vec{V}}{Dt} = \vec{g} - \nabla p + \frac{\partial}{\partial x_j}[\mu(\frac{\partial u_i}{\partial x_j} + \frac{\partial u_j}{\partial x_i}) - \frac{2}{3}\delta_{ij}\frac{\partial u_k}{\partial x_k}] \tag{2.2}$$

$$\rho \frac{De}{Dt} + p \nabla \cdot \vec{V} = \frac{\partial Q}{\partial t} - \nabla \cdot \vec{q} + \Phi \tag{2.3}$$

where ρ is the density, $\vec{V}$ is the velocity vector, p is the hydrostatic pressure, e is the internal energy per unit mass, $\vec{g}$ is the body force, δ_{ij} is the Kronecker delta function:

$$\delta_{ij} = \begin{cases} 1 & \text{if } i = j \\ 0 & \text{if } i \neq j \end{cases}$$

$\frac{\partial Q}{\partial t}$ represents heat energy production by external agencies, $\vec{q}$ is the heat conduction and Φ is dissipation. Fourier's law of heat conduction will be assumed to apply so

$$\vec{q} = -k \nabla T$$

The dissipation function for a Newtonian fluid in a Cartesian coordinate system becomes

$$\Phi = \mu[2(u_x^2+v_y^2+w_z^2)+(v_x+u_y)^2+(w_y+v_z)^2+(u_z+w_x)^2-\frac{2}{3}(u_x+v_y+w_z)^2] \quad (2.4)$$

The ideal gas equation of state and a viscosity law are used to close the system for laminar flow. Equations (2.1)-(2.3) are the general form of the governing equations written in Cartesian coordinates.

In the sections that follow, the appropriate form of the governing equations for two-dimensional compressible and three-dimensional incompressible flows will be derived.

2.1 Governing Equations For Two-Dimensional Compressible Flows

2.1.1 Physical coordinates

The two-dimensional Navier-Stokes equations are obtained from Eqs. (2.1)-(2.3) by dropping terms in the third dimension. They are recast in a strong conservation-law form as follows:

$$\frac{\partial Q}{\partial t}+\frac{\partial E}{\partial x}+\frac{\partial F}{\partial y}=0 \quad (2.5)$$

where

$$Q=\begin{pmatrix} \rho \\ \rho u \\ \rho v \\ E_t \end{pmatrix}$$

$$E = \begin{pmatrix} \rho u \\ \rho u^2 + p - \tau_{xx} \\ \rho uv - \tau_{xy} \\ E_t u + pu - u\tau_{xx} - v\tau_{xy} + q_x \end{pmatrix} \quad F = \begin{pmatrix} \rho v \\ \rho vu + p - \tau_{xy} \\ \rho v^2 - \tau_{yy} \\ E_t v + pv - u\tau_{xy} - v\tau_{yy} + q_y \end{pmatrix}$$

where q_x and q_y are the x and y components of the heat conduction vector $\vec{q}$ respectively, E_t is the total energy per unit volume which is defined as:

$$E_t = \rho e + \frac{1}{2}\rho(u^2 + v^2)$$

and the τ_{xx}, τ_{yy} and τ_{xy} are the shear stresses which are defined as follows:

$$\tau_{xx} = \frac{2}{3}\mu(2\frac{\partial u}{\partial x} - \frac{\partial v}{\partial y})$$

$$\tau_{yy} = \frac{2}{3}\mu(2\frac{\partial v}{\partial y} - \frac{\partial u}{\partial x})$$

$$\tau_{xy} = \mu(\frac{\partial u}{\partial y} + \frac{\partial v}{\partial x})$$

where μ for air is determined by the Sutherland formula [7] as follows:

$$\mu = \frac{C_1 T^{3/2}}{(T + C_2)} \tag{2.6}$$

The Sutherland constants C_1 and C_2 are:

$$C_1 = 1.458 \times 10^{-6} \ \ Kg/(m\ s\ \sqrt{K}), \quad C_2 = 110.4 \ \ K$$

The body force term $\vec{g}$ has been neglected in Eq. (2.5) since body forces were not considered in the two-dimensional applications in this study. The dependent

variables in Eq. (2.5), ρ, ρu, ρv and E_t, are the so-called conserved variables. Traditionally, the conserved variables have been used as the dependent variables in the compressible flow calculations [9]. However, as mentioned in the previous chapter, using density as a primary variable contributes to convergence problems in low Mach number flow calculations. To circumvent this problem, pressure is chosen as a primary variable instead of density in this study, because the variation of pressure is generally significant for all flow regimes. In this study, the ideal gas law is used to relate the density, pressure and temperature as follows:

$$\rho = \frac{p}{RT} \tag{2.7}$$

where R is the gas constant. For air, R is equal to 287 $m^2/(s^2\ K)$

After replacing the density by pressure and temperature in Eq. (2.5) using Eq. (2.7), the governing equations become

$$\frac{\partial Q(q)}{\partial t} + \frac{\partial E(q)}{\partial x} + \frac{\partial F(q)}{\partial y} = 0 \tag{2.8}$$

where

$$q = \begin{pmatrix} u \\ v \\ p \\ T \end{pmatrix} \qquad Q = \begin{pmatrix} \frac{pu}{T} \\ \frac{pv}{T} \\ \frac{p}{T} \\ (C_p - R)p + \frac{1}{2}\frac{pu^2}{T} + \frac{1}{2}\frac{pv^2}{T} \end{pmatrix}$$

$$E = \begin{pmatrix} \frac{p}{T}uu + Rp - R\tau_{xx} \\ \frac{p}{T}uv - R\tau_{xy} \\ \frac{p}{T}u \\ (C_p p + \frac{p}{T}\frac{u^2}{2} + \frac{p}{T}\frac{v^2}{2})u - Ru\tau_{xx} - Rv\tau_{xy} - RkT_x \end{pmatrix}$$

$$F = \begin{pmatrix} \frac{p}{T}uv - R\tau_{xy} \\ \frac{p}{T}vv + Rp - R\tau_{yy} \\ \frac{p}{T}v \\ (C_{pp} + \frac{p}{T}\frac{u^2}{2} + \frac{p}{T}\frac{v^2}{2})v - Ru\tau_{xy} - Rv\tau_{yy} - RkT_y \end{pmatrix}$$

In Eq. (2.8) the Q, E and F vectors are functions of the primitive variable vector q. The choice of pressure as a primary dependent variable in the governing equations results in a Eq. (2.8) being somewhat more complicated in form than Eq. (2.5). However, it should be noted that the viscous terms in the momentum equations and the viscous dissipation and conduction terms in the energy equation are expressed in terms of the primitive variables and become more straightforward to deal with in the linearization process. This will be discussed again in Chapter 4.

2.1.2 Nondimensional form

It is a common practice to use nondimensionalized equations as the basis for numerical approximations. The advantage to this strategy is that it eliminates the need for many dimensional conversion factors within the program, and if the proper reference values are prescribed, it ensures that all variables have numerical values within a specific range (i.e., 0.0-1.0).

For convenience, the following nondimensional variables are defined (nondimen-

sional quantities are indicated by a asterisk):

$$t^* = \frac{t}{L_{ref}/u_{ref}} \quad x^* = \frac{x}{L_{ref}} \quad y^* = \frac{y}{L_{ref}} \quad u^* = \frac{u}{u_{ref}} \quad v^* = \frac{v}{u_{ref}}$$

$$\rho^* = \frac{\rho}{\rho_{ref}} \qquad p^* = \frac{p}{(\rho_{ref} u_{ref}^2)} \qquad T^* = \frac{T}{T_{ref}} \qquad \mu^* = \frac{\mu}{\mu_{ref}}$$

$$R^* = \frac{R}{(u_{ref}^2/T_{ref})} = \frac{1}{\gamma M_\infty^2} \qquad C_p^* = \frac{C_p}{(u_{ref}^2/T_{ref})} = \frac{1}{(\gamma - 1)M_\infty^2}$$

The nondimensional parameters Re, M_∞ and Pr represent Reynolds number, Mach number and Prandtl number, respectively, and are defined as follows:

$$Re = \frac{\rho_{ref} u_{ref} L_{ref}}{\mu_{ref}}, \quad M_\infty = \frac{u_{ref}}{\sqrt{\gamma R T_{ref}}}, \quad Pr = \frac{C_p \mu}{k}$$

The new nondimensional Sutherland constants C_1^* and C_2^* are defined as follows:

$$C_1^* = C_1 \frac{T_{ref}^{1/2}}{\mu_{ref}} \qquad C_2^* = \frac{C_2}{T_{ref}}$$

and the nondimensional Sutherland formula for air becomes

$$\mu^* = \frac{C_1^* T^{*3/2}}{(T^* + C_2^*)} \tag{2.9}$$

The local thermal conductivity k can be determined from the Prandtl number which is assumed to be constant in the present study:

$$k = \frac{C_p \mu}{Pr}$$

The definition of each of these variables can be found in the Nomenclature.

For all the compressible flow cases examined in this study, the working fluid was considered to be air, and unless otherwise noted, the following constant values of fluid properties were used:

$$C_p = 1005 \ \ m^2/(s^2\ K) \qquad \gamma = 1.4$$

$$\mu_{ref} = 1.6 \times 10^{-5} \ \ kg/(m\ s) \qquad P_r = 0.7$$

The above nondimensional quantities are substituted into Eq. (2.8) and the resulting equation in nondimensional form is:

$$\frac{\partial Q(q)}{\partial t} + \frac{\partial E(q)}{\partial x} + \frac{\partial F(q)}{\partial y} = 0 \tag{2.10}$$

where

$$q = \begin{pmatrix} u \\ v \\ p \\ T \end{pmatrix} \qquad Q = \begin{pmatrix} \frac{pu}{T} \\ \frac{pv}{T} \\ \frac{p}{T} \\ (C_p - R)p + \frac{1}{2}\frac{pu^2}{T} + \frac{1}{2}\frac{pv^2}{T} \end{pmatrix}$$

$$E = \begin{pmatrix} \frac{p}{T}uu + Rp - \tau_{xx} \\ \frac{p}{T}uv - \tau_{xy} \\ \frac{p}{T}u \\ (C_p p + \frac{p}{T}\frac{u^2}{2} + \frac{p}{T}\frac{v^2}{2})u - u\tau_{xx} - v\tau_{xy} - \frac{RC_p\mu}{P_r Re}T_x \end{pmatrix}$$

$$F = \begin{pmatrix} \frac{p}{T}uv - \tau_{xy} \\ \frac{p}{T}vv + Rp - \tau_{yy} \\ \frac{p}{T}v \\ (C_{pp} + \frac{p}{T}\frac{u^2}{2} + \frac{p}{T}\frac{v^2}{2})v - u\tau_{xy} - v\tau_{yy} - \frac{RC_{p\mu}}{P_r Re}T_y \end{pmatrix}$$

and

$$\tau_{xx} = \frac{2}{3}\frac{R\mu}{Re}(2\frac{\partial u}{\partial x} - \frac{\partial v}{\partial y})$$

$$\tau_{yy} = \frac{2}{3}\frac{R\mu}{Re}(2\frac{\partial v}{\partial y} - \frac{\partial u}{\partial x})$$

$$\tau_{xy} = \frac{R\mu}{Re}(\frac{\partial u}{\partial y} + \frac{\partial v}{\partial x})$$

In Eq. (2.10), the superscript $*$'s for all nondimensional variables have been dropped for convenience.

2.1.3 Transformed coordinates

In order to solve Eq. (2.10) numerically it is generally necessary to use a variably spaced numerical grid. The equations can be differenced in their present form for variable grid spacing, but the resulting system is complicated and difficult to program. Instead, a coordinate transformation is applied to the governing equations, and the equations can be solved in a uniformly-spaced computational plane while taking advantage of variable spacing in the physical domain.

When the grid was stationary in the physical domain, the following generalized coordinate transformation was used:

$$\tau = t \qquad \xi = \xi(x, y) \qquad \eta = \eta(x, y)$$

The metrics of the transformation are:

$$\xi_x = Jy_\eta \quad \xi_y = -Jx_\eta \quad \eta_x = -Jy_\xi \quad \eta_y = Jx_\xi \tag{2.11}$$

and the Jacobian is given by

$$J = \frac{\partial(\xi,\eta)}{\partial(x,y)} = \xi_x\eta_y - \eta_x\xi_y = \frac{1}{x_\xi y_\eta - x_\eta y_\xi} \tag{2.12}$$

Applying the above coordinate transformation to Eq. (2.10) through the application of the chain rule:

$$\frac{\partial}{\partial x} = \xi_x\frac{\partial}{\partial \xi} + \eta_x\frac{\partial}{\partial \eta}$$

the governing equation becomes

$$\frac{\partial Q}{\partial \tau} + \xi_x\frac{\partial E}{\partial \xi} + \eta_x\frac{\partial E}{\partial \eta} + \xi_y\frac{\partial F}{\partial \xi} + \eta_y\frac{\partial F}{\partial \eta} = 0 \tag{2.13}$$

The application of the coordinate transformation described above has resulted in a loss of the desired strong conservation law form of the equations. The strong conservation law form of the equations is essential for proper shock-capturing in the numerical solution [11]. Fortunately, it is possible to recombine the transformed equations to recover the strong conservation law property. Following the procedure outlined by Vinokur [51], the strong conservation law form may be recovered by first dividing the equations by the Jacobian, J, and adding and subtracting like terms which may later be combined to form the conservative derivative terms. Finally the resulting equation becomes:

$$\frac{\partial \hat{Q}(q)}{\partial \tau} + \frac{\partial \hat{E}(q)}{\partial \xi} + \frac{\partial \hat{F}(q)}{\partial \eta} = 0 \tag{2.14}$$

where

$$q = \begin{pmatrix} u \\ v \\ p \\ T \end{pmatrix} \qquad \hat{Q} = \frac{1}{J} \begin{pmatrix} \frac{pu}{T} \\ \frac{pv}{T} \\ \frac{p}{T} \\ (C_p - R)p + \frac{1}{2}\frac{pu^2}{T} + \frac{1}{2}\frac{pv^2}{T} \end{pmatrix}$$

$$\hat{E} = \frac{1}{J} \begin{pmatrix} \frac{p}{T}uU + Rp\xi_x - (\xi_x\tau_{xx} + \xi_y\tau_{xy}) \\ \frac{p}{T}vU + Rp\xi_y - (\xi_x\tau_{xy} + \xi_y\tau_{yy}) \\ \frac{p}{T}U \\ (C_pp + \frac{p}{T}\frac{u^2}{2} + \frac{p}{T}\frac{v^2}{2})U \\ -\xi_x u\tau_{xx} - (\xi_x v + \xi_y u)\tau_{xy} - \xi_y v\tau_{yy} \\ -\frac{RC_p\mu}{P_r Re}[(\xi_x^2 + \xi_y^2)T_\xi + (\xi_x\eta_x + \xi_y\eta_y)T_\eta] \end{pmatrix}$$

$$\hat{F} = \frac{1}{J} \begin{pmatrix} \frac{p}{T}uV + Rp\eta_x - (\eta_x\tau_{xx} + \eta_y\tau_{xy}) \\ \frac{p}{T}vV + Rp\eta_y - (\eta_x\tau_{xy} + \eta_y\tau_{yy}) \\ \frac{p}{T}V \\ (C_pp + \frac{p}{T}\frac{u^2}{2} + \frac{p}{T}\frac{v^2}{2})V \\ -\eta_x u\tau_{xx} - (\eta_x v + \eta_y u)\tau_{xy} - \eta_y v\tau_{yy} \\ -\frac{RC_p\mu}{P_r Re}[(\xi_x\eta_x + \xi_y\eta_y)T_\xi + (\eta_x^2 + \eta_y^2)T_\eta] \end{pmatrix}$$

and

$$\tau_{xx} = \frac{2}{3}\frac{R\mu}{Re}[2(\xi_x u_\xi + \eta_x u_\eta) - (\xi_y v_\xi + \eta_y v_\eta)]$$

$$\tau_{yy} = \frac{2}{3}\frac{R\mu}{Re}[2(\xi_y v_\xi + \eta_y v_\eta) - (\xi_x u_\xi + \eta_x u_\eta)]$$

$$\tau_{xy} = \frac{R\mu}{Re}[(\xi_y u_\xi + \eta_y u_\eta) - (\xi_x v_\xi + \eta_x v_\eta)]$$

$$U = \xi_x u + \xi_y v \quad V = \eta_x u + \eta_y v$$

Equation (2.14) is the final form of the governing equations which was used in this study to solve both steady and unsteady two-dimensional flows with different geometries. Boundary conditions are needed to close the system of equations and will be discussed in Chapter 3.

In the next section, the three-dimensional Navier-Stokes equations for incompressible flows in a primitive form will be derived.

2.2 Governing Equations For Three-Dimensional Incompressible Flows

For a truly incompressible fluid, the density in Eqs. (2.1)-(2.3) is constant. If flow properties, μ and k, remain constant, Eqs. (2.1)-(2.3) can be reduced to:

$$\frac{\partial u_i}{\partial x_i} = 0 \tag{2.15}$$

$$\frac{\partial u_i}{\partial t} + u_j\frac{\partial u_i}{\partial x_j} = -\frac{1}{\rho}\frac{\partial p}{\partial x_i} + \nu\frac{\partial^2 u_i}{\partial x_j \partial x_j} - g_i \tag{2.16}$$

Equation (2.15) is the continuity equation and Eq. (2.16) is the momentum equation. Following the convention of index notation, a single (unrepeated) index is a free index and its value ranges from 1 to 3. When a repeated index appears in the same term, it represents a summation over three terms with the index ranging from 1 to 3. For incompressible flows, the energy equation is usually decoupled from the continuity and momentum equations except for flows with high temperature gradients. Since

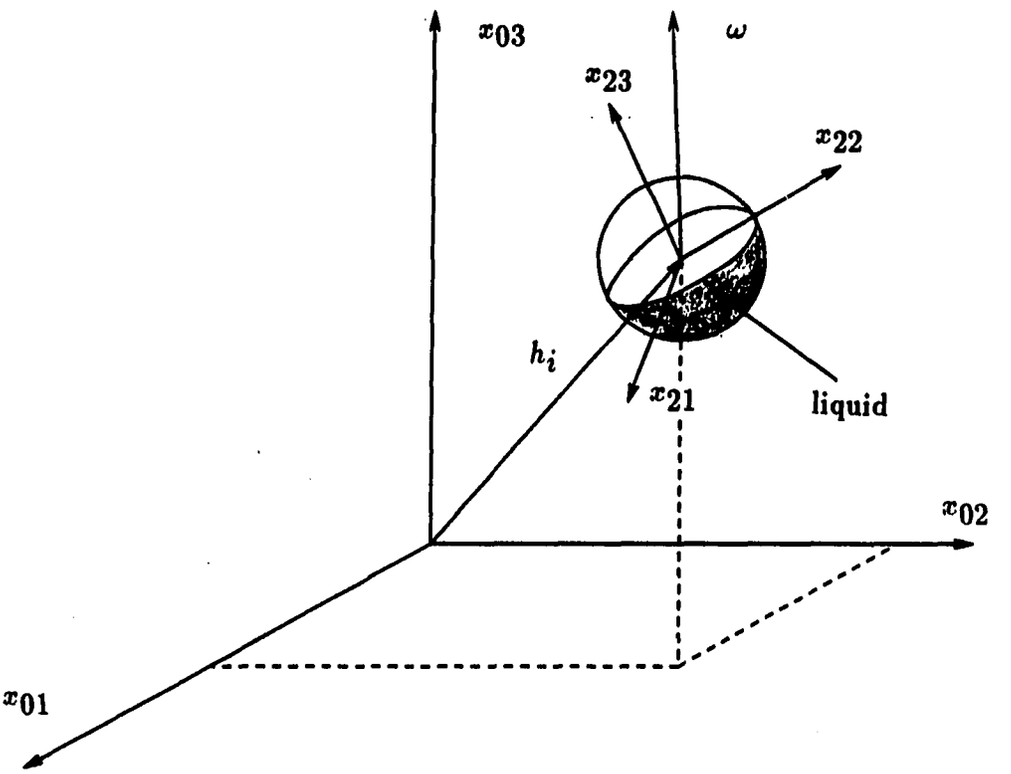

Figure 2.1: Schematic of a partially filled rotating-nutating container moving relative to an inertial frame

heat transfer is not of major interest for the incompressible flow calculations in this study, the energy equation was not solved in the three-dimensional cases. However, it can be added to the above equations if the temperature distribution is needed.

Both equations are written in index notation. The choice of the index notation for the three-dimensional incompressible equations is based on the fact that for the three-dimensional liquid sloshing motion inside a spherical container considered in this study, use of this notation facilitates the derivation of new equations accounting for the general rotating-nutating motion of the container. A schematic diagram of

the partially filled rotating-nutating container is shown in Fig. 2.1.

Since this problem involves a general rotating-nutating motion of the container, there are at least two different approaches to solving this problem. First, the above equations could be solved in the form indicated above together with the proper treatment of the boundary conditions in accordance with the rotating-nutating motion of the container at any instant of time. Ideally, this treatment is workable for a simple motion of the container, but will become impractical and difficult for describing the motion and interpreting the results if a general rotating-nutating motion is encountered. Actually, such a general motion can arise in the interaction between a satellite structure and the liquid sloshing in a partially filled container. Therefore it is more appropriate to handle the general motion of the container with terms within the equations themselves. That is, the motion of the container relative to an inertial frame can be implicitly accounted for by proper coordinate transformations. This is the second approach and the one that will be adopted in this study.

Following the approach outlined in [38], several steps are needed to transform the governing equations from an inertial frame to a noninertial frame. They are described in the following several sections. In addition to those transformations, a generalized nonorthogonal coordinate transformation was applied to the resulting equations to handle the irregular geometry of the boundaries. The transformations needed are summarized as follows and will be discussed one by one.

1. inertial frame $\rightarrow x_0$ coordinate

2. ψ_1, ψ_2 and ψ_3 rotation $\rightarrow x_1$ coordinate

3. translation $h_i \rightarrow x_2$ coordinate

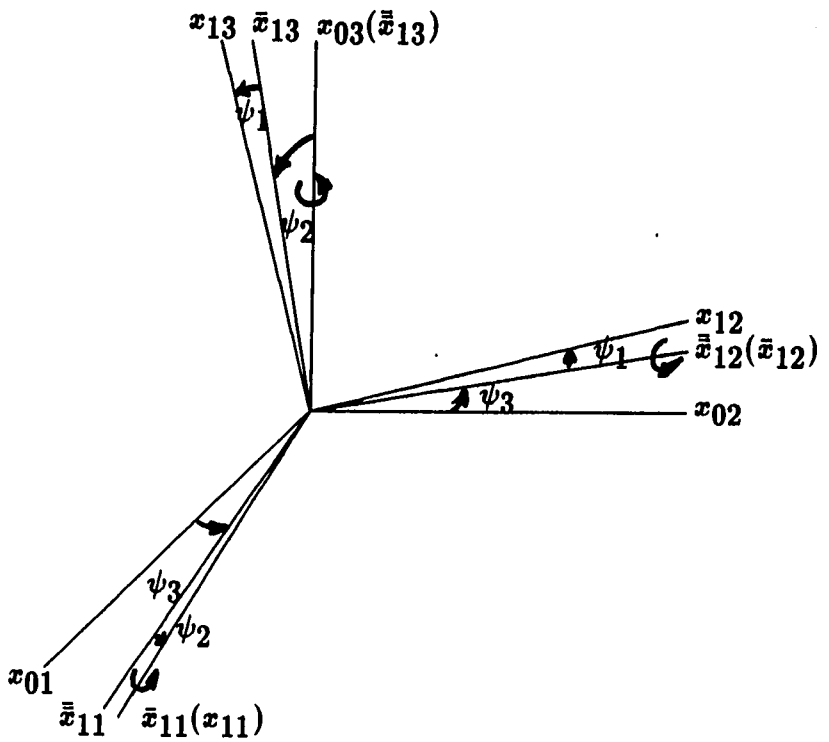

Figure 2.2: Notation for the three successive coordinate rotations

4. free surface tracking transformation, ϕ_r rotation $\rightarrow x_3$ coordinate

5. generalized nonorthogonal coordinate transformation $\rightarrow z$ coordinate

2.2.1 The rotating-nutating coordinates: x_1 coordinate system

The original three-dimensional incompressible equations will be labeled with a subscript 0 to indicate that they are in x_0 inertial frame and rewritten as

$$\frac{\partial u_{0i}}{\partial x_{0i}} = 0 \tag{2.17}$$

$$\frac{\partial u_{0i}}{\partial t_0} + u_{0j}\frac{\partial u_{0i}}{\partial x_{0j}} = -\frac{1}{\rho}\frac{\partial p}{\partial x_{0i}} + \nu\frac{\partial^2 u_{0i}}{\partial x_{0j}\partial x_{0j}} - g_{0i} \tag{2.18}$$

The container may undergo a motion with nonzero angular velocities or accelerations with respect to each axis at any instant of time. If a coordinate frame, x_1, is attached to the spacecraft undergoing this general motion, then three successive coordinate rotations will reflect this motion. The three coordinate rotations are performed in the following order (see Fig. 2.2). First, the x_0 coordinate rotates an angle ψ_3 counterclockwise about the x_{03} axis. This leads to an intermediate coordinate called $\bar{\bar{x}}_1$. Second, the $\bar{\bar{x}}_1$ coordinate rotates an angle ψ_2 counterclockwise about the $\bar{\bar{x}}_{12}$ axis. This leads to another intermediate coordinate called $\bar{x}_1$. Finally, the $\bar{x}_1$ frame makes another counterclockwise rotation of an angle ψ_1 about the $\bar{x}_{11}$ axis. This last rotation gives the desired coordinate x_1.

The relationship between the x_0 and x_1 coordinates can be expressed as:

$$x_{0i} = \alpha_{ij}x_{1j} \tag{2.19}$$

where α_{ij} represents the elements of a 3×3 transformation matrix resulting from the

above successive rotations. The elements of this transformation matrix are shown in Appendix A.

2.2.2 The elastic arm coordinates: x_2 coordinate system

Since the container is attached to a spacecraft by an elastic bar, another translation is required to move the origin of the x_1 coordinate to the location of the container by the length of the elastic bar h_i. This translation leads to a coordinate frame designated as x_2. The relationship between x_1 and x_2 is:

$$x_{2i} = x_{1i} - h_i \tag{2.20}$$

Eqs. (2.19) and (2.20) can be combined into a single equation relating the x_0 and x_2 frames. The relationship between x_0 and x_2 is

$$x_{2i} = \alpha_{ji} x_{0j} - h_i \tag{2.21}$$

or

$$x_{0i} = \alpha_{ij}(x_{2j} + h_j) \tag{2.22}$$

Applying the chain rule to the derivative terms in Eqs. (2.17) and (2.18), the following relationships between x_0 and x_2 frames were obtained:

$$\frac{\partial}{\partial x_{0i}} = \alpha_{ij} \frac{\partial}{\partial x_{2j}}$$

$$\frac{\partial^2}{\partial x_{0i}^2} = \alpha_{ij}\alpha_{ik} \frac{\partial^2}{\partial x_{2j} \partial x_{2k}} = \delta_{jk} \frac{\partial^2}{\partial x_{2j} \partial x_{2k}} = \frac{\partial^2}{\partial x_{2j} \partial x_{2j}}$$

$$\frac{\partial}{\partial t_0} = \frac{\partial}{\partial t_2} + [\dot{\alpha}_{ji}\alpha_{jk}(x_{2k} + h_k) - \dot{h}_i] \frac{\partial}{\partial x_{2i}}$$

The governing equations in the x_0 frame, i.e., Eqs. (2.17) and (2.18), can be written in terms of the new x_2 coordinates and new velocity components in the x_2 frame by using the above chain rule relationships. The new governing equations in the x_2 frame are:

$$\frac{\partial u_{2i}}{\partial x_{2i}} = 0 \tag{2.23}$$

$$\frac{\partial u_{2l}}{\partial t_2} - \dot{\alpha}_{il}\alpha_{ij}u_{2j} + [\dot{\alpha}_{ji}\alpha_{jk}(x_{2k} + h_k) - \dot{h}_i + u_{2i}]\frac{\partial u_{2l}}{\partial x_{2i}} = -\frac{1}{\rho}\frac{\partial p}{\partial x_{2l}} + \nu\frac{\partial^2 u_{2l}}{\partial x_{2j}\partial x_{2j}} - g_{2l} \tag{2.24}$$

where

$$u_{2i} = \alpha_{ji}u_{0j}$$

$$g_{2l} = \alpha_{il}g_{0i}$$

$$\dot{h}_i = \frac{dh_i}{dt}$$

$$\dot{\alpha}_{il} = \frac{d\alpha_{il}}{dt}$$

2.2.2.1 A new relative velocity in the x_2 frame A new relative velocity is defined as follows to permit a more convenient application of the boundary conditions and to facilitate interpretation of the solutions:

$$u_{2l'} = u_{2l} + \dot{\alpha}_{ji}\alpha_{jk}(x_{2k} + h_k) - \dot{h}_i$$

This new relative velocity is always zero at the wall of the container no matter what kind of motion the container may undergo. The introduction of this new relative velocity can greatly simplify the treatment of the boundary conditions. Substituting

the above definition of the relative velocity into Eqs. (2.23) and (2.24) and neglecting the l, we have the following equations written in terms of relative velocity components:

$$\frac{\partial u_{2i}}{\partial x_{2i}} = 0 \tag{2.25}$$

$$\frac{\partial u_{2l}}{\partial t_2} + u_{2i}\frac{\partial u_{2l}}{\partial x_{2i}} - 2\beta_{cr,li}u_{2i} - \beta_{t,li}(x_{2i} + h_i) - \beta_{cp,li}(x_{2i} + h_i)$$
$$= -\frac{1}{\rho}\frac{\partial p}{\partial x_{2l}} + \nu\frac{\partial^2 u_{2l}}{\partial x_{2j}\partial x_{2j}} - g_{2l} + E_l \tag{2.26}$$

where

$$\beta_{cr,li} = \dot{\alpha}_{jl}\alpha_{ji}$$

$$\beta_{t,li} = \ddot{\alpha}_{jl}\alpha_{ji}$$

$$\beta_{cp,li} = \dot{\alpha}_{kl}\dot{\alpha}_{ki} - \dot{\alpha}_{kl}\dot{\alpha}_{nj}\alpha_{kj}\alpha_{ni}$$

$$E_l = 2\dot{\alpha}_{il}\alpha_{ij}\dot{h}_j - \ddot{h}_l$$

$$\ddot{h}_l = \frac{d^2 h_l}{dt^2}$$

$$\ddot{\alpha}_{jl} = \frac{d^2\alpha_{jl}}{dt^2}$$

2.2.3 Free surface tracking coordinates: x_3 coordinate system

When the container undergoes a rotating-nutating motion, the free surface shape will change continuously with time. Equations (2.25) and (2.26) can be used to model this motion; however, a third coordinate rotation is preferred in this study for the following two reasons. First, the kinematic equation which is used in this study to update the free surface at each time step requires that the free surface height be a single-valued function of the other two coordinates. Therefore it is important to

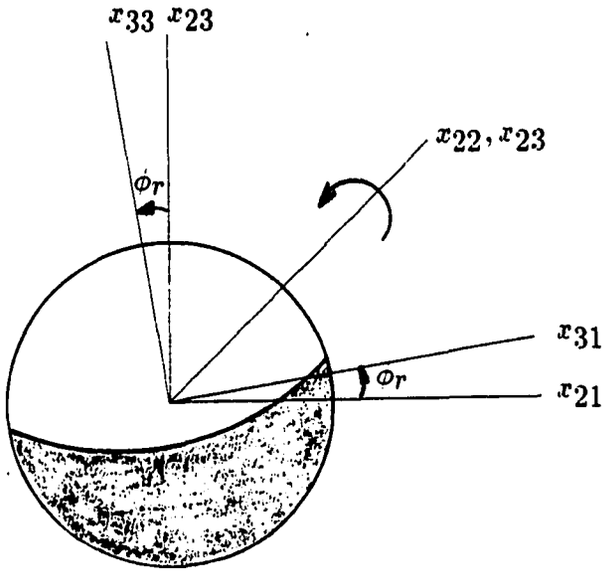

Figure 2.3: Notation for the S transformation

keep this free surface a single-valued function by rotating the coordinates as required at each computational time step. Second, rotating the coordinates in response to changes in the orientation of the free surface facilitates the establishment of the computational grid by the present algebraic grid generation scheme.

At any instant of time, the free surface may move to a new position with respect to the x_2 coordinates as shown in Fig. 2.3. It is desirable to have the x_{23} axis remain normal to the free surface in an average sense. One way to accomplish this is to let the x_2 coordinates rotate an angle ϕ_r counterclockwise about the x_{22} axis as shown in Fig. 2.3. A transformation matrix, S, is required to transform from the x_2 to the x_3 coordinates. The expression for this transformation matrix is also listed in

Appendix A. The relationship between the x_2 and x_3 coordinates is:

$$x_{2i} = s_{ij} x_{3j} \tag{2.27}$$

where s_{ij} is an element of S.

The chain rule is then applied to Eqs. (2.25) and (2.26) using Eq. (2.27) and the resulting governing equations in the x_3 coordinates are:

$$\frac{\partial u_{3i}}{\partial x_{3i}} = 0 \tag{2.28}$$

$$\frac{\partial u_{3n}}{\partial t_3} + (u_{3i} + f_{ij} x_{3j}) \frac{\partial u_{3n}}{\partial x_{3i}} - (f_{ni} + 2\lambda_{ni}) u_{3i} - \tau_{1,ni} x_{3i} - \tau_{2,ni} h_i = -\frac{1}{\rho} \frac{\partial p}{\partial x_{3n}} + \nu \frac{\partial^2 u_{3n}}{\partial x_{3j} \partial x_{3j}} - g_{3n} + E_n \tag{2.29}$$

where

$$u_{3j} = s_{ij} u_{2i}$$

$$g_{3n} = s_{ln} g_{2l}$$

$$f_{ij} = \dot{s}_{ki} s_{kj}$$

$$\lambda_{ni} = \beta_{cr,lj} s_{ji} s_{ln}$$

$$\tau_{1,ni} = (\beta_{t,lj} + \beta_{cp,lj}) s_{ln} s_{ji}$$

$$\tau_{2,ni} = (\beta_{t,li} + \beta_{cp,li}) s_{ln}$$

$$E_n = s_{ln} E_l$$

It should be noted that the application of this transformation introduces additional terms into the original governing equations. Careful attention must be paid to the evaluation of the elements of transformation matrix, s_{ij}, and its time rate, $\dot{s}_{ij}$, to avoid numerical instability. The treatment of these terms is described in the last test case regarding to the liquid sloshing results in Chapter 5.

2.2.4 Nondimensional form of the governing equations in the x_3 coordinate system

Equations (2.28) and (2.29) are dimensional equations. They can be nondimensionalized by properly choosing the characteristic quantities. Let the nondimensional quantities be defined as:

$$x_{3i}^* = \frac{x_{3i}}{L_{ref}} \qquad u_{3i}^* = \frac{u_{3i}}{V_{ref}} \qquad t^* = \frac{t}{t_{ref}} \qquad p^* = \frac{p - p_0}{p_{ref}} \tag{2.30}$$

where

L_{ref} = reference length = radius of the sphere

V_{ref} = reference velocity (will be defined later)

p_{ref} = reference pressure = ρV_{ref}^2

t_{ref} = reference time = $\dfrac{L_{ref}}{V_{ref}}$

p_0 = atmospheric pressure or saturated vapor pressure above the free surface

After replacing the dimensional quantities in Eqs. (2.28) and (2.29) by the nondimensional quantities in Eq. (2.30), the following nondimensional form of the governing equations in x_3 coordinates (the superscript $*$ has been dropped) is obtained:

$$\frac{\partial u_{3i}}{\partial x_{3i}} = 0 \tag{2.31}$$

$$\frac{\partial u_{3n}}{\partial t_3} + (u_{3i} + f_{ij}x_{3j})\frac{\partial u_{3n}}{\partial x_{3i}} - (f_{ni} + 2\lambda_{ni})u_{3i} - \tau_{1,ni}x_{3i} - \tau_{2,ni}h_i = -\frac{\partial p}{\partial x_{3n}} + \frac{1}{Re}\frac{\partial^2 u_{3n}}{\partial x_{3j}\partial x_{3j}} - g_{3n} + E_n \tag{2.32}$$

where Re is the Reynolds number and is defined as:

$$Re = \frac{V_{ref} L_{ref}}{\nu}$$

2.2.5 Generalized nonorthogonal coordinates: z coordinate system

Equations (2.31) and (2.32) are written in the noninertial Cartesian x_3 coordinates. However, it is very difficult to handle irregular boundaries such as the free surface and the spherical container wall in this coordinate system. It is desirable to establish a new coordinate system having the property that the coordinate lines fit the boundaries of the problem domain of interest, i.e., the liquid itself enclosed by the container wall and the free surface.

Let this new coordinate system be designated by (τ, z_i). The relationship between the (t_3, x_{3i}) and (τ, z_i) coordinate systems can be expressed as:

$$\tau = t_3 \tag{2.33}$$

$$z_i = z_i(x_{31}, x_{32}, x_{33}, t_3) \tag{2.34}$$

By applying the chain rule to the time and spatial derivative terms, we have:

$$\frac{\partial}{\partial x_{3i}} = \eta_{j,i} \frac{\partial}{\partial z_j}$$

$$\frac{\partial^2}{\partial x_{3i} \partial x_{3i}} = \eta_{j,i} \eta_{k,i} \frac{\partial^2}{\partial z_j \partial z_k} + \eta_{k,ii} \frac{\partial}{\partial z_k}$$

$$\frac{\partial}{\partial t_3} = \frac{\partial}{\partial \tau} + \dot{z}_i \frac{\partial}{\partial z_j}$$

where

$\eta_{i,j} = \dfrac{\partial z_i}{\partial x_{3j}}$,

$\eta_{i,jj} = \dfrac{\partial^2 z_i}{\partial x_{3j} \partial x_{3j}}$ are metric terms

and

$\dot{z}_i = \dfrac{\partial z_i}{\partial t_3}$ is the grid speed term.

Note that the definition of η has been changed in these three-dimensional equations. The final governing equations in generalized nonorthogonal coordinates are:

$$\eta_{j,i} \frac{\partial u_{3i}}{\partial z_j} = 0 \tag{2.35}$$

$$\begin{aligned} \frac{\partial u_{3n}}{\partial \tau} + (\dot{z}_j + \eta_{j,i} u_{3i} + \eta_{j,i} f_{ik} x_{3k}) \frac{\partial u_{3n}}{\partial z_j} - (f_{ni} + 2\lambda_{ni}) u_{3i} \\ -\eta_{j,n} \frac{\partial p}{\partial z_j} + \frac{1}{Re} (\eta_{j,i} \eta_{k,i} \frac{\partial^2 u_{3n}}{\partial z_j \partial z_k} + \eta_{k,ii} \frac{\partial u_{3n}}{\partial z_k}) \\ = -\tau_{1,ni} x_{3i} - \tau_{2,ni} h_i - g_{3n} + E_n, \end{aligned} \tag{2.36}$$

The definitions of the metric terms and the grid speed terms are as follows:

$$\eta_{1,1} = J(\zeta_{2,2}\zeta_{3,3} - \zeta_{2,3}\zeta_{3,2})$$

$$\eta_{1,2} = -J(\zeta_{1,2}\zeta_{3,3} - \zeta_{1,3}\zeta_{3,2})$$

$$\eta_{1,3} = J(\zeta_{1,2}\zeta_{2,3} - \zeta_{1,3}\zeta_{2,2})$$

$$\eta_{2,1} = -J(\zeta_{2,1}\zeta_{3,3} - \zeta_{2,3}\zeta_{3,1})$$

$$\eta_{2,2} = J(\zeta_{1,1}\zeta_{3,3} - \zeta_{1,3}\zeta_{3,1})$$

$$\eta_{2,3} = -J(\zeta_{1,1}\zeta_{2,3} - \zeta_{1,3}\zeta_{2,1})$$

$$\eta_{3,1} = J(\zeta_{2,1}\zeta_{3,2} - \zeta_{2,2}\zeta_{3,1})$$

$$\eta_{3,2} = -J(\zeta_{1,1}\zeta_{3,2} - \zeta_{1,2}\zeta_{3,1})$$

$$\eta_{3,3} = J(\zeta_{1,1}\zeta_{2,2} - \zeta_{1,2}\zeta_{2,1})$$

$$\eta_{i,jj} = \frac{\partial \eta_{i,j}}{\partial x_{3j}} = \eta_{k,j}\frac{\partial \eta_{i,j}}{\partial z_k}$$

$$\dot{z}_i = -\dot{x}_{3j}\eta_{i,j}$$

$$J = \frac{1}{\zeta_{1,1}(\zeta_{2,2}\zeta_{3,3} - \zeta_{2,3}\zeta_{3,2}) - \zeta_{1,2}(\zeta_{2,1}\zeta_{3,3} - \zeta_{2,3}\zeta_{3,1}) + \zeta_{1,3}(\zeta_{2,1}\zeta_{3,2} - \zeta_{2,2}\zeta_{3,1})}$$

where $\zeta_{i,j} = \frac{\partial x_{3i}}{\partial z_j}$ and $\dot{x}_{3i} = \frac{\partial x_{3i}}{\partial \tau}$.

3. BOUNDARY CONDITIONS

The role of the boundary conditions in the numerical solution procedure is extremely important. The boundary conditions clearly define the domain of interest and reflect the nature of the flow under consideration. It is those special conditions (equations) at the computational boundaries that guide the code to the desired solutions. Although the word "boundary conditions" is generally used in the literature as in this chapter title, it is believed that the designation "boundary equations" is really more descriptive than "boundary conditions" for the boundaries of a complicated problem like the present three-dimensional liquid sloshing configuration. It is those special "boundary equations" that govern the motion of the fluid particles at the boundaries. In general, they are not simple equations. It is known that solving the full unsteady Navier-Stokes equations is an initial and boundary value problem. Both initial and boundary conditions need to be specified. For a well-defined problem, the initial conditions usually can be easily specified. Starting from this initial condition, the flow afterward will be completely controlled by the Navier-Stokes equations and those special equations at the boundaries.

All boundary conditions are treated implicitly. In general, except for noslip boundaries, the governing equations are written at boundary points. This procedure usually requires field variables at the points outside the domain. The way the

unknowns at these extra points are determined varies with the boundary and flow types. The boundary conditions for the two-dimensional compressible and three-dimensional incompressible flows considered in this study were somewhat different. For the two-dimensional compressible flow results presented in this study, several different types of boundaries were involved. They include inflow, outflow, farfield, symmetry, periodic and wall boundaries. The treatment of the boundary condition for the two-dimensional compressible flow calculations will be discussed first in the following section. For the three-dimensional incompressible liquid sloshing calculation inside a partially filled spherical container considered in this study, there are only two types of boundaries, i.e., wall and free surface boundaries. Since the treatment of these boundaries is quite different from their two-dimensional compressible counterparts, it will be addressed in a separate section. It should be noted that only the concepts used in obtaining the boundary conditions (or equations) is discussed in this chapter. The detailed boundary condition implementation in the numerical procedure is described in Chapter 4.

3.1 Two-Dimensional Compressible Flows

For various two-dimensional compressible flow calculations considered in this study, the boundary conditions were specified as follows:

1. *Inflow boundary*

   For subsonic flows, u, v and T were specified at this boundary. However pressure was extrapolated from interior points due to the elliptic nature of the pressure signal propagation in the subsonic regime. For supersonic flows, all variables

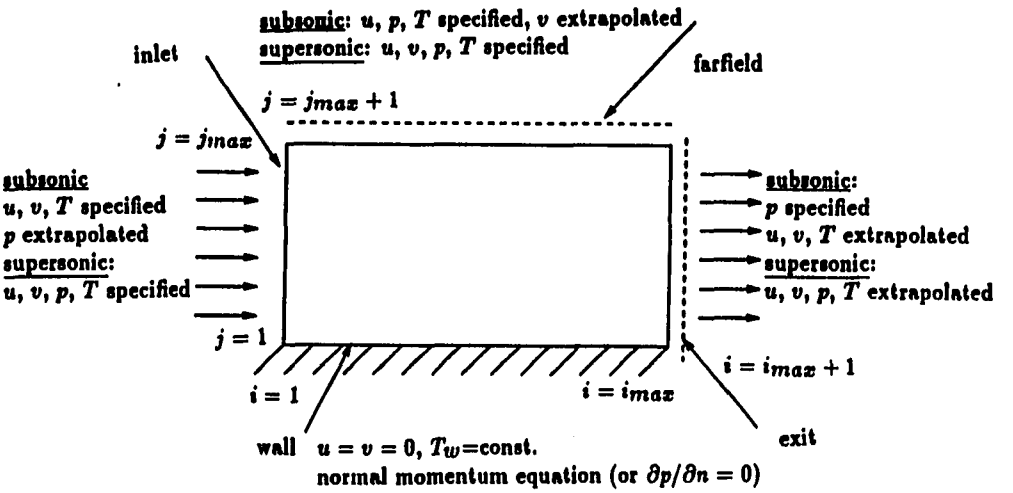

Figure 3.1: Boundary condition treatment for inflow, outflow, wall and farfield boundaries

must be specified (see Fig. 3.1).

2. *Outflow boundary*

For subsonic flows, the full Navier-Stokes equations were still written at the outflow boundary. The real boundary conditions were then technically specified at the points outside the computational domain (see Fig. 3.1). The freestream or atmospheric pressure was specified at this extra point and extrapolation was used to obtain values for other variables. For supersonic flows, all quantities were extrapolated from interior points.

3. *Farfield boundary*

The farfield boundary was chosen far enough from the object considered so that the influence of the location of this artificial boundary on the solutions was small. For subsonic flows, the full Navier-Stokes equations were still written at this boundary. Freestream velocity, pressure and temperature were specified at the point outside the computational domain (see Fig. 3.1) and the v component of velocity was obtained at this extra point from the continuity equation. For supersonic flows reported in this study, all variables were specified.

4. *Symmetry boundary*

If a line of symmetry exists in a flow, it is common practice to solve the problem for only one half of the domain using a symmetry boundary condition. The governing equations were written on the line of symmetry. All variables at the points outside the domain were obtained by the symmetry condition for u, p and T and the antisymmetry condition for v (see Fig. 3.2).

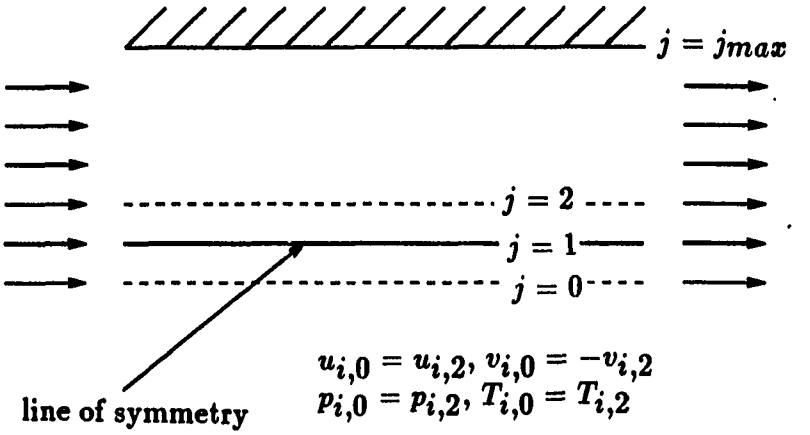

Figure 3.2: Boundary condition treatment for a symmetry boundary

5. *Periodic boundary*

In one of the two-dimensional compressible flow calculations, i.e., vortex shedding over a circular cylinder, and the three-dimensional incompressible liquid sloshing calculation, the condition of circumferential periodicity existed in the flow. The periodic condition was assured by overlapping the solutions for three constant θ lines (or planes in 3-D; see Fig. 3.3). The governing equations were still written at this boundary ($i = 1$ and $i = imax$).

6. *Wall boundary*

Instead of writing the governing equations at this boundary, noslip conditions were used for velocity components (see Fig. 3.1). Either fixed temperature or a specified heat flux condition was used for the boundary condition for T. For pressure, instead of specifying a zero pressure gradient condition, the favored treatment was to write the normal momentum equation at this boundary and apply the noslip conditions to simplify it. The resulting equation related the

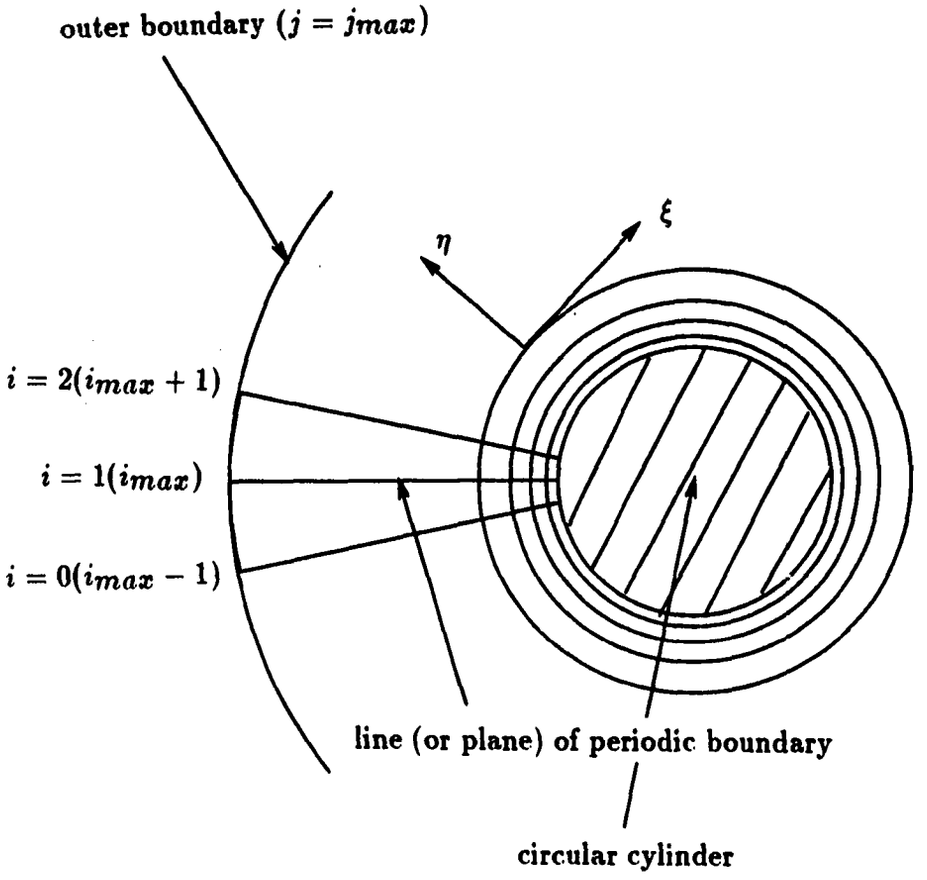

Figure 3.3: Boundary condition treatment for a periodic boundary

normal derivative of pressure to velocity derivative terms. The detailed implementation of this type of boundary condition will be presented in Chapter 4. This treatment will become more complicated for irregular or curvilinear boundaries but it may enhance the coupling between the pressure and velocity fields and eliminate spurious pressure solutions. This idea will be discussed further in the results section.

For internal steady flow calculations, the treatment of the pressure boundary condition at inflow and outflow deserves special attention. The pressure level calculated at the inflow boundary must be adjusted as the calculation proceeds if the specified inflow Reynolds number is to be maintained. The same adjustment must be applied to the pressure everywhere, including the outflow pressure. This pressure adjustment procedure maintains a constant and predetermined mass flow rate. Without this adjustment, the Reynolds number of the final converged solution may drift from the desired value. This drift was found to be more severe for low Reynolds number flows.

3.2 Three-Dimensional Incompressible Liquid Sloshing Flows

There are only two types of boundaries for this three-dimensional configuration. They are the solid wall of the container and the free surface. Four boundary equations are required at each boundary to close the system of equations since the Navier-Stokes equations consist of four equations for four unknowns. In the following sections the boundary equations for the two types of boundaries (solid wall and free surface) will be derived.

3.2.1 Wall boundary equations

At the wall of the spherical container, it is easy to specify three equations due to the zero relative motion between the fluid particles and the solid wall. These three boundary equations are:

$$u_{3i} = 0 \qquad i = 1, 2, 3 \tag{3.1}$$

The fourth equation is to provide a boundary condition for pressure and comes from conservation of momentum in the direction normal to the wall. This normal momentum equation is formed by performing the inner product of the *local* unit vector normal to the wall and the three momentum equations such as:

$$M_n = \vec{n} \cdot \vec{M}$$

where M_n represents the normal momentum equation, $\vec{n}$ is the *local* unit normal vector at the wall and $\vec{M}$ represents the three momentum equations in a vector form. The expression for the *local* unit normal vector at the wall is listed in Appendix B. The resulting normal momentum equation, after simplifying with Eq. (3.1), becomes

$$\eta_{j,n}\eta_{2,n}\frac{\partial p}{\partial z_j} = \{\tau_{1,ni}x_{3i} + \tau_{2,ni}h_i - g_{3n} + E_n - (\dot{z}_2 + \eta_{2,i}f_{ik}x_{3k})\frac{\partial u_{3n}}{\partial z_2}$$
$$+\frac{1}{Re}[\eta_{2,i}^2\frac{\partial^2 u_{3n}}{\partial z_2^2} + \eta_{2,ii}\frac{\partial u_{3n}}{\partial z_2} + 2\eta_{1,i}\eta_{2,i}\frac{\partial^2 u_{3n}}{\partial z_1 \partial z_2} + 2\eta_{2,i}\eta_{3,i}\frac{\partial^2 u_{3n}}{\partial z_2 \partial z_3}]\}\eta_{2,n} \tag{3.2}$$

It is assumed that the wall of the container coincides with the z_2 = constant surface in Eq. (3.2). As shown in this equation, the pressure boundary equation is not simple at all. However, due to the use of the index notation, the derivation of this equation is surprisingly straightforward. After differencing, all terms with dependent variables that fit into the 7-point molecule were treated implicitly. The numerical treatment of this boundary equation for pressure is discussed in more detail in Chapter 4.

3.2.2 Free surface boundary equations

Strictly speaking, five equations are needed at this boundary since one more equation is required for an additional unknown, i.e., the free surface position, which is part of the solution. This extra equation will be discussed in the following section. The so-called dynamic equations will be discussed first. These equations, which will be coupled with the Navier-Stokes equations for the interior points, are derived based on the following conditions. First, it is assumed that the two tangential shear stresses along the free surface are zero since no external tangential forces are applied to the surface. Second, the normal shear stress must be continuous across the free surface boundary, and finally, the continuity equation must be satisfied at this boundary. For the continuous normal stress condition, a further assumption for air is made that only the pressure contribution to the normal stress equation is retained, since the viscous stress contribution is small for air compared with similar terms for the liquid.

These four equations in nondimensional form are:

1. *Continuity equation*

$$\eta_{j,i}\frac{\partial u_{3i}}{\partial z_j} = 0 \tag{3.3}$$

2. *Zero tangential shear stress(two equations)*

$$\frac{\partial U_n}{\partial \tau_1} + \frac{\partial U_{\tau_1}}{\partial n} + U_{\tau_1}\kappa_1 = 0 \tag{3.4}$$

$$\frac{\partial U_n}{\partial \tau_2} + \frac{\partial U_{\tau_2}}{\partial n} + U_{\tau_2}\kappa_2 = 0 \tag{3.5}$$

3. *Continuous normal shear stress*

$$p - \frac{2}{Re}\frac{\partial U_n}{\partial n} - \frac{1}{We}\kappa = 0 \tag{3.6}$$

where

n denotes distance normal to the free surface ($\vec{n}$ is the unit normal vector)

τ_1 denotes distance along the 1st tangential direction at the free surface ($\vec{\tau}_1$ is the 1st unit tangential vector)

τ_2 denotes distance along the 2nd tangential direction at the free surface ($\vec{\tau}_2$ is the 2nd unit tangential vector)

U_n denotes velocity component along the $\vec{n}$ direction at the free surface

U_{τ_1} denotes velocity component along the $\vec{\tau}_1$ direction at the free surface

U_{τ_2} denotes velocity component along the $\vec{\tau}_2$ direction at the free surface

κ_1, κ_2 and κ denote *local* curvature terms

We is the Weber number and is defined as

$$We = \frac{\rho V_{ref}^2 L_{ref}}{\Gamma}$$

where Γ is the surface tension coefficient.

The definitions of the above quantities are listed in Appendix C. The numerical treatment for this boundary equation is discussed in more detail in Chapter 4.

3.2.3 Free surface kinematic equation

The free surface kinematic equation is derived from the Lagrangian point of view. Basically, it represents the fact that fluid particles which lie on the free surface must remain on it. Letting F be the free surface height which is a function of time , and the x_{31} and x_{32} coordinates, the condition that a particle on the free surface must remain on the free surface can be written as:

$$\frac{D}{Dt_2}\{F(x_{31}, x_{32}, t_3) - x_{33}\} = 0$$

Using the chain rule to express this in terms of the generalized nonorthogonal coordinates gives the following representation for the free surface kinematic condition:

$$\begin{aligned}\frac{\partial F}{\partial \tau} &= \{u_{33} + f_{3k}x_{3k}\} \\ &\quad -\{\dot{z}_1 + (u_{31} + f_{1k}x_{3k})\eta_{1,1} + (u_{32} + f_{2k}x_{3k})\eta_{1,2}\}\frac{\partial F}{\partial z_1} \\ &\quad -\{\dot{z}_2 + (u_{31} + f_{1k}x_{3k})\eta_{2,1} + (u_{32} + f_{2k}x_{3k})\eta_{2,2}\}\frac{\partial F}{\partial z_2} \qquad (3.7)\end{aligned}$$

In the above equation, the free surface coincides with the z_3 = constant surface.

So far the governing equations and boundary conditions for two and three-dimensional flows have been derived. The equations are expressed in terms of the so-called "primitive variables". The partial differential equations will be discretized and solved by a numerical method. The numerical solution algorithm is described in the next chapter.

4. NUMERICAL SOLUTION ALGORITHM

In this chapter, the numerical solution algorithm will be described. The discussion will cover the discretization method, the linearization method, the grid generation scheme, metric term evaluation, the boundary condition implementation, the artificial compressibility method for incompressible equations, the coupled strongly implicit procedure, the convergence acceleration technique, the convergence criterion and the solution procedure. These topics will be described one by one.

4.1 Discretization Method

The governing equations written in a generalized nonorthogonal coordinate system for two-dimensional compressible flows, Eq. (2.14), and three-dimensional incompressible flows, Eqs. (2.35) and (2.36), contain five types of terms: time derivative terms, first order spatial derivative terms, second order derivative terms, second order cross derivative terms and source terms. The discretization method for each type of derivative term is described as follows. It should be noted that the following discretization methods, in general, were applied to the interior points only. The equations written at the boundary points (boundary equations), were discretized in different ways and are described in the the section entitled "the boundary condition implementation" in this chapter.

1. *Time terms*

Letting ϕ be a general dependent variable, a first-order accurate forward difference was used such as:

$$(\frac{\partial \phi}{\partial t})^{n+1} = \frac{1}{\Delta t}(\phi^{n+1} - \phi^{n})$$

Note: Unless otherwise noted, no subscript for the dependent variable, ϕ, means that it is evaluated at the center point, i.e., (i, j) for two-dimensional equations or (i, j, k) for three-dimensional equations. Furthermore, only those subscripts that are incremented from the (i,j,k) level will be shown. For example, $\phi^{n+1}_{i+1,j,k}$ will be written as ϕ^{n+1}_{i+1}.

2. *First-order spatial derivative terms*

A second-order central difference formula was used for these terms such as:

$$(\frac{\partial \phi}{\partial \xi})^{n+1} = \frac{1}{2}(\phi^{n+1}_{i+1} - \phi^{n+1}_{i-1})$$

$$(\frac{\partial \phi}{\partial \eta})^{n+1} = \frac{1}{2}(\phi^{n+1}_{j+1} - \phi^{n+1}_{j-1})$$

where, $\Delta\xi = \Delta\eta = 1$ is assumed.

3. *Second-order spatial derivative terms*

A second-order central difference formula was used for these terms such as:

$$(\frac{\partial^2 \phi}{\partial \xi^2})^{n+1} = (\phi^{n+1}_{i+1} - 2\phi^{n+1} + \phi^{n+1}_{i-1})$$

$$(\frac{\partial^2 \phi}{\partial \eta^2})^{n+1} = (\phi^{n+1}_{j+1} - 2\phi^{n+1} + \phi^{n+1}_{j-1})$$

However the following difference method was used for the second-order spatial derivative terms appearing in the two-dimensional compressible equations:

$$\frac{\partial}{\partial\xi}(a\frac{\partial\phi}{\partial\xi})^{n+1} = (a\frac{\partial\phi}{\partial\xi})^{n+1}_{i+1/2} - (a\frac{\partial\phi}{\partial\xi})^{n+1}_{i-1/2}$$

where $i+1/2$ indicates a location halfway between i and $i+1$ and $i-1/2$ denotes a location halfway between $i-1$ and i and a represents a combination of metric terms and viscosity in the viscous terms in the momentum equations and the coefficient to the conduction terms in the energy equation. The values of $a_{i+1/2}$ and $a_{i-1/2}$ were determined as follows:

$$a_{i+1/2} = \frac{1}{2}(a_i + a_{i+1})$$

$$a_{i-1/2} = \frac{1}{2}(a_i + a_{i-1})$$

The first-order derivative terms at the half nodal point were evaluated as follows:

$$(\frac{\partial\phi}{\partial\xi})^{n+1}_{i+1/2} = \phi^{n+1}_{i+1} - \phi^{n+1}_i$$

$$(\frac{\partial\phi}{\partial\xi})^{n+1}_{i-1/2} = \phi^{n+1}_i - \phi^{n+1}_{i-1}$$

Similar expressions for the terms in the η direction were evaluated in the same way.

4. *Second-order spatial cross derivative terms*

A second-order central difference formula was used for these terms such as:

$$\frac{\partial}{\partial\xi}(\frac{\partial\phi}{\partial\eta})^{n+1} = \frac{1}{4}(\phi^{n+1}_{i+1,j+1} - \phi^{n+1}_{i+1,j-1} - \phi^{n+1}_{i-1,j+1} + \phi^{n+1}_{i-1,j-1})$$

In this section, only terms with notation used in the two-dimensional equations are shown; however similar terms in three-dimensional equations were evaluated in the same way and will not be repeated.

4.2 Linearization Method

All nonlinear terms were linearized by a Newton method [7]. The representation for typical nonlinear terms such as the time term in the continuity equation of the two-dimensional equations and one of the convective terms in the momentum equation of the three-dimensional incompressible equations are illustrated as:

$$(\frac{p}{T})^{n+1} \simeq (\frac{1}{\overline{T}})^{n+1} p^{n+1} - (\frac{\overline{p}}{\overline{T}^2})^{n+1} T^{n+1} + (\frac{\overline{p}}{\overline{T}})^{n+1} \tag{4.1}$$

$$(u_{3i}\frac{\partial u_{3n}}{\partial z_j})^{n+1} \simeq (\bar{u}_{3i})^{n+1}(\frac{\partial u_{3n}}{\partial z_j})^{n+1} + (\overline{\frac{\partial u_{3n}}{\partial z_j}})^{n+1}(u_{3i})^{n+1} - (\bar{u}_{3i}\overline{\frac{\partial u_{3n}}{\partial z_j}})^{n+1} \tag{4.2}$$

where $(\overline{p})^{n+1}$, $(\overline{T})^{n+1}$, $(\bar{u}_{3i})^{n+1}$ and $(\overline{\frac{\partial u_{3n}}{\partial z_j}})^{n+1}$ are values from the previous iteration level of the current time level, $n+1$.

The linearization error can be effectively removed by doing subiterations at each time level. It should be noted that an equivalent formulation can be developed using conventional Jacobian matrices [7] for the system of equations. This equivalence is shown in Appendix D.

All terms containing the dependent variables were treated implicitly and put on the left hand side (LHS) of the equations to form the coefficient matrix except for the cross derivative terms in the viscous terms of the momentum equations and the

viscous dissipation terms in the energy equation. These terms were lagged to the right hand side (RHS) of the equations and were evaluated at the previous iteration level of the current time step. For the three-dimensional equations, several source terms arising due to the coordinate rotation and gravity were evaluated on the RHS.

The linearization procedure for each term in the two-dimensional governing equations is somewhat tedious but straightforward. For the three-dimensional equations, only one of the convective terms needs to be linearized. The use of index notation in the three-dimensional equations not only simplifies the derivation of the final form of the governing equations, but also helps in the development of a compact three-dimensional code.

After carrying out the above linearization procedure, the four dependent variables at the current time level, $n+1$, appear in each of the four equations. At each nodal point there are four coupled equations which can be used to solve for the four dependent variables simultaneously. Also, the coupling of the unknowns in the entire 2-D or 3-D computational domain is assured when applying the coupled strongly implicit procedure to solve the resulting algebraic system of equations. This procedure will be described later in this chapter.

4.3 Grid Generation Scheme

For all geometries considered in this study the grids were generated by algebraic means. Grid clustering was achieved near boundaries when needed by using the following Roberts transformation listed in [7]:

$$y^* = \alpha + (1-\alpha)\frac{ln(\{\beta + [y(2\alpha+1)/h] - 2\alpha\}/\{\beta - [y(2\alpha+1)/h] + 2\alpha\})}{ln[(\beta+1)/(\beta-1)]} \qquad (4.3)$$

where y^* is a coordinate in the transformed domain, y is a coordinate in the physical domain and h is the maximum value in y direction.

For this transformation, if $\alpha = 0$ the mesh will be refined near $y = h$ only, whereas, if $\alpha = 0.5$ the mesh will be refined equally near $y = 0$ and $y = h$ (see Fig. 4.1). In the actual computation the inverse transformation of Eq. (4.3) is more useful. The inverse transformation is:

$$y = h\frac{(\beta + 2\alpha)[(\beta + 1)/(\beta - 1)]exp[(y^* - \alpha)/(1 - \alpha)] - \beta + 2\alpha}{(2\alpha + 1)\{1 + [(\beta + 1)/(\beta - 1)]exp[(y^* - \alpha)/(1 - \alpha)]\}} \tag{4.4}$$

In Eqs. (4.3) and (4.4), β is a stretching parameter for controlling the grid clustering. Its value should be greater than one. As β increases, the distribution of the grid becomes more and more uniform.

With a slight modification, Eq. (4.4) can also be used to control the grid stretching in a curvilinear coordinate system. For example, in the circular cylinder case considered in this study, Eq. (4.4) was modified to cluster the grid in both the circumferential and radial directions by changing y to θ and r respectively in the above equation. The grid layout for different problems generated by the variation of Eq. (4.4) will be shown in the results chapter.

For the three-dimensional liquid sloshing flow calculations, the grid generation was not a simple task. The major difficulty in generating grids for this flow arises from the combination of the wall of the spherical container and the irregular geometry of the free surface which is moving in time. It is a formidable job to generate an ideal grid in this case, since almost any choice of grid system is bound to encounter difficulties in high grid skewness, high aspect ratio and singularities somewhere in the domain of interest. Use of a general three-dimensional grid generation code, such

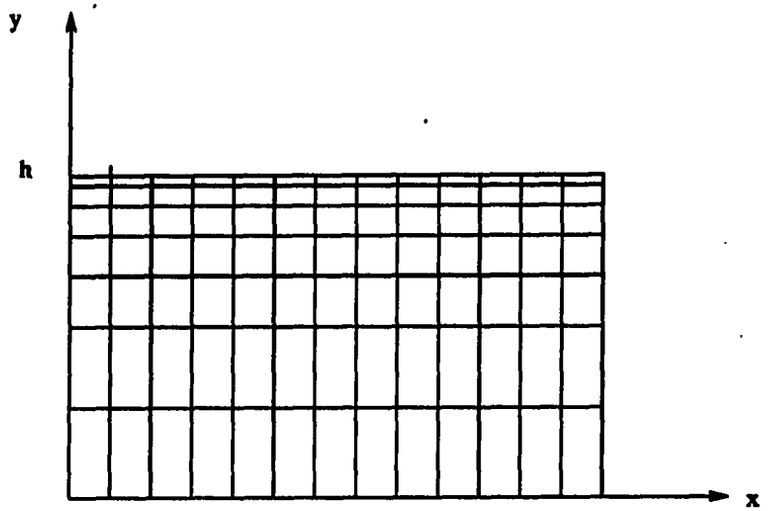

(a) $\alpha = 0$

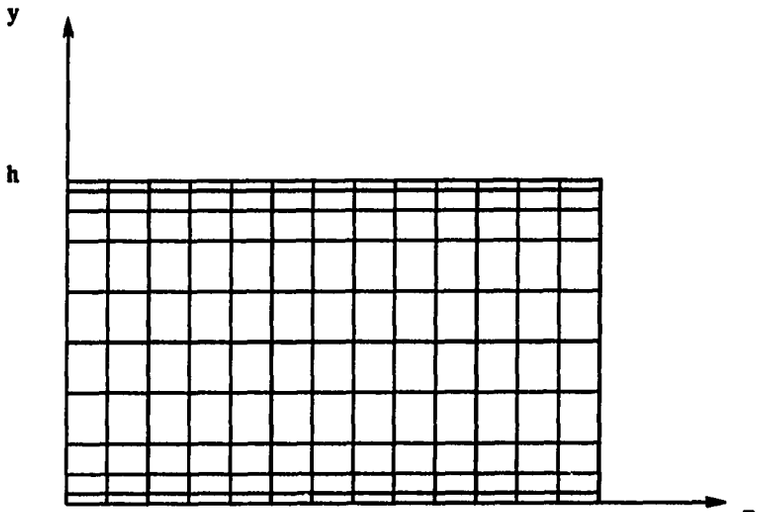

(b) $\alpha = 0.5$

Figure 4.1: Grid clustering demonstration for $\alpha = 0$ and 0.5

as 3DGRAPE [52], which provides a capability for controlling the grid skewness, stretching and orthogonality, was initially considered for this case. However, since a new grid must be generated at every time step in this unsteady calculation (and hence 3DGRAPE would need to be called to do this in every time step), it was anticipated that a tremendous amount of computer time would be required in this part of the calculation. Furthermore, it was believed that some of the difficulties mentioned above would still exist even with the use of 3DGRAPE. Therefore, 3DGRAPE was abandoned and a simple algebraic method, which can match the free surface shape at any instant of time and adapt all or part of the grid to follow the free surface, was finally developed to generate grids for this case without solving complicated partial differential equations. This grid generation scheme was very easy to use and was efficient. Only a tiny fraction of CPU time was spent in this part of calculation. However, the scheme still suffered from the above grid problems to some extent. This grid generation scheme will be briefly described below.

4.3.1 Grid Generation For Three-Dimensional Liquid Sloshing Flows

The grid system for this case can be seen in Fig. 4.2. In order to fit the boundaries easily on both the free surface and the wall of the spherical container, a cylindrical coordinate-like grid system was adopted here. At each plane of constant x_{33}, a two-dimensional grid was generated with the grid stretching in the radial direction by Eq. (4.4) and a uniform $\Delta\theta$ increment in the circumferential direction. Eq. (4.4) was also used for controlling the grid stretching in the x_{33} direction.

At time zero the free surface is flat and normal to the x_{33} axis. The container is started in a motion and therefore the free surface begins to change its shape. After the

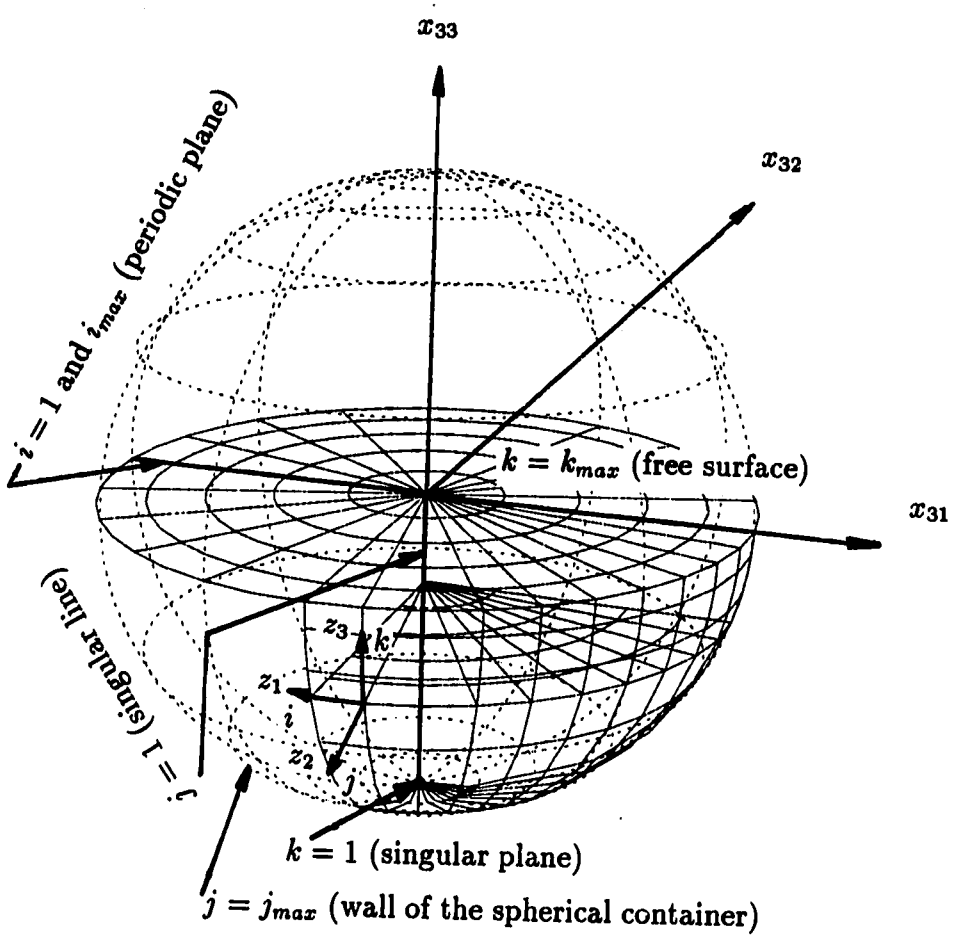

Figure 4.2: Coordinate system for liquid sloshing problem

first time step, a new free surface is calculated by solving the free surface kinematic equation, i.e., Eq. (3.7) and this new free surface is no longer flat.

A new grid has to be generated for the new physical domain under this new free surface. Since the free surface could be of any arbitrary shape at any instant of time, the following grid adaptation strategy was used to follow the free surface shape with the grid generation technique mentioned earlier.

1. Locate the x_{23} coordinate of the highest free surface point, say z_{high} (see Fig. 4.3).

2. Calculate the free surface tracking angle, ϕ_r, and rotate counterclockwise the x_{21} and x_{23} axes by this angle (see Fig. 4.3). The new coordinate system after this rotation is denoted as the x_3 coordinate system. The rotation angle, ϕ_r, is shown in Fig. 4.3. It is the angle formed by the horizontal axis, x_{21}, and the line formed by connecting two free surface points at the wall of the tank at the $x_{22} = 0$ plane.

3. Construct a horizontal plane which is orthogonal to the x_{33} axis and passes through z_{high}. This plane should form a circular plane after intersecting with the wall of the spherical container (see Fig. 4.3).

4. Generate a provisional three-dimensional grid for the domain enclosed by this circular plane ($k = k_{max}$ plane) and the wall of the container by the algebraic grid generation technique mentioned earlier. This provisional grid (see Fig. 4.3) does not have the correct free surface height (except at the highest free surface point) and does not have the final x_{33} coordinate for all grid points. However this provisional grid will match with the new free surface shape and all grid

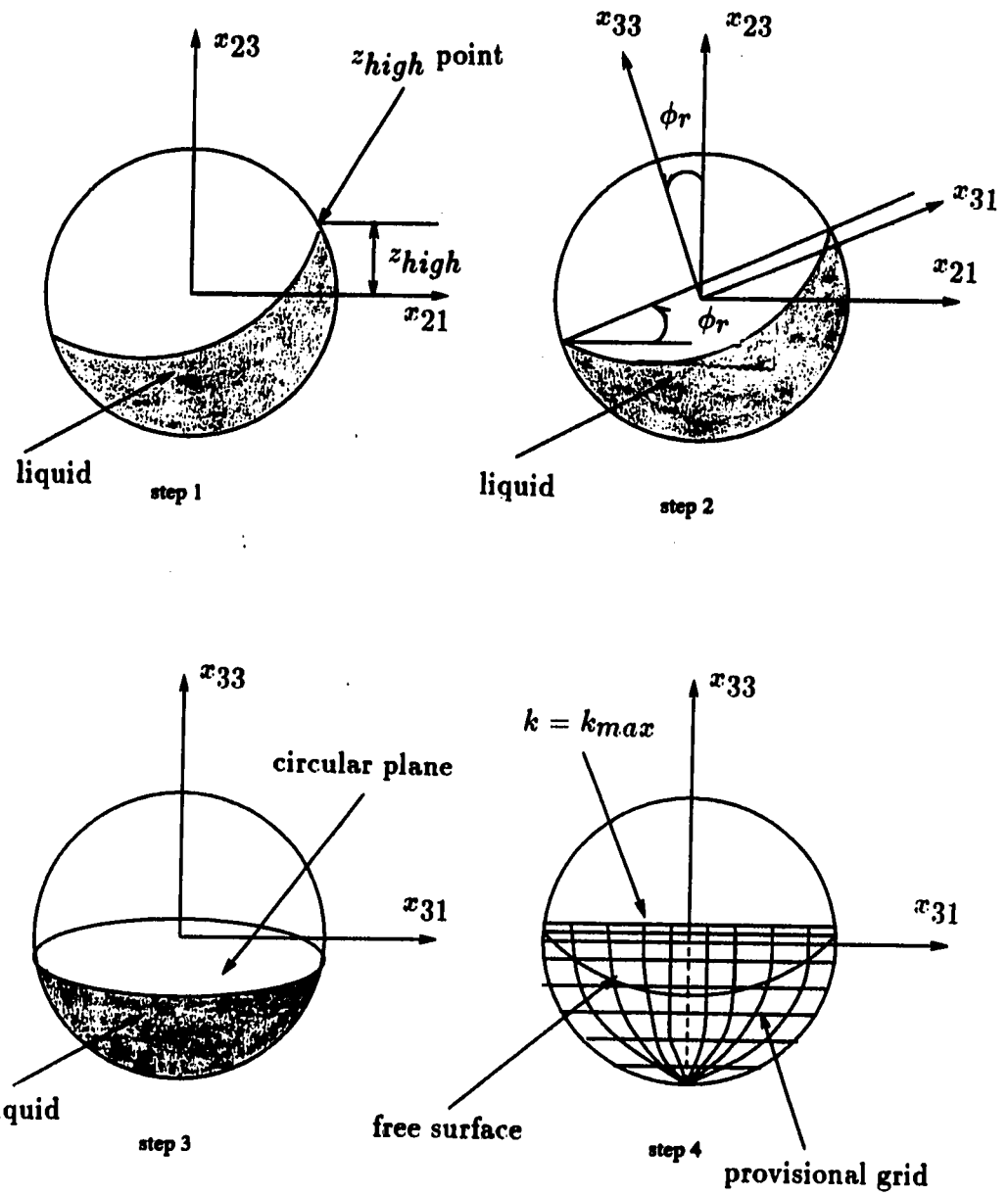

Figure 4.3: Basic grid generation procedure for 3-D liquid sloshing problem

points below this free surface will gradually adjust its coordinates to follow the free surface smoothly after the following grid adaptation procedure is complete.

5. Interpolate the corresponding free surface height for each provisional grid point at the $k = k_{max}$ plane based on the free surface height which is obtained from the free surface kinematic equation, Eq. (3.7). One-dimensional linear interpolation for the free surface height along the radial direction was used to complete this procedure for each θ direction. This procedure is necessary because the x_{31} and x_{32} coordinates of the provisional grid points and those of the original grid points at the free surface are different. The location of the free surface at the wall of the container remains unchanged. So far, new grid points at the free surface have been generated at this step.

6. Adjust the x_{33} coordinate (height) for every grid point of the provisional grid from level $k = 2$ to $k = k_{max-1}$ by the following formula:

$$x_{33})_{i,j,k} = x_{33})^{p}_{i,j,k} - (\chi)_{i,j,k}(\Delta z)_{i,j,k_{max}} \tag{4.5}$$

where $x_{33})^{p}_{i,j,k}$ is the *local* provisional x_{33} coordinate, $(\Delta z)_{i,j,k_{max}}$ is the *local* x_{33} coordinate difference between the free surface and the highest point of the provisional grid, z_{high}, (see Fig. 4.4) and $(\chi)_{i,j,k}$ is a *local* multiplication factor which linearly decreases the amount of height adjustment for all provisional grids from one at the free surface to zero at the bottom of the container. The expression for $(\chi)_{i,j,k}$ is

$$(\chi)_{i,j,k} = \frac{z - z_0}{z_{high} - z_0} \tag{4.6}$$

where z_0, z_{high} and z are defined in Fig. 4.4.

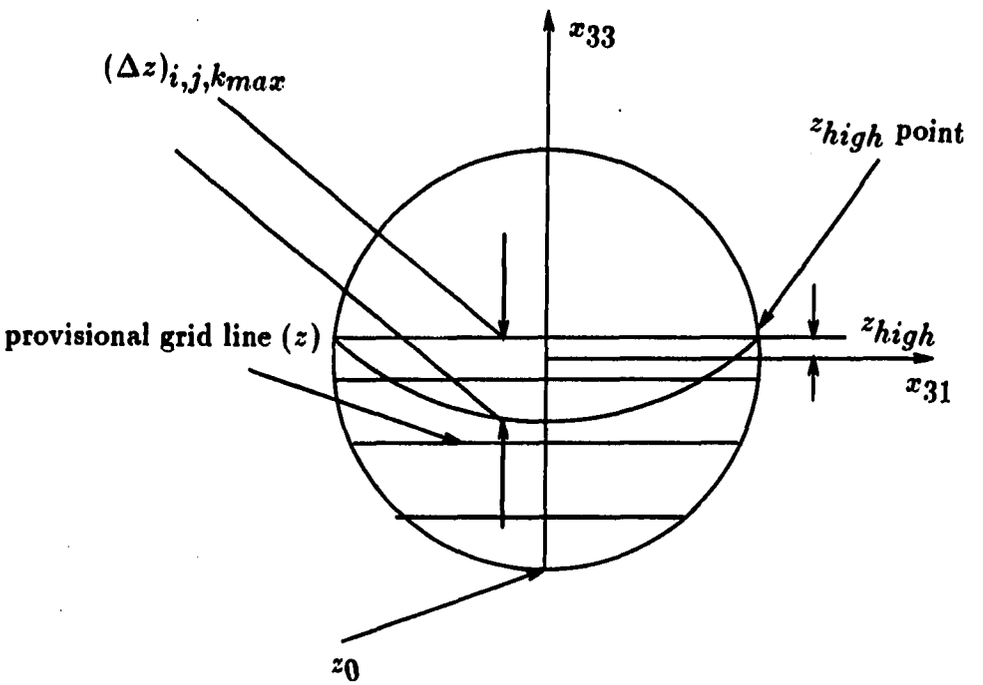

Figure 4.4: Notation for grid adjustment step

7. Adjust the x_{31} and x_{32} coordinates of the grid points at the wall of the container based on the new x_{33} coordinate at the wall. This procedure is necessary because the adjustment at step 6 does not account for the geometry of the wall.

4.4 Metric Term Evaluation

To satisfy the so-called geometry conservation law when the governing equations are written in a strong conservation law form, Hindman [53] showed that the metric terms, such as ξ_x, ξ_y, η_x, ... J,..., etc., should be evaluated with the same differencing scheme used for the spatial derivative terms in the governing equations. All

metric terms were therefore evaluated by a second order central difference formula in accordance with the discretization scheme described above. A typical term such as x_ξ was represented as follows:

$$x_\xi = \frac{1}{2}(x_{i+1} - x_{i-1})$$

For the boundary points, a central difference formula was still used. This required an extra point outside the domain which was determined by a simple one-dimensional extrapolation from the interior points such as:

$$\chi)_{imax+1} = 3\chi)_{imax} - 3\chi)_{imax-1} + \chi)_{imax-2}$$

where χ is either x, y or z. This practice is actually identical to the use of a 3-point second order one-sided difference within the domain; however, it it much simpler to program the procedure that utilizes extrapolation, especially for a three-dimensional code, since metric terms at the boundary points are then calculated by the same formula as those at the interior points.

The metric terms, $\eta_{j,i}$ and $\eta_{j,ii}$, defined in the three-dimensional flows were calculated in exactly the same way as above. However, adjustments were needed at two types of singular points that exist in the current coordinate system. The first type of singularity occurs at $j = 1$ and $k = 2$ to k_{max}. These points all have the same coordinates for $i = 1$ to i_{max}. The second type of singularity occurs at $k = 1$ where points from $i = 1$ to i_{max} and $j = 1$ to j_{max} all have the same coordinates. The first type of singularity occurs because a line has been shrunk to a point; however, at the second singularity, a surface has been shrunk to a point. Special treatment was required for calculating metric terms at these singular points. Fortunately, it was only necessary to evaluate metric terms at two singular points in the present formulation.

These were the points at the center of the free surface (i, 1, k_{max}) and at the bottom point of the container (i, j, 1). The metric terms at the center point of the free surface were required in the implementation of the free surface stress boundary conditions. A simple average of the metric terms at neighboring points on the free surface was used for that point in this study. At the bottom of the container the metric terms were required in the implementation of the pressure wall boundary condition. Fortunately, the grid line $j = 1$, was always normal to the wall at that point due to the use of the x_3 coordinate transformation. This property ensured that the x_{33} momentum equation written in the physical domain became the normal momentum equation and hence could be used at this boundary point directly without using any metric quantities. However, nonuniform differencing had to be used to represent the spatial derivative terms.

First-order differencing was used to evaluate the grid speed terms $\dot{z}$ for all points. This involves evaluating a term such as:

$$\dot{x}_{3i} = \frac{\partial x_{3i}}{\partial \tau} = \frac{1}{\Delta \tau}(x_{3i}^{n+1} - x_{3i}^{n})$$

4.5 The Boundary Condition Implementation

As will be described later, the coupled strongly implicit procedure was used to solve the algebraic system of equations. All boundary conditions (equations) were coupled into the system of equations and solved fully implicitly. This treatment is believed to be more robust and straightforward than the explicit treatment of the boundary conditions or the treatment used in the ADI type of scheme in which some of the boundary conditions must be evaluated on the RHS. Some specific implementations of boundary conditions are briefly described as follows.

4.5.1 Extrapolation

As mentioned earlier in the section on boundary conditions, extrapolation was used to obtain variables at the extra points outside the computational domain. The following second order extrapolation formula was used for the point outside the computation domain:

$$\phi)_p = 3\phi)_{p-1} - 3\phi)_{p-2} + \phi)_{p-3}$$

or

$$\phi)_p = 3\phi)_{p+1} - 3\phi)_{p+2} + \phi)_{p+3}$$

depending on the location of p. In the above extrapolation ϕ represents a dependent variable and p indicates the spatial location of the variable. For example, for two-dimensional flows, the pressure at the inlet (p_1) was extrapolated from the interior points as:

$$p_1 = 3p_2 - 3p_3 + p_4$$

and the u velocity at one station outside the domain (u_{imax+1}) was extrapolated from the interior points as:

$$u_{imax+1} = 3u_{imax} - 3u_{imax-1} + u_{imax-2}$$

The above second-order extrapolation is indeed the Lagrangian formula applied for the computational domain where a uniform grid spacing is assumed. This treatment is actually identical to the use of a 3-point second order one-sided difference for the first-order spatial derivative terms at the boundary points.

For some cases (free surface height and pressure at the edge of the free surface, see next subsections), the extrapolations were done in the physical domain. The

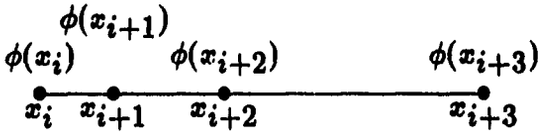

Figure 4.5: Notation for the Lagrangian formula

Lagrangian formula for a nonuniform grid spacing (physical domain) (see Fig. 4.5) was used. It can be expressed as:

$$\phi(x_i) = a\phi(x_{i+1}) + b\phi(x_{i+2}) + c\phi(x_{i+3}) \tag{4.7}$$

where

$$a = \frac{(x_i - x_{i+2})(x_i - x_{i+3})}{(x_{i+1} - x_{i+2})(x_{i+1} - x_{i+3})}$$
$$b = \frac{(x_i - x_{i+3})(x_i - x_{i+1})}{(x_{i+2} - x_{i+3})(x_{i+2} - x_{i+1})}$$
$$c = \frac{(x_i - x_{i+1})(x_i - x_{i+2})}{(x_{i+3} - x_{i+1})(x_{i+3} - x_{i+2})}$$

4.5.2 Flow variables at the singular points

For 3-D flows, special treatment was required due to coordinate singularities occurring at boundaries. Instead of deriving a special governing equation at the $j = 1$ singular line, the above extrapolation scheme was applied in the computational domain to obtain flow variables. It was expressed as:

$$\phi)_{j=2}^{\theta+\pi} = 3\phi)_{j=1}^{\theta} - 3\phi)_{j=2}^{\theta} + \phi)_{j=3}^{\theta} \tag{4.8}$$

where $\theta + \pi$ is the location at 180 degrees from the point of interest θ (see Fig. 4.6) and ϕ represents the flow variables. After the solution had been obtained, the flow

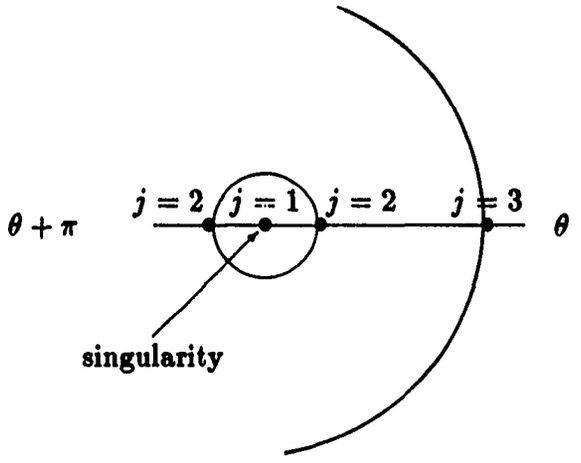

Figure 4.6: Notation for the extrapolation at $j = 1$

variables at the $j = 1$ singular line were determined from Eq. (4.8) which can be expressed as:

$$\phi)^{\theta}_{j=1} = \frac{1}{3}[3\phi)^{\theta}_{j=2} - \phi)^{\theta}_{j=3} + \phi)^{\theta+\pi}_{j=2}] \tag{4.9}$$

The ϕ's evaluated from Eq. (4.9) for all i's (circumferential direction) were then averaged to obtain the final value.

For $k = 1$, the pressure boundary equation at the wall of the container can not be directly used because of the singularity (no metric terms exist). The x_{33} component of the momentum equation written in the physical domain was applied at this point in place of Eq. (3.2) due to the fact that the x_{33} axis is always normal to the wall of the container at this point in the x_3 coordinate system. After applying the noslip condition at this point to simplify the equation, the following expression for the pressure boundary condition at the point $k = 1$ results:

$$\frac{\partial p}{\partial x_{33}} = -f_{3j}x_{3j}\frac{\partial u_{33}}{\partial x_{33}} + \tau_{1,3i}x_{3i} + \tau_{2,3i}h_i - g_{3,3} + \frac{1}{Re}\frac{\partial^2 u_{33}}{\partial x_{33}^2} + E_3 \tag{4.10}$$

A one-sided nonuniform differencing formula was used to represent the derivative terms in the above equation. The above equation was applied to obtained the pressure at the $k = 1$ point after the flow solution had been obtained.

4.5.3 Free surface

In order to apply the shear stress equations at the free surface boundary, a *local* unit normal and two unit tangential vectors need to be determined. The expressions for these unit vectors at the free surface are given in Appendix C. After the unit vectors are defined, the shear stress equations then must be decomposed from the *local* coordinates (n, τ_1, τ_2) to the *global* coordinates, x_3 and the generalized nonorthogonal coordinates, z. The following equalities were used to relate these coordinates:

$$U_{\tau_1} = \vec{V} \cdot \hat{\tau}_1 = u_{3i}\tau_{1i}$$

$$U_{\tau_2} = \vec{V} \cdot \hat{\tau}_2 = u_{3i}\tau_{2i}$$

$$U_n = \vec{V} \cdot \hat{n} = u_{3i}n_i$$

and

$$\frac{\partial U_{\tau_1}}{\partial n} = \nabla U_{\tau_1} \cdot \hat{n} = \frac{\partial U_{\tau_1}}{\partial x_{3i}} n_i = \frac{\partial (u_{3i}\tau_{1i})}{\partial x_{3j}} n_j = \eta_{k,j} \frac{\partial (u_{3i}\tau_{1i})}{\partial z_k} n_j$$

$$\frac{\partial U_n}{\partial \tau_1} = \eta_{k,j} \frac{\partial (u_{3i}n_i)}{\partial z_k} \tau_{1j}$$

$$\frac{\partial U_n}{\partial \tau_2} = \eta_{k,j} \frac{\partial (u_{3i}n_i)}{\partial z_k} \tau_{2j}$$

$$\frac{\partial U_{\tau_2}}{\partial n} = \eta_{k,j} \frac{\partial (u_{3i}\tau_{2i})}{\partial z_k} n_j$$

After applying the above relationships to the shear stress equations, the following equations written in generalized coordinates are obtained:

$$[(n_i\tau_{lj}+n_j\tau_{li})\eta_{k,j}]\frac{\partial u_{3i}}{\partial z_k}+[(\tau_{lj}\frac{\partial n_i}{\partial z_k}+n_j\frac{\partial \tau_{li}}{\partial z_k})\eta_{k,j}]u_{3i}+u_{3i}\tau_{li}\kappa_l=0 \qquad (4.11)$$

where l is 1 for the first tangential stress equation and l is 2 for the second tangential stress equation. The normal shear stress equation becomes:

$$p-\frac{2}{Re}[n_in_j\eta_{k,j}\frac{\partial u_{3i}}{\partial z_k}+\eta_{k,j}n_j\frac{\partial n_i}{\partial z_k}u_{3i}]-\frac{\kappa}{We}=0 \qquad (4.12)$$

where i,j and k range from 1 to 3 respectively.

Second-order central differences were used to represent the spatial derivative terms in Eqs. (4.11) and (4.12) in the z_1 and z_2 directions (parallel to the free surface) and first-order one-sided backward differences were used to represent the derivatives terms in the z_3 direction (normal to the free surface). The continuity equation which was also used at the free surface boundary was differenced in the same way. These four equations were coupled with the governing equations written at the interior points and solved simultaneously.

The free surface kinematic equation, Eq. (3.7), was used to explicitly determine a new free surface position after the flow solution for the entire domain was obtained. The new free surface function F was obtained by the following expression:

$$\begin{aligned} F^{n+1} &= F^n+\Delta\tau(\{u_{33}+f_{3k}x_{3k}\} \\ &\quad -\{\dot{z}_1+(u_{31}+f_{1k}x_{3k})\eta_{1,1}+(u_{32}+f_{2k}x_{3k})\eta_{1,2}\}\frac{\partial F}{\partial z_1} \\ &\quad -\{\dot{z}_2+(u_{31}+f_{1k}x_{3k})\eta_{2,1}+(u_{32}+f_{2k}x_{3k})\eta_{2,2}\}\frac{\partial F}{\partial z_2}) \end{aligned} \qquad (4.13)$$

Central differences were usually used to represent the spatial derivative terms in the above equation. However, for one of the cases investigated in this liquid sloshing

study, upwind differences were also used to represent these terms to suppress a saw-toothed profile in the free surface. The effect of this upwind differencing and the free surface smoothing is also discussed in Chapter 5.

Equation (4.13) is only valid for the interior points. At the edge of the free surface, i.e., $i = 1, imax$, $k = kmax$ and $j = jmax$, the Lagrangian extrapolation formula, Eq. (4.7), was used in the z_2 (radial) direction to obtain the free surface positions for all θ directions from the free surface position at the interior points.

4.5.4 Pressure at the wall

The implementation of the pressure boundary equation at the wall (especially how this equation was coupled into the governing equations) will be explained in this section. Equation (3.2) was rearranged as:

$$\eta_{j,n}\eta_{2,n}\frac{\partial p}{\partial z_j} + \eta_{2,n}(\dot{z}_2 + \eta_{2,i}f_{ik}x_{3k})\frac{\partial u_{3n}}{\partial z_2} - \frac{\eta_{2,n}}{Re}(\eta_{2,i}^2\frac{\partial^2 u_{3n}}{\partial z_2^2} + \eta_{2,ii}\frac{\partial u_{3n}}{\partial z_2}) =$$

$$\{\tau_{1,ni}x_{3i} + \tau_{2,ni}h_i - g_{3n} + E_n + \frac{1}{Re}[2\eta_{1,i}\eta_{2,i}\frac{\partial^2 u_{3n}}{\partial z_1 \partial z_2} + 2\eta_{2,i}\eta_{3,i}\frac{\partial^2 u_{3n}}{\partial z_2 \partial z_3}]\}\eta_{2,n} \quad (4.14)$$

On the LHS of the above equation, all terms were treated implicitly. The finite-difference representation of each term on the LHS of the above equation is described below.

$\frac{\partial p}{\partial z_j}$:

$$\frac{\partial p}{\partial z_1} = (p_{i+1} - p_{i-1})/2$$
$$\frac{\partial p}{\partial z_3} = (p_{k+1} - p_{k-1})/2$$
$$\frac{\partial p}{\partial z_2} = p_{jmax} - p_{jmax-1}$$

$\frac{\partial u_{3n}}{\partial z_2}$:

$$\frac{\partial u_{3n}}{\partial z_2} = u_{3njmax} - u_{3njmax-1}$$

$\frac{\partial^2 u_{3n}}{\partial z_2^2}$:

$$\frac{\partial^2 u_{3n}}{\partial z_2^2} = u_{3njmax} - 2u_{3njmax-1} + u_{3njmax-2}$$

All the above quantities fit into the 3-D CSIP 7-point molecule (see CSIP section in this chapter) except the quantity, $u_{3njmax-2}$, which appears in the representation of the second-order viscous term. This quantity was lagged to the RHS.

The above equation was not applied at the edge of the free surface. Instead the Lagrangian extrapolation formula, Eq. (4.7), was used in the z_2 (radial) direction to provide the pressure boundary equation at the wall of the container for all θ directions from the pressure data at interior points of the free surface.

4.6 The Artificial Compressibility Method for Incompressible Flows

The final governing equations, Eqs. (2.35) and (2.36) together with the boundary equations at the walls, Eqs. (3.1) and (3.2), and the boundary equations at the free surface, Eqs. (3.3) to (3.6), close the system of equations once the free surface position is updated by the kinematic equation, Eq. (3.7). The continuity equation, Eq. (2.35), serves as a compatibility condition for incompressible flows to ensure that the pressure and velocity solutions which satisfy Eq. (2.36) provide a divergence-free velocity field as well. A form of the artificial compressibility method (first proposed by Chorin [22]) was used in this study. This method gained popularity recently because several researchers, including Rogers and Kwak [19], Merkle and Athavale [20] and Pan and Chakravarthy [21], have shown that this procedure can be extended to

calculate unsteady incompressible flows by performing subiterations at each physical time step until a divergence-free solution is obtained for velocity. With the use of this method, a lengthy derivation (especially for the present liquid sloshing problem which involves several coordinate rotations and transformations) for the pressure Poisson equation was avoided. The four unknowns, u_{3i} and p, are obtained simultaneously by this procedure. This artificial compressibility method was adopted in this three-dimensional study and combined with the strongly implicit procedure which will be described in the next section.

The first step in doing this is to add an artificial time derivative of pressure, $\frac{\partial p}{\partial \tau^*}$, to the continuity equation. This artificial pressure term not only provides a linkage between the time variation of pressure and the divergence of the velocity, but also makes the coupled system nonsingular if central differences are used in the continuity equation. That is, if central differences are used for the spatial derivatives, the coupled system would be singular without the addition of the artificial time derivative. The final equations become:

$$\frac{\partial p}{\partial \tau^*} + \eta_{j,i}\frac{\partial u_{3i}}{\partial z_j} = 0 \tag{4.15}$$

and

$$\begin{aligned}\frac{\partial u_{3n}}{\partial \tau} + (\dot{z}_j + \eta_{j,i}u_{3i} + \eta_{j,i}f_{ik}x_{3k})\frac{\partial u_{3n}}{\partial z_j} - (f_{ni} + 2\lambda_{ni})u_{3i} \\ +\eta_{j,n}\frac{\partial p}{\partial z_j} - \frac{1}{Re}(\eta_{j,i}\eta_{k,i}\frac{\partial^2 u_{3n}}{\partial z_j \partial z_k} + \eta_{k,ii}\frac{\partial u_{3n}}{\partial z_k}) \\ = \tau_{1,ni}x_{3i} + \tau_{2,ni}h_i - g_{3n} + E_n\end{aligned} \tag{4.16}$$

where τ^* is a pseudotime. Note that this pseudotime is also added to the free surface continuity equation, Eq. (3.3).

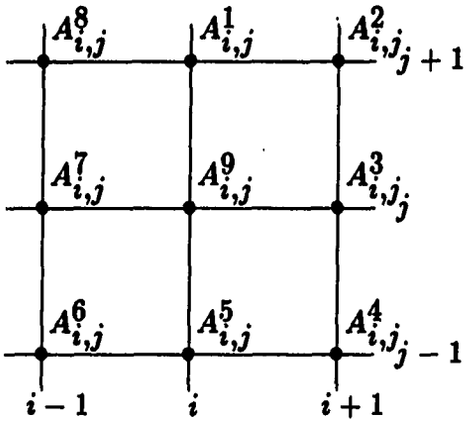

Figure 4.7: Two-dimensional computational molecule for $A^1_{i,j}$, $A^2_{i,j}$,..., $A^9_{i,j}$

It is important to add this artificial time term to the continuity equation after the generalized coordinate transformation is applied instead of before if the grid is moving in time. Pan and Chakravarthy [21] have pointed out that for a moving grid system, the divergence of the velocity would not be zero if this term was added before the generalized coordinate transformation even in steady state calculations.

4.7 Coupled Strongly Implicit Procedure

The coupled partial differential equations will become a coupled algebraic system of equations after the above finite-difference discretization scheme is applied to each derivative term of the governing equations. Since the derivative terms in the governing equations were treated in a fully implicit manner, the algebraic system of equations for the two and three-dimensional equations will take the following forms:

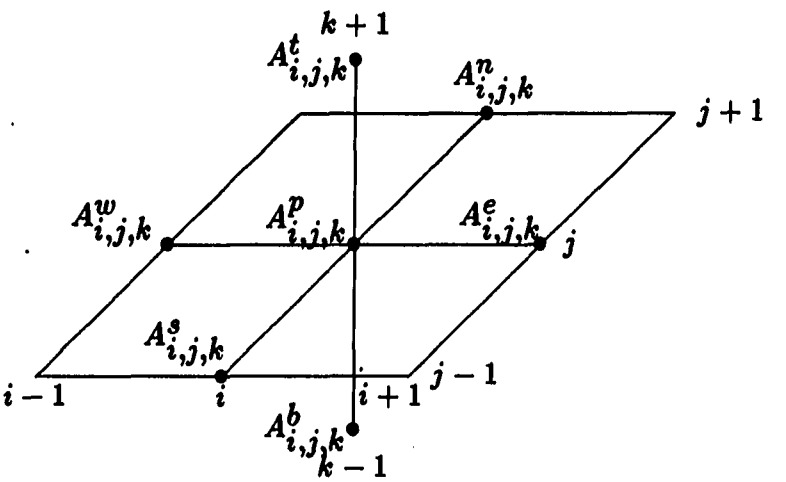

Figure 4.8: Three-dimensional computational molecule for $A^e_{i,j,k}$, $A^w_{i,j,k}$,..., $A^p_{i,j,k}$

For 2-D:

$$A^6_{i,j}\vec{q}_{i-1,j-1} + A^5_{i,j}\vec{q}_{i,j-1} + A^4_{i,j}\vec{q}_{i+1,j-1} + A^7_{i,j}\vec{q}_{i-1,j} + A^9_{i,j}\vec{q}_{i,j} + A^3_{i,j}\vec{q}_{i+1,j} + A^8_{i,j}\vec{q}_{i-1,j+1} + A^1_{i,j}\vec{q}_{i,j+1} + A^2_{i,j}\vec{q}_{i+1,j+1} = \vec{b}_{i,j} \quad (4.17)$$

For 3-D:

$$A^b_{i,j,k}\vec{q}_{i,j,k-1} + A^s_{i,j,k}\vec{q}_{i,j-1,k} + A^w_{i,j,k}\vec{q}_{i-1,j,k} + A^p_{i,j,k}\vec{q}_{i,j,k} + A^e_{i,j,k}\vec{q}_{i+1,j,k} + A^n_{i,j,k}\vec{q}_{i,j+1,k} + A^t_{i,j,k}\vec{q}_{i,j+1,k} = \vec{b}_{i,j,k} \quad (4.18)$$

where the coefficients A^1 to A^9 for two-dimensional equations and A^b to A^t for three-dimensional equations are 4×4 matrices and $\vec{q}$ is the vector of unknowns (dependent variables), $(u, v, p, T)^T$ for 2-D and $(u_{3i}, p)^T$ for 3-D, and $\vec{b}$ is the RHS vector. The difference molecule can be seen in Figs. 4.7 and 4.8 for two-dimensional and three-dimensional equations respectively. The *A's* are the coefficient matrices for the unknowns at the positions indicated in the figures. Equations (4.17) and (4.18)

can be expressed in the following matrix form:

$$[A]\vec{q} = \vec{b} \tag{4.19}$$

where

$$[A] = \begin{bmatrix} A^9_{1,1} & A^3_{1,1} & & A^1_{1,1} & A^2_{1,1} & & & & \\ A^6_{i,j} & A^5_{i,j} & A^4_{i,j} & A^7_{i,j} & A^9_{i,j} & A^3_{i,j} & & A^8_{i,j} & A^1_{i,j} & A^2_{i,j} \\ & & & & A^6_{im,jm} & A^5_{im,jm} & & A^7_{im,jm} & A^9_{im,jm} & \end{bmatrix}$$

is for the two-dimensional equations and

$$[A] = \begin{bmatrix} A^{p\,a}_{\alpha} & A^{e}_{\alpha} & & A^{n}_{\alpha} & & A^{t}_{\alpha} & \\ A^{b\,b}_{\beta} & A^{s}_{\beta} & A^{w}_{\beta} & A^{p}_{\beta} & A^{e}_{\beta} & A^{n}_{\beta} & A^{t}_{\beta} \\ & & A^{b\,c}_{\gamma} & A^{s}_{\gamma} & A^{w}_{\gamma} & A^{p}_{\gamma} & \end{bmatrix}$$

[a] subscript α represents point $(1, 1, 1)$
[b] subscript β represents point (i, j, k)
[c] subscript γ represents point (im, jm, km)

is for the three-dimensional equations.

Detailed discussions of the this strongly implicit procedure for two and three-dimensional equations can be found in several sources [29], [45], [30], [44], [43] and therefore only the basic concept will be described in the following paragraphs. Interested readers should refer to the literature cited above to obtain detailed formula.

A general iterative formula for Eq. (4.19) may be obtained by adding an auxiliary matrix $[P]$ to each side of Eq. (4.19) and adding iteration numbers to $\vec{q}$ as:

$$[A+P]\vec{q}^{n+1,k+1} = [P]\vec{q}^{n+1,k} + \vec{b} \tag{4.20}$$

where n is the time level and k is the iteration level, and $[P]$ is so chosen that the decomposition of $[A+P]$ can be obtained conveniently. In general, the convergence rate becomes faster as $[A+P]$ becomes closer to $[A]$, or in other words, as the scheme becomes more "implicit". In this regard $[P] = 0$ gives the fastest convergence. In effect the solution is obtained by "one iteration", $\vec{q} = [A]^{-1}\vec{b}$, although the iterative solutions are necessary when such a direct inversion is difficult or costly.

In the strongly implicit method, $[P]$ is chosen that $[A+P]$ can be decomposed as:

$$[A+P] = [L][U] \tag{4.21}$$

where $[L]$ and $[U]$ are, respectively, lower and upper triangular matrices, each of which has only five nonzero diagonals for the two-dimensional 9-point formula and four nonzero diagonals for the three-dimensional 7-point formula in each row. Inversion of a matrix in the form of $[L][U]$ is very easy. If $[P]$ is a minor correction to $[A]$, then the iterative scheme represented by Eq. (4.20) may be regarded as *strongly implicit*. The above $[L]$ and $[U]$ matrices were constructed to have nonzero diagonals

at the same positions as the original matrix $[A]$, so that no additional storage was needed. However, there is a numerical error prior to convergence associated with this decomposition because the matrix resulting from the product of $[L]$ and $[U]$ is not identical to the $[A]$ matrix and the error is due to the $[P]$ matrix. The issue now is how to minimize the effect of the auxiliary matrix $[P]$ in order to hasten convergence. Usually the effect of the $[P]$ matrix is small and if nothing is done to reduce the effect of this auxiliary matrix, the method is called incomplete L-U (ILU) decomposition. The errors vanish, of course, if the iterative procedure defined by Eq. (4.20) converges. However as mentioned before, the scheme may converge faster if the effect of the $[P]$ matrix is minimized.

Stone [29] proposed that a partial cancellation parameter be introduced to reduce the influence of this extra $[P]$ matrix. The original Stone's SIP contains only a 5-point formula and it was extended to a 9-point formula by Schneider and Zedan [30] for two-dimensional scalar equations using the same idea. The new 9-point formula was named the modified strongly implicit procedure (MSIP). The MSIP formula, which was found to be less sensitive to the partial cancellation parameter and also showed better convergence properties than the SIP formula, was used for the two-dimensional equations in the present study. Since a coupled system of equations was solved in this study, the scalar MSIP formula has been modified to solve coupled equations. The extension to a coupled formula is very straightforward (see Appendix F) and therefore only the scalar version is demonstrated here. An explanation of the extension to a coupled system of equations can be also found in Zedan and Schneider [44], where the 5-point SIP formula was used. In the MSIP method, the $[L]$ and $[U]$

matrices are chosen as:

$$[L] = \begin{bmatrix} a_{i,j} & b_{i,j} & c_{i,j} & d_{i,j} & e_{i,j} & & \\ & a_{i,j} & b_{i,j} & c_{i,j} & d_{i,j} & e_{i,j} & \\ & & a_{i,j} & b_{i,j} & c_{i,j} & d_{i,j} & e_{i,j} \end{bmatrix}$$

$$[U] = \begin{bmatrix} 1 & f_{i,j} & g_{i,j} & h_{i,j} & s_{i,j} & & \\ & 1 & f_{i,j} & g_{i,j} & h_{i,j} & s_{i,j} & \\ & & 1 & f_{i,j} & g_{i,j} & h_{i,j} & s_{i,j} \end{bmatrix}$$

The formulas used to calculate the elements in $[L]$ and $[U]$ from the original matrix $[A]$ are listed in Appendix F. After $[L]$ and $[U]$ are obtained, the following procedure is used to obtain the unknown vector $\vec{q}$.

Letting

$$\vec{\delta}^{n+1,k+1} = \vec{q}^{n+1,k+1} - \vec{q}^{n+1,k} \tag{4.22}$$

and a residual vector

$$\vec{R}^{n+1,k} = \vec{b} - [A]\vec{q}^{n+1,k} \tag{4.23}$$

Eq. (4.20) becomes

$$[A+P]\vec{\delta}^{n+1,k+1} = \vec{R}^{n+1,k} \tag{4.24}$$

Replacing $[A+P]$ by the $[L][U]$ product gives

$$[L][U]\vec{\delta}^{n+1,k+1} = \vec{R}^{n+1,k}$$

Defining an provisional vector $\vec{W}$ by

$$\vec{W}^{n+1,k+1} = [U]\vec{\delta}^{n+1,k+1} \tag{4.25}$$

the solution procedure can be written in two steps:

Step 1:

$$[L]\vec{W}^{n+1,k+1} = \vec{R}^{n+1,k} \tag{4.26}$$

Step 2:

$$[U]\vec{\delta}^{n+1,k+1} = \vec{W}^{n+1,k+1} \tag{4.27}$$

The process represented by Eqs. (4.26) and (4.27) consists of a forward substitution to determine $\vec{W}^{n+1,k+1}$ followed by a backward substitution to obtain $\vec{\delta}^{n+1,k+1}$. The coefficient matrix $[A]$, and so the $[L]$ and $[U]$ matrices, have to be updated at each iteration if linearization errors are to be removed.

For three-dimensional flows, the above procedure is applied to 7-point formula in an exactly the same way. The $[L]$ and $[U]$ matrices for three-dimensional equations

are listed as follows:

$$[L] = \begin{bmatrix} & & & & \\ a_{i,j,k} & d_{i,j,k} & f_{i,j,k} & g_{i,j,k} & \\ & & & & \end{bmatrix}$$

$$[U] = \begin{bmatrix} & & & & \\ & & & & \\ & & 1 & h_{i,j,k} & r_{i,j,k} & v_{i,j,k} \\ & & & & & \end{bmatrix}$$

The relationship between the elements in $[L]$ and $[U]$ and those in the original matrix $[A]$ for three-dimensional equations is also given in Appendix F. Interested readers can also refer to the paper by Weinstein, Stone and Kwan [45].

The two-dimensional 9-point MSIP method requires nine arrays of dimension $(im, jm, 4, 4)$ in the coefficient matrix for a coupled system or five arrays of the same

dimension for the reduced 5-point formula. In three dimensions, the 7-point CSIP method requires seven large arrays of dimension $(im, jm, km, 4, 4)$ in the coefficient matrix. It should be noted that Zedan and Schneider [46] also derived a three-dimensional 19-point formula for the MSIP scheme for a scalar equation. This 19-point formula was not used in this study simply because it requires significantly more computer storage (about 2.3 times) for a coupled system, than Stone's original three-dimensional 7-point formulation.

4.8 Convergence Acceleration Techniques

As for most central difference schemes, the time term serves to enhance the diagonal dominance. This time term is even more important when the continuity equation is coupled with the momentum and energy equations. When central differences are applied to the spatial derivative terms in the continuity equation, the time term must be retained to avoid a singularity in the matrix system. Unlike the momentum and energy equations which possess nonzero diagonal terms from the diffusion and conduction terms, the time term in the continuity equation bears all the burden of providing the diagonal dominance in this equation. Although the present method solves equations in a coupled manner, and the resulting coefficient matrix is in a block form, the diagonal dominance requirement for the continuity equation has been found to provide a good guideline to assure convergence of the coupled equations. Golub and Van Loan [54] provide the definition of diagonal dominance for a block system, but it was found impractical to use in the present work.

Consistent with the above observations, it was found that if the steady state solution was the only concern, dual-time steps could be used to accelerate the convergence

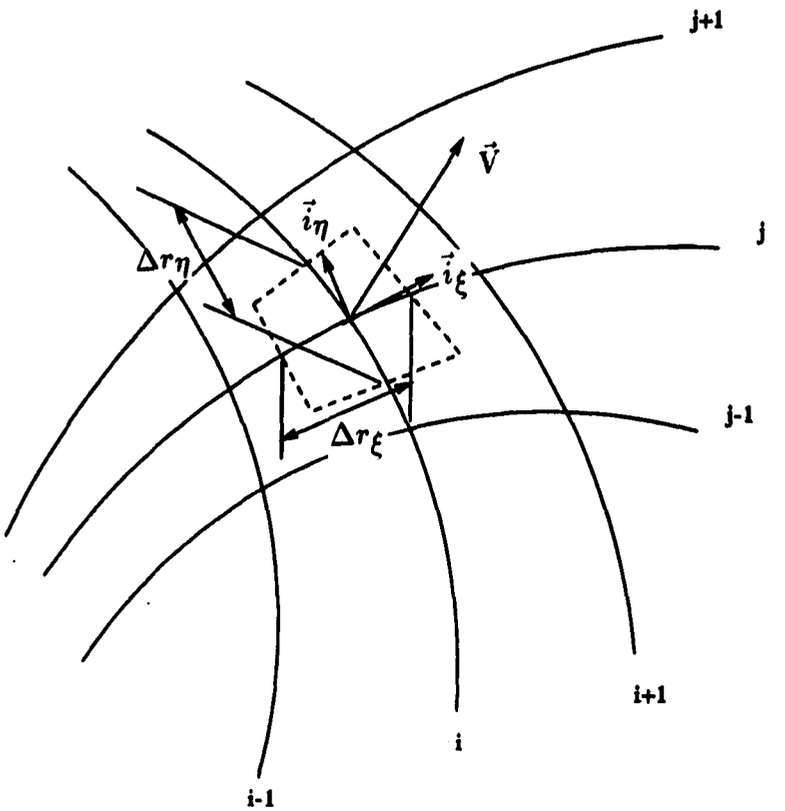

Figure 4.9: Notation for the local time step computation for two-dimensional flows

rate for low Mach number flows in the steady two-dimensional compressible calculations when an isothermal condition could be assumed. This dual-time technique applies a much smaller time step for the continuity equation than for the momentum equations. For the current formulation, the time step for the continuity equation is about the order of M_∞^2 for low Mach number flows. This technique assures that the rapidly propagating pressure signal in low Mach number flows is resolved by the smaller time step used in the continuity equation which can be thought as an equation for pressure.

In addition to the above special treatment for the time step in the continuity

equation, a local time step in the momentum and energy equations can be used to further accelerate the convergence for steady state flow calculations. This local time step employs a different time step for each grid point depending on the local speed of propagation for convective signals. The local time step was determined using the following formula:

$$\Delta t_\xi = \frac{\Delta r_\xi}{\vec{V} \cdot \vec{i}_\xi}$$

$$\Delta t_\eta = \frac{\Delta r_\eta}{\vec{V} \cdot \vec{i}_\eta}$$

where $\vec{i}_\xi$ and $\vec{i}_\eta$ are the *local* unit vectors along the ξ and η directions, respectively, Δr_ξ and Δr_η are the cell lengths in the ξ and η direction, respectively, and $\vec{V}$ is the *local* velocity vector (see Fig. 4.9). The final Δt is chosen by:

$$\Delta t = \sigma_1 DMIN(\Delta t_\xi, \Delta t_\eta) \tag{4.28}$$

where σ_1 is a parameter to further control this local time step and DMIN chooses the minimum value from its two arguments. The above formula was applied for each grid point. This formula was derived based the assumption that a local time step cannot exceed the time required for a fluid particle to travel across each cell in the unsteady calculations. This idea was adapted here for steady state calculations to estimate the maximum local time step. This choice of time step seems to be somewhat arbitrary. However, it was found that the procedure can accelerate convergence for steady state computations by a factor of about 2 to 3. The choice of σ_1 needs to be determined by numerical experiments. The rule adopted in the present study was to choose σ_1 as large as possible without causing the solution to diverge. The choice of σ_1 depends on problems and flow types as well. For low Reynolds number problems, σ_1 can be as

high as 10^3 and about the order of one, $O(1)$, for high Reynolds number calculations. This formula is simple and easy to use in the program.

Since the time dependent aspects of the three-dimensional liquid sloshing flow calculations were of interest, the steady state convergence acceleration technique described above could not be applied. However, in the artificial compressibility method, the time term in the continuity equation is artificial (in pseudotime) even for time accurate calculations, and it was found that convergence was enhanced by using a *local* pseudotime. This local pseudotime was determined based on the following criterion:

$$(\Delta\tau^*)_{i,j,k} \simeq \frac{\sigma_2}{\sum|\lambda_{i,j,k}|} \tag{4.29}$$

where $\lambda_{i,j,k}$ are the off-diagonal coefficient terms in the continuity equation and the summation is over the six neighboring points at each i,j,k location. The $\Delta\tau^*$ is a local value and varies in space. The σ_2 is a constant to further control the time step. The choice of σ_2 is problem-dependent. Usually a value of the order of one, $O(1)$, gave satisfactory results.

4.9 Convergence Criterion and Solution Procedure

For two-dimensional compressible calculations, the convergence criterion was based on the norm of all variables in a coupled sense. This criterion is as follows:

$$\left(\frac{\sum_{i,j=1}^{im,jm} \sum_{n=1}^{n=4} \left| \frac{q_n^{k+1} - q_n^k}{q_{n,rms}^{k+1}} \right|^2}{4 \times im \times jm} \right)^{0.5} \leq \epsilon, \tag{4.30}$$

where k is the iteration level, n the variable index, im the number of grid points in the x direction, jm the number of grid points in the y direction, q_n a component of

the unknown vector $\vec{q}$, and $q_{n,rms}$ the root mean square value of q_n. The criterion ϵ was generally set equal to 1.0×10^{-4}. However, for three-dimensional incompressible calculations, the convergence at each physical time step was based on the divergence of the velocity field. This criterion was as follows:

$$\nabla \cdot \vec{V} = \eta_{j,i} \frac{\partial u_{3i}}{\partial z_j} \leq 5 \times 10^{-4} \tag{4.31}$$

The solution procedure for two and three dimensional flows can be summarized as follows:

Two-dimensional flow calculations:

1. Set initial conditions (or guess for steady state computation).
2. Generate grid.
3. Construct the coefficient matrix $[A]$ and the right-hand-side vector $\vec{b}$.
4. Call the CSIP solver to update solution (u, v, p, T); go back to step 3 and subiterate until convergence at each time step for unsteady calculations.
5. Move to the next time step and go to step 3 until steady state solutions are reached or the specified time is reached. No subiteration is required in step 4 if only steady state solution is desired.

Three-dimensional liquid sloshing flow calculations:

1. Set initial conditions.
2. Update the free surface position at each time step by the kinematic equation based on the flow solution at the previous time step.

3. Generate the grid using the new free surface position.

4. Construct the coefficient matrix $[A]$ and the right-hand-side vector $\vec{b}$.

5. Call the CSIP solver to update solution (u_{3i}, p); go back to step 4 and subiterate (until convergence) to create a divergence-free field at each time step.

6. Go back to step 2 and move to the next time step.

5. RESULTS AND DISCUSSION

The numerical procedure described in the previous chapter has been applied to both two-dimensional compressible and three-dimensional incompressible flows. Of particular interest in the compressible flow study is the performance of the present algorithm (pressure based scheme) over a wide range of Mach numbers. Also of interest is the low Mach number regime, where convergence difficulties are often observed for other density based compressible flow schemes. The three-dimensional scheme is applied to study the complex time-dependent motion of liquid in a partially filled spherical container. This flow is especially challenging due to the three-dimensional motion of the free surface. Results obtained for these two types of flows are described in the next two sections.

5.1 Two-Dimensional Compressible Results

In order to evaluate the performance of the present numerical algorithm on two-dimensional compressible flows, especially for a wide range of Mach numbers, several types of geometries and flow speeds were considered. They are summarized in Table 5.1. It is believed that these cases are diverse and challenging enough to demonstrate the capabilities of the present algorithm. The results for these five test cases follow.

Table 5.1: Summary of test cases for two-dimensional compressible flows

Case	Description
1.	Developing flow in a channel. (Inlet Mach number = 0.05; inlet Reynolds number = 0.5, 10, 75, 500 and 7500)
2.	Driven cavity flow. (Mach number = 10^{-4} to 0.2; Reynolds number = 100, 1000 and 3200)
3.	Steady flow over a circular cylinder. (Inlet Mach number = 0.05; inlet Reynolds number = 40)
4.	Unsteady vortex shedding flow over a circular cylinder. (Inlet Mach number = 0.2; inlet Reynolds number = 100)
5.	Shock-boundary layer interaction problem. (Inlet Mach number = 2.0; inlet Reynolds number = 0.296×10^{6})

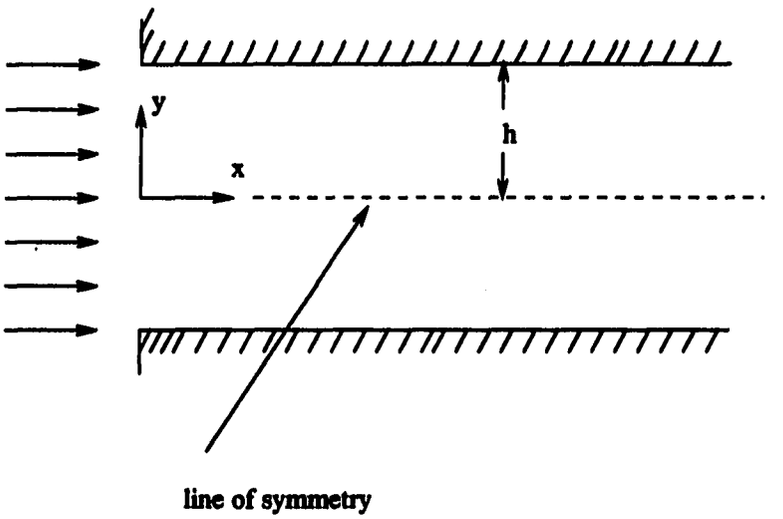

Figure 5.1: Geometry of a constant area, two-dimensional channel inlet

5.1.1 Subsonic steady state flows

5.1.1.1 Developing flow in a channel The first test case is flow in a constant area, two-dimensional channel inlet with and without heat transfer. A uniform flow enters the channel and the velocity and temperature fields develop along the channel simultaneously. It is well known that an incompressible flow will eventually become fully developed with a parabolic velocity distribution. The centerline velocity will reach a value 1.5 times the inlet velocity. However, for an isothermal compressible flow, the velocity will continue to increase and eventually the flow will become choked [55]. This is due to the fact that the density of the fluid will become

smaller and smaller as the pressure continues to drop along the channel. Therefore, there will be no fully developed velocity profile for isothermal compressible flows in this channel configuration. The geometry of this test case can be seen in Fig. 5.1.

Due to the symmetric nature of this channel flow, the solution was only computed in the upper half of the channel. Four cases with Reynolds numbers of 0.5, 10, 75 and 7500 and a Mach number of 0.05 were studied. The Reynolds number is based on the inlet velocity, bulk density and half width of the channel. Grids of 21×11, 21×11, 31×11 and 41×11 points and nondimensional channel lengths of 2, 4, 30 and 3000 were used for Reynolds numbers of 0.5, 10, 75 and 7500, respectively. The length of the channel for each Reynolds number was chosen to provide a reasonable distance for the flow to develop. The grid points were clustered near the inlet and the upper wall. The centerline velocity distribution along the flow development region is shown in Fig. 5.2. The present results were basically compared with calculations obtained by others for incompressible flows. Only the results presented by TenPas and Pletcher [26] were obtained with a compressible flow formulation. Due to the use of the compressible equations, the velocity profile will never become independent of distance along the channel. However, in order to compare with the incompressible results in the literature, the converged velocity solutions from the present calculations were adjusted. Since the finite-difference scheme maintained a constant mass flow rate in the channel at steady state, the velocities were decreased appropriately to compensate for the density decreases when comparing with incompressible results. This correction was made by TenPas and Pletcher as well for their compressible formulation. The agreement between the present results and those obtained by TenPas and Pletcher [26], Morihara and Cheng [56], McDonald, Denny and Mills [57] and Bodoia and

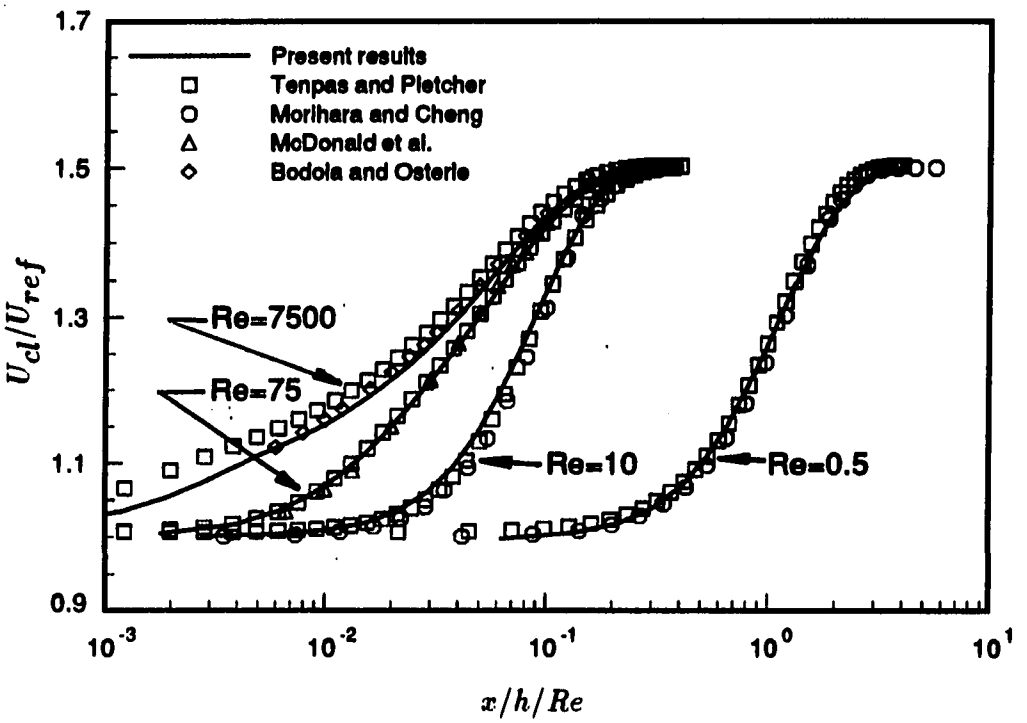

Figure 5.2: Predicted centerline velocity distribution for developing flow in a two-dimensional channel inlet

Osterle [58] is good. In Fig. 5.2, the results obtained by Bodoia and Osterle are from solutions of the boundary layer equations. It is clear that the boundary-layer assumption is no longer valid as the Reynolds number becomes smaller and smaller for the channel inlet, and the full Navier-Stokes equations must be solved in order to obtain the correct flow details in the flow development region. The convergence history of these four cases is shown in Fig. 5.3. It should be noted that for steady state calculations, subiterations were not used at each time step.

Heat transfer results are also shown in Fig. 5.4. The Reynolds number in this case is 500 based on the hydraulic diameter D and the Prandtl number is 0.72. A temperature ratio of T_w/T_i=1.2 was maintained along the wall of the channel. A 41×21 grid was used. The agreement of averaged Nusselt number with the results by Hwang and Fan [59] is good. The averaged Nusselt number is defined as:

$$\bar{N}u = h_m D/k \tag{5.1}$$

where D is the hydraulic diameter, and k is the thermal conductivity at the fluid inlet temperature and h_m is the average heat transfer coefficient. The average heat transfer coefficient, h_m, is defined as:

$$h_m = \frac{Q}{A\Delta T} \tag{5.2}$$

where the temperature difference, ΔT, is taken as the log-mean temperature difference

$$\Delta T = \frac{(T_w - T_i) - (T_w - T_{b,x})}{ln[(T_w - T_i)/(T_w - T_{b,x})]} \tag{5.3}$$

where $T_{b,x}$ is the bulk temperature at each x station. The total heat flux Q from the entry to x is:

$$Q = 2\int_0^x k(\frac{\partial T}{\partial y})_{wall} dx \tag{5.4}$$

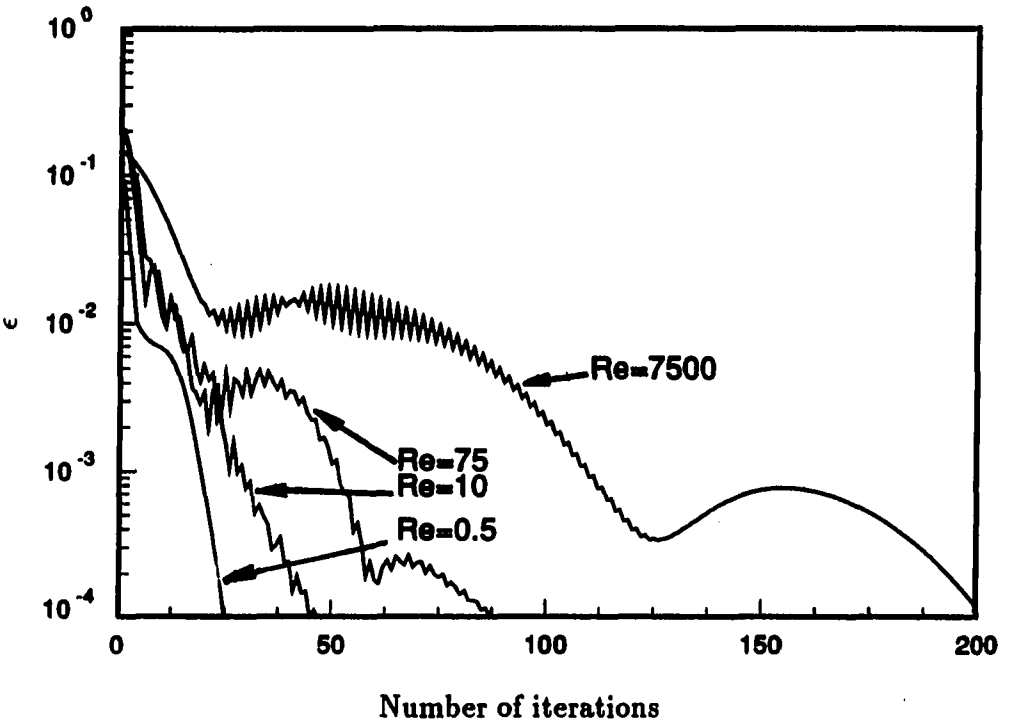

Figure 5.3: Convergence history for developing flow in a two-dimensional channel inlet

5.1.1.2 Driven cavity flow The two-dimensional driven cavity problem has been studied extensively by many investigators and has frequently served as a benchmark test case for incompressible Navier-Stokes calculations. The configuration for this flow can be seen in Fig. 5.5. The fluid initially is motionless inside the square cavity. Suddenly, the top lid is subject to a constant velocity and the fluid particles start to move due to the fluid viscosity. The flow pattern becomes very complex and can only be resolved computationally by solving the full Navier-Stokes equations. The flow pattern generally exhibits a very strong main vortex near the center of the cavity, and, depending on the magnitude of the Reynolds number, several weak eddies at the corners of the cavity. A very detailed analysis for this problem was presented by Ghia, Ghia and Shin [60] where a very fine grid (257×257) was used to compute the flow for Reynolds numbers ranging from 100 to 10,000. Their results, obtained with a coupled strongly implicit multigrid (CSI-MG) method, are usually considered as benchmark solutions for the cavity flow. Most investigators studying this flow reported velocity solutions only [60], [61], [62]. Only a few included solutions for pressure and heat transfer [63], [64], [65]. For an incompressible flow, it is possible to obtain the pressure from the solution for velocity by solving the pressure Poisson equation. However, considerable computational effort is required to solve this elliptic equation with Neumann type of boundary conditions. It is the present author's opinion that pressure is a very important quantity in practical applications, and for some types of flow it provides the dominant contribution to the aerodynamic drag force. Therefore, it should always be reliably calculated instead of ignored.

Results were obtained for Reynolds numbers of 100, 1000 and 3200 under an isothermal condition and a Mach number of 0.05. The temperature was assumed

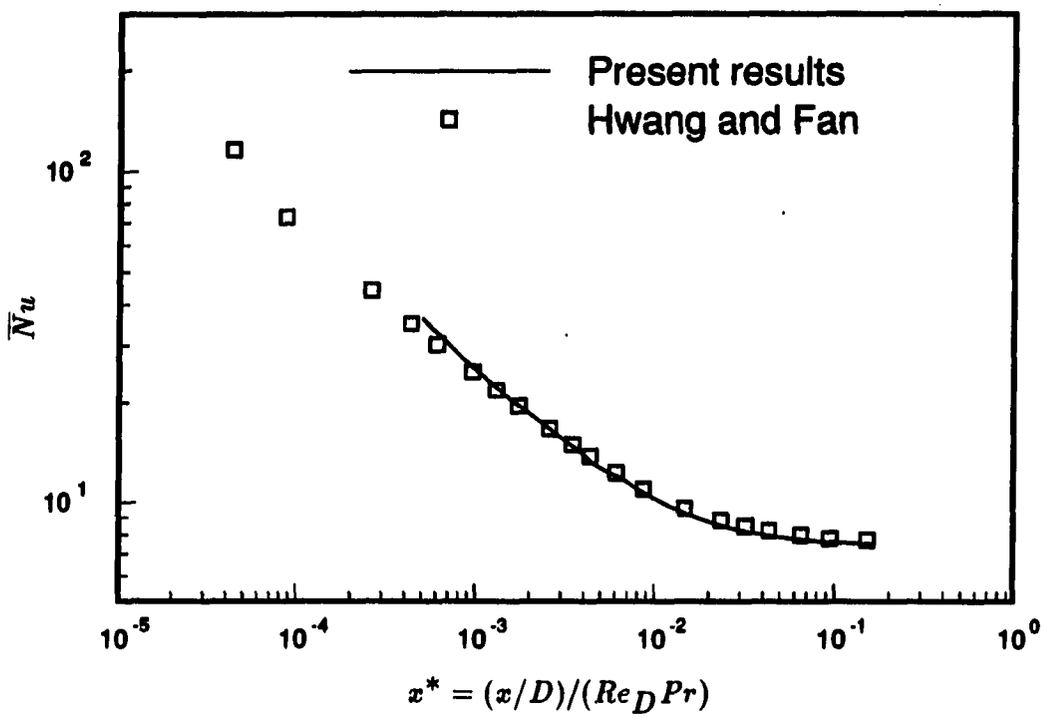

Figure 5.4: Predicted average Nusselt number for developing flow in a two-dimensional channel inlet, Re=500, Pr=0.72, $\frac{T_w}{T_i} = 1.2$

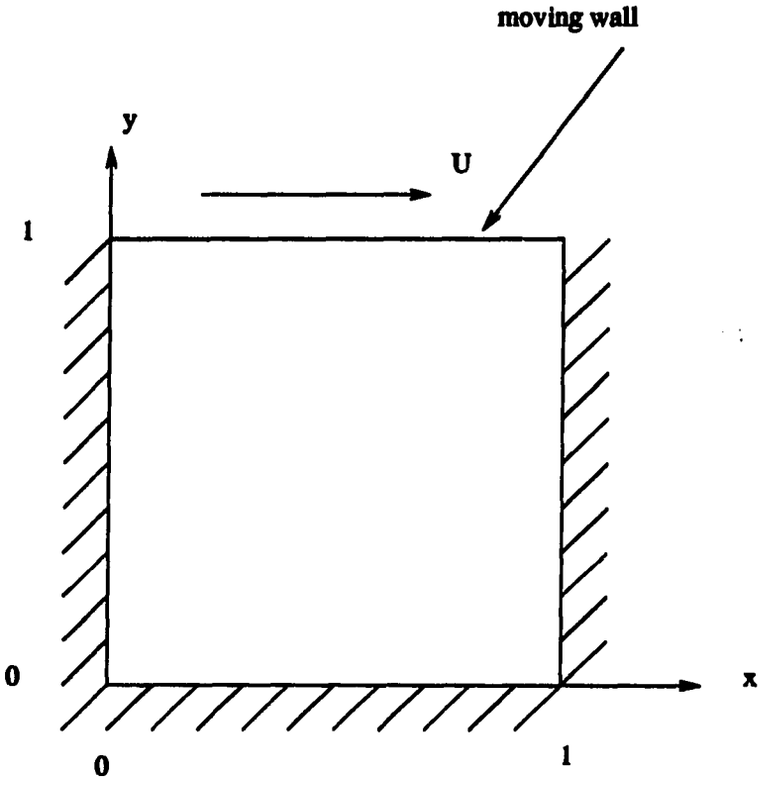

Figure 5.5: Geometry of the driven cavity flow

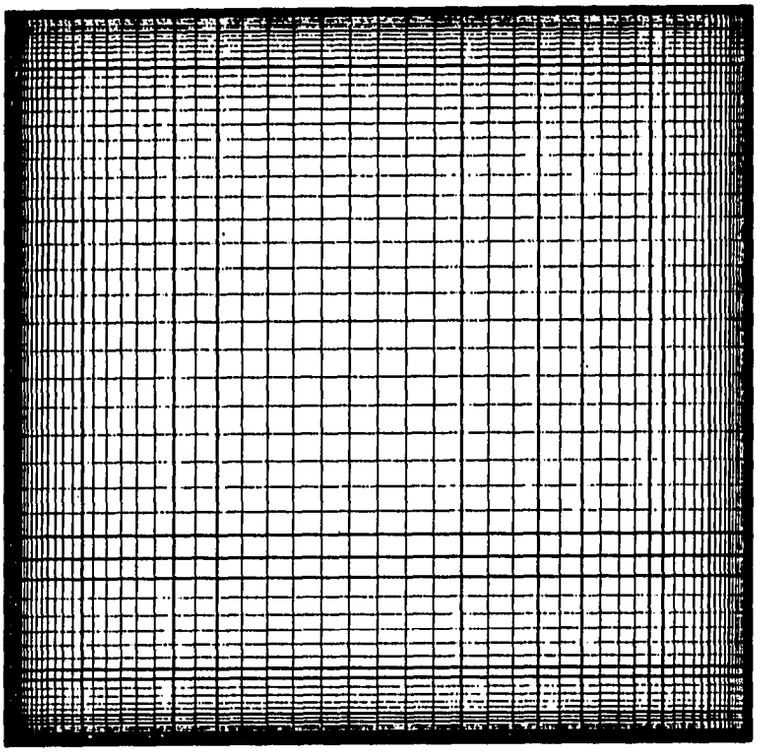

Figure 5.6: 71×71 grid layout for Re=3200 calculation

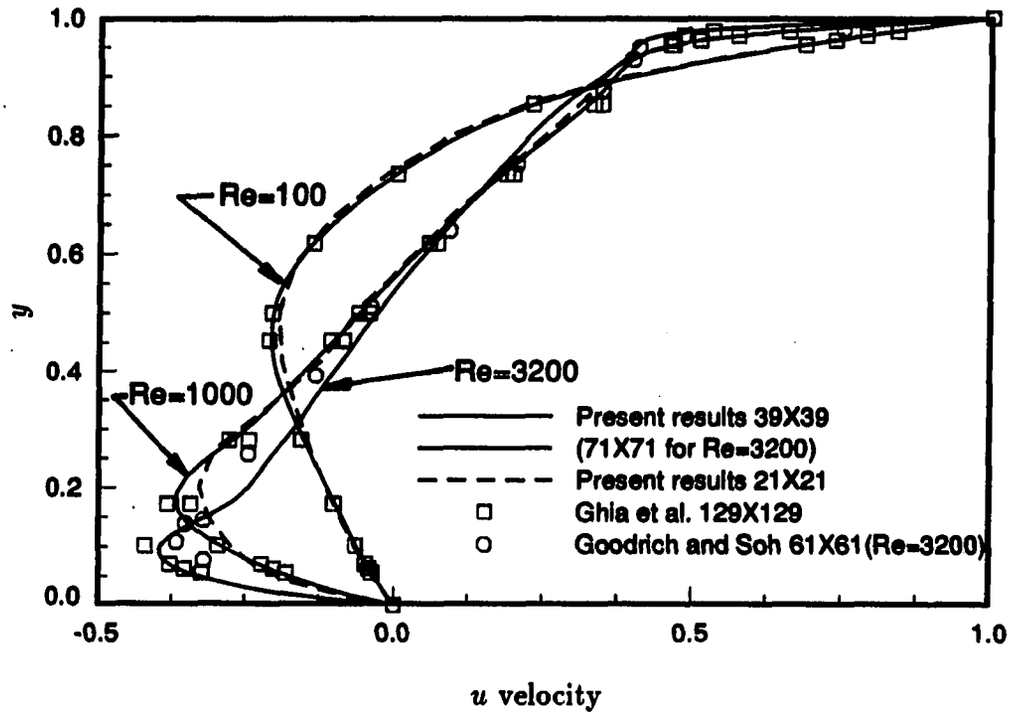

Figure 5.7: Predicted u velocity component along the vertical centerline of the two-dimensional driven cavity, for Re=100, 1000 and 3200

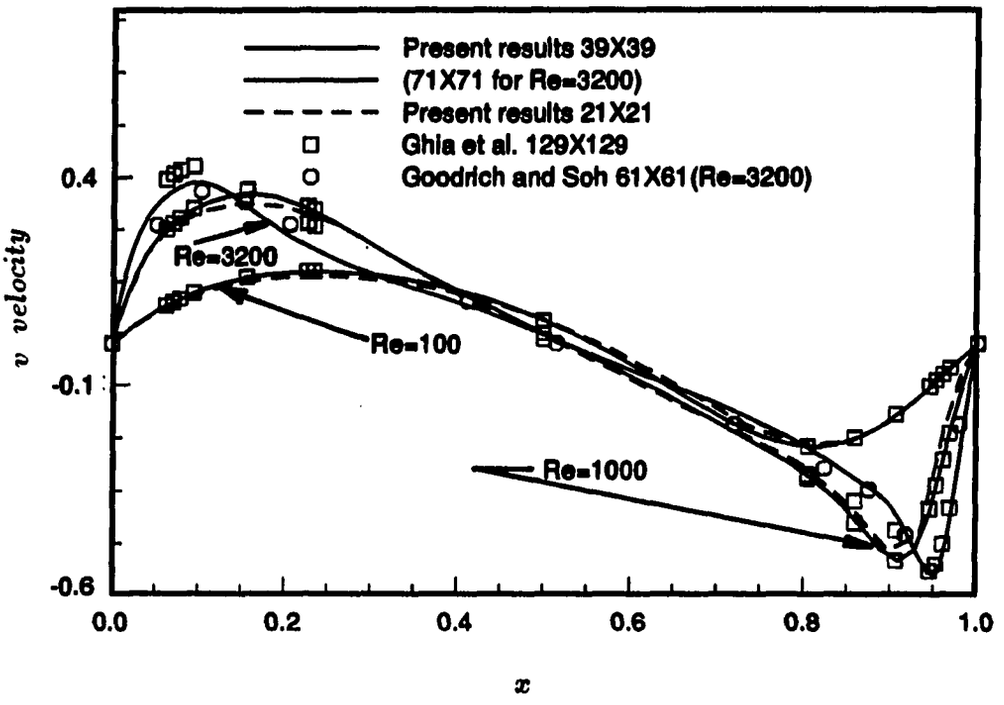

Figure 5.8: Predicted v velocity component along the horizontal centerline of the two-dimensional driven cavity, for Re=100, 1000 and 3200

to be uniform and constant because (1) the temperature variations would be very small at a Mach number of 0.05 and less if an isothermal wall boundary condition was assumed and (2) it would be more convenient to compare with the results in the literature where an isothermal flow condition was usually assumed. Of course, if the temperature distribution is of interest, the energy equation must be included as it was for the heat transfer cases to be discussed later. The grid lines were clustered near the walls using Eq. (4.4) in both the x and y directions. The 71×71 grid used for the Re=3200 case is shown in Fig. 5.6. The u velocity component along the vertical centerline is shown in Fig. 5.7 and the v velocity component along the horizontal centerline is shown in Fig. 5.8 for these three Reynolds numbers. The agreement with the results by Ghia, Ghia and Shin [60] and Goodrich and Soh [62] is excellent for Re=100 and 1000 and is good for Re=3200. The effects of grid refinement are also shown in these figures. Figure 5.9 compares the pressure distribution along the stationary wall obtained by the present method with those obtained by Ghia, Hankey and Hodge [66]. The number in the x coordinate of Fig. 5.9 represents the four corner points of the cavity as indicated in the insert. The streamline pattern, pressure contours, and velocity vectors for Re=3200 are shown in Fig. 5.10. It should be noted that for Reynolds number lower than 1000, the flow patterns are quite similar except that the strength of the eddies at the two corners of the bottom wall becomes stronger and stronger and the center of the main circulating region moves closer to the geometric center of the cavity. However, for Reynolds number higher than about 2000, a third eddy gradually appears near the left upper corner and increases in strength as the Reynolds number becomes higher and higher. This third eddy can be easily seen in Fig. 5.10.

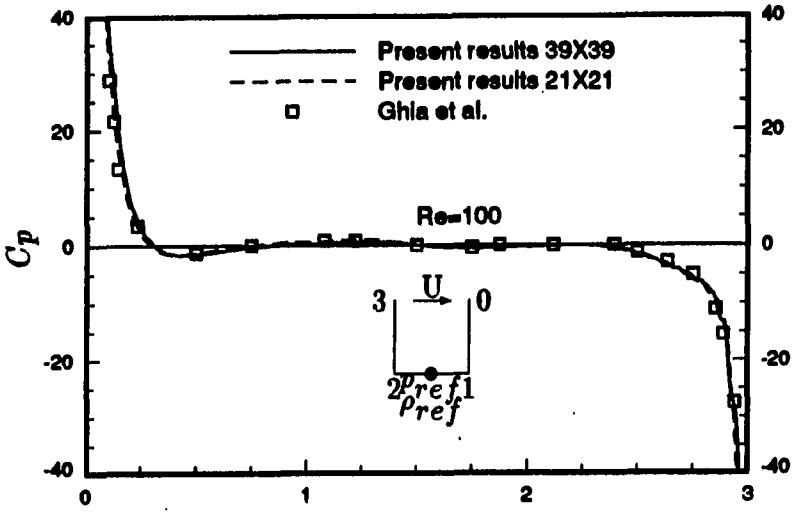

Distance along the perimeter of the stationary wall

(a)

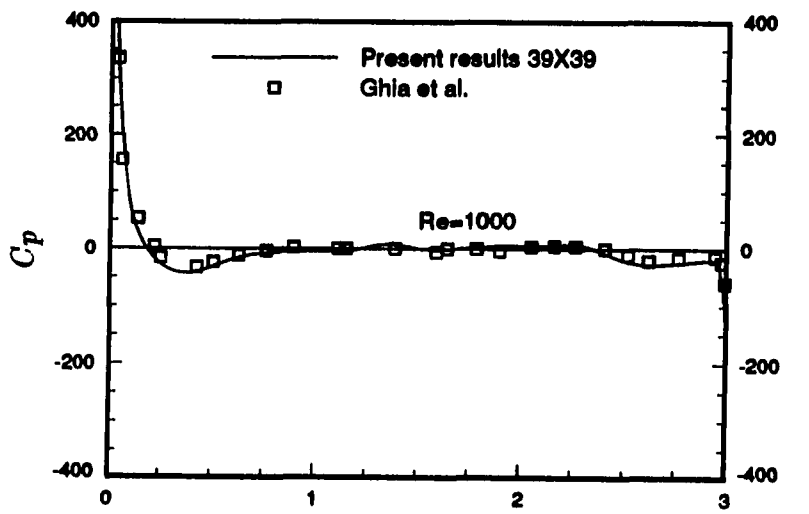

Distance along the perimeter of the stationary wall

(b)

Figure 5.9: Predicted pressure coefficient, C_p, along the stationary walls of the two-dimensional driven cavity, (a) Re=100, (b) Re=1000 ($C_p = Re \times (\tilde{p} - \tilde{p}_{ref})/\tilde{\rho}_{ref}U^2$)

For the grid points used (indicated in the figures), the convergence rate for Re=100 and 1000 compares very favorably with that reported by Mansour and Hamed [63] where a coupled scheme in primitive variables was used for the incompressible Navier-Stokes equations. Usually less than 200 iterations were sufficient to reduce the residual to the desired level. For the Re=3200 case, slow convergence for a 71×71 grids was encountered (more than 2000). A similar difficulty at this Reynolds number was also reported by Napolitano and Walters [61]. It is suspected that the slow convergence at this Reynolds number is due to the strong transient nature of the flow where several significant secondary flows appear and interact with the main circulating vortex. Goodrich et al. [67] has found the flow to be unsteady at $Re \simeq$ 5000.

Heat transfer phenomena were also studied for Reynolds numbers of 100 and 1000 and a Mach number of 0.05. Most of the heat transfer studies on the cavity configuration found in the literature were devoted to natural convection [68] where the four walls of the cavity were kept stationary, and the flow was induced by the buoyancy force which was created by a temperature difference between one wall and the others. Very few results can be found in the literature for the driven cavity configuration [65], [69].

The local Nusselt number along the top moving wall (T_m) which is hotter than the stationary walls (T_s) for Re=100 and 1000 with Pr=1.0 is shown in Fig. 5.11. The temperature ratio was T_s/T_m=0.9 (or T_m/T_s=1.11). The local Nusselt number in Fig. 5.11 is defined as:

$$Nu = \frac{hL}{k} \tag{5.5}$$

where L is the length of the cavity and k is the thermal conductivity at the tempera-

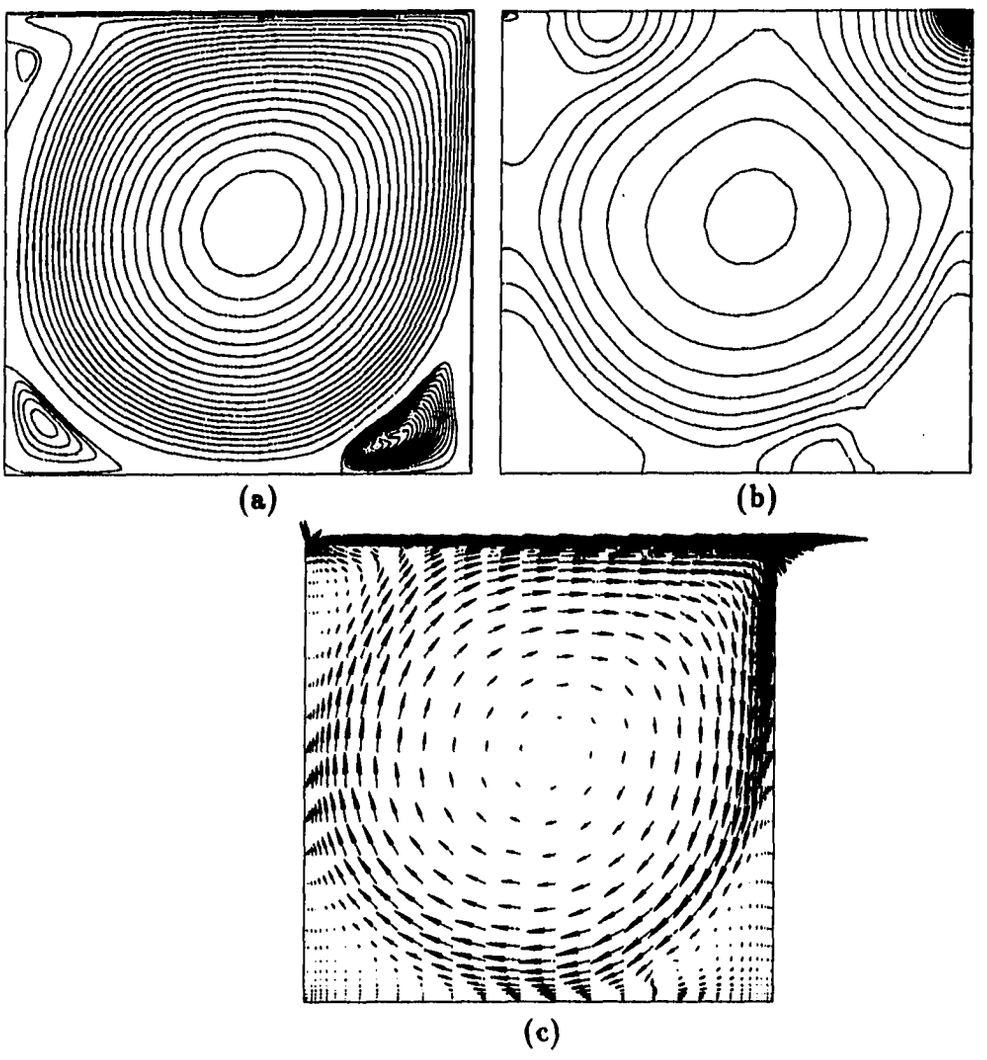

Figure 5.10: Results for the two-dimensional driven cavity flow, Re=3200, (a) streamlines, (b) pressure contours, (c) velocity vectors

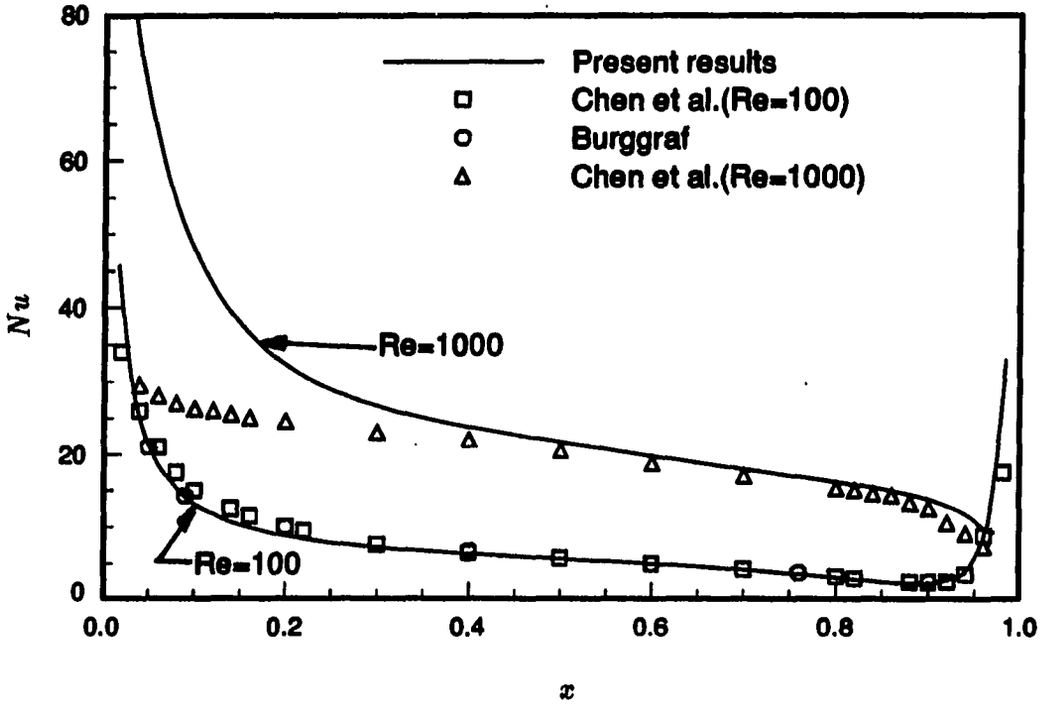

Figure 5.11: Local Nusselt number at the top moving wall of the two-dimensional driven cavity

ture of the hotter moving wall and h is the heat transfer coefficient (based on the $\Delta T = T_m - T_s$). The results for Re=100 were compared with those obtained by Chen et al. [65] (using a 41×41 uniform grid) and Burgraff [69] (using a 21×21 uniform grid). The good agreement is obvious. For this Reynolds number, a nonuniform 21×21 grid was used and 140 iterations were required to obtain the converged solution. The results for Re=1000, however, don't agree well with those of Chen et al. [65] (using a 41×41 uniform grid) near the left corner of the top wall. Further research is needed to resolve this discrepancy. For the Re=1000 calculation, a nonuniform 39×39 grid was used and more than 500 iterations were required to obtain the converged solution.

In order to study the effect of Mach number, the driven cavity case for Re=100 with a 21×21 grid was computed with Mach numbers ranging from 10^{-4} to 0.2 and an isothermal condition. The number of iterations required for the various Mach numbers is listed in Table 5.2. It indicates that for Mach numbers of 10^{-2} and lower, the number of iterations required increases by a factor of more than two. Even with this increase, the algorithm is still very efficient for this range of low Mach numbers, at least compared with the results reported by Mansour and Hamed [63]. As one can expect, the solutions at the above Mach numbers were almost identical since flows at very low Mach numbers are effectively incompressible. The present work may be one of the first attempts [70] to compute this flow using the compressible form of the Navier-Stokes equations. Most numerical solutions for this problem have been based on the incompressible Navier-Stokes equations.

It is important to mention that no pressure oscillations were detected despite using central differences for the cavity flow cases, even for the highest Reynolds number. This unexpected result might be attributed to : *(1) use of the compressible form*

Table 5.2: Mach number effect for cavity flow, Re=100, 21×21 grid

Mach number	0.2	0 .1	0.05	10^{-2}	10^{-3}	10^{-4}
No. of iterations	25	27	33	85	85	85

which contains the pressure information in the time and other first order derivative terms and (2) the treatment of the pressure boundary condition at the wall, which employs the momentum equations to evaluate the pressure derivative at the wall in an implicit manner. Both of these procedures enhance the pressure-velocity coupling, thus tending to remove the pressure oscillation. It is almost certain that the compressible form of the equations can provide a better pressure-velocity coupling for low Mach number flows, at least for the driven cavity flows. The results for the three-dimensional driven cavity flows also confirmed this pressure smoothing property. The three-dimensional driven cavity results will be presented in a section to follow. Despite its success on the driven cavity cases, further study is required in order to determine if this treatment will also work well for a variety of geometries in the low Mach number regime.

5.1.1.3 Steady flow over a circular cylinder, $Re = 40$ This case is quite different from the previous one. It involves a blunt body immersed in an external stream, conceptually infinite in extent. It is known [71] that steady flow over a circular cylinder can persist up to Reynolds number about 40 (based on diameter). As the Reynolds number is increased further, the flow is expected to become unsteady. Due to symmetry, only the flow in the upper half plane was calculated. An O-type grid was generated with clustering near the wall region and uniform increments in the θ

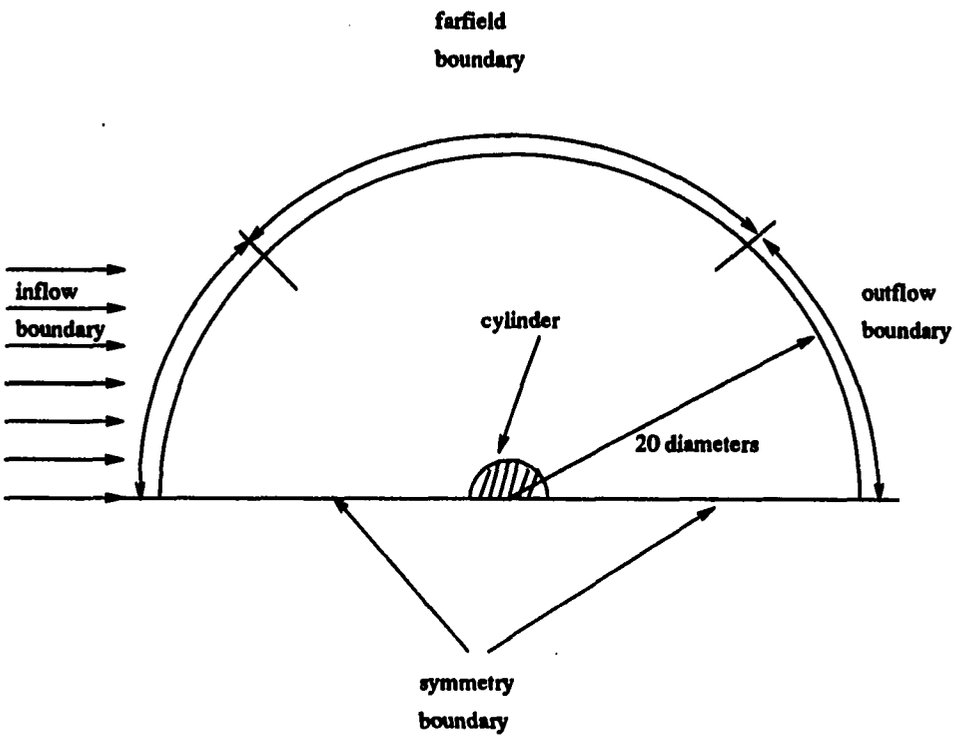

Figure 5.12: Labeling of boundary conditions for steady flow over a circular cylinder

direction. Grid sizes of 31×41, 41×51 and 81×51, were used. The flow was assumed to be isothermal. The outer boundary was located 20 diameters from the cylinder in an attempt to minimize the influence of this artificially imposed boundary. With an O-type grid, the definition of inlet, farfield and exit boundaries is not obvious. The designation of boundary types used in this study can be seen in Fig. 5.12. Majumdar and Rodi [72] also used a similar idea to partition the outer boundary for their O-type grid. The solution was not sensitive to this partition if the outer boundary was located far enough from the cylinder.

The distribution of skin-friction coefficient along the θ direction is shown in Fig. 5.13. The results are nearly grid-independent. Good agreement with the numerical results by Majumdar and Rodi [72] and the experimental results by Acrivos et al. [73] is observed. The pressure coefficient is shown in Fig. 5.14. The present results were compared with those obtained by TenPas and Pletcher [26], Rhie [74] and Son and Hanratty [75]. Good agreement was observed. Figure 5.15 shows the streamlines and pressure contours.

The number of iterations required was between 150 and 200 for the grid sizes studied. The Mach number was 0.05. In this case, the simplified form of the pressure boundary condition, $\partial p/\partial n=0$, was used because the full pressure boundary condition had not been extended to curvilinear boundaries at the time these calculations were made. This condition, which is widely used, does not guarantee a wiggle-free pressure. A small amount of smoothing was added to suppress the pressure oscillation in the form [76]

$$p^{new} = p^{old} + \omega\left(\frac{\partial^2 p^{old}}{\partial \xi^2} + \frac{\partial^2 p^{old}}{\partial \eta^2}\right) \tag{5.6}$$

A value of ω between 0.05 and 0.2 was found to be satisfactory. The widely used

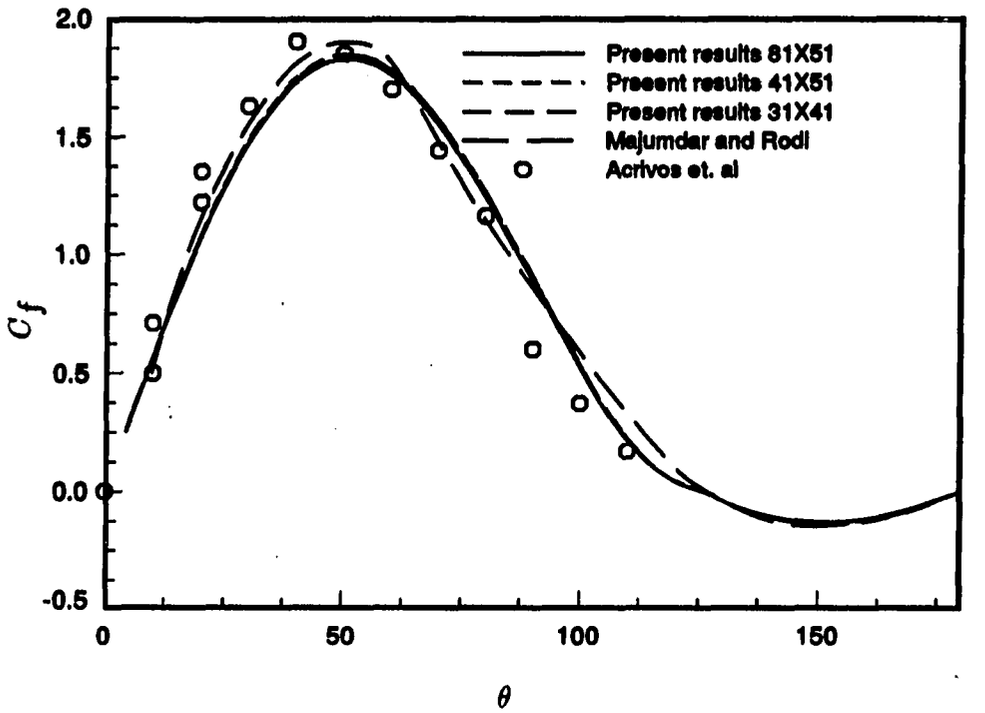

Figure 5.13: Skin-friction coefficient, C_f $(=\tau_w/Re^{1/2})$, for flow over a circular cylinder, Re=40

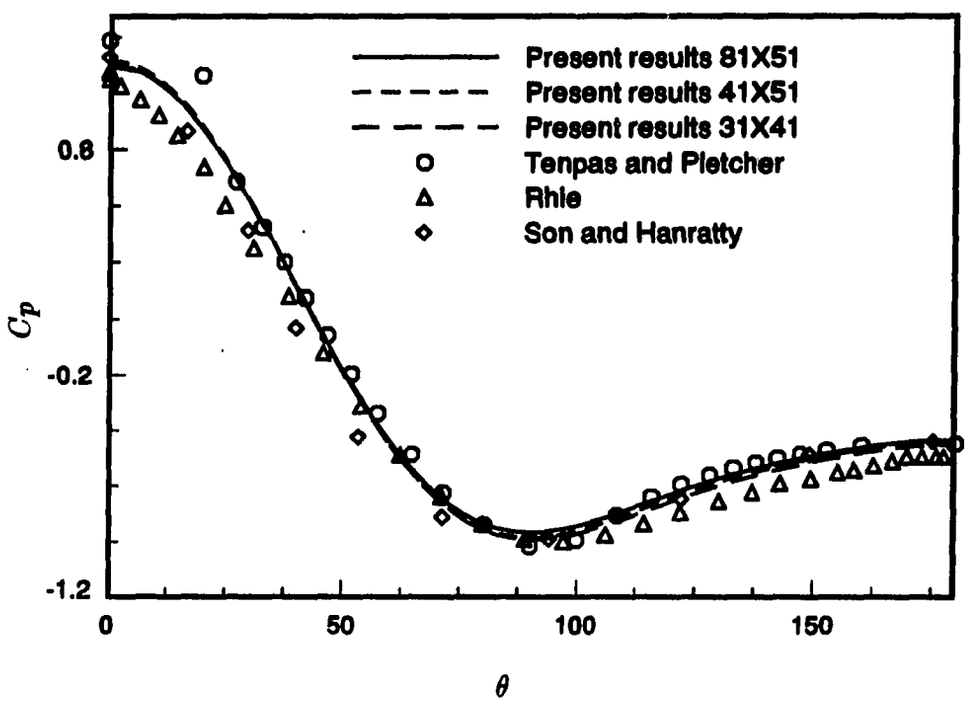

Figure 5.14: Pressure coefficient, C_p $(=(\tilde{p}-\tilde{p}_\infty)/\ \frac{1}{2}\tilde{\rho}_\infty \tilde{u}_\infty^2)$, for flow over a circular cylinder, Re=40

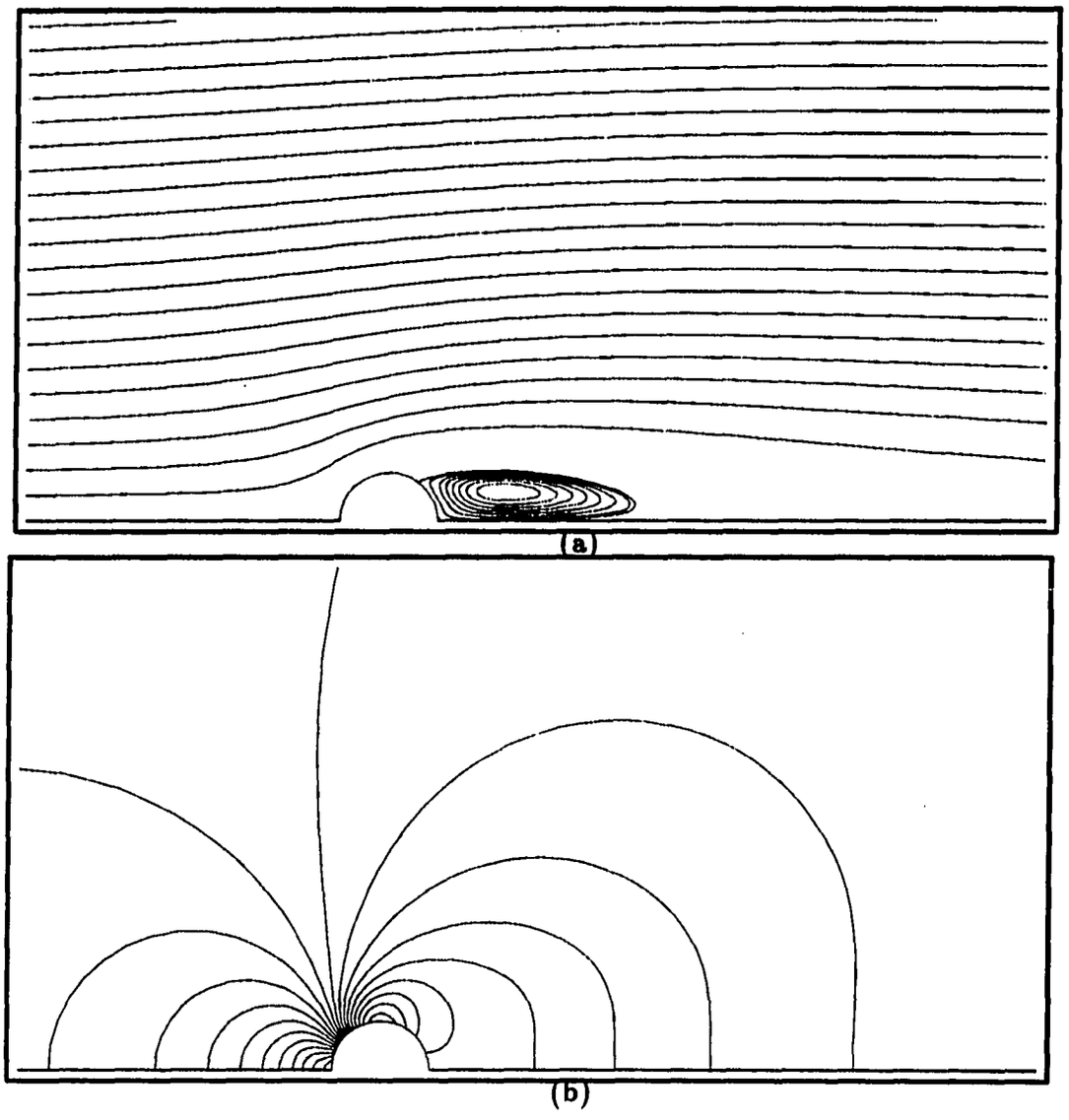

Figure 5.15: Streamlines and pressure contours for flow over a circular cylinder, Re=40, (a) streamlines, (b) pressure contours

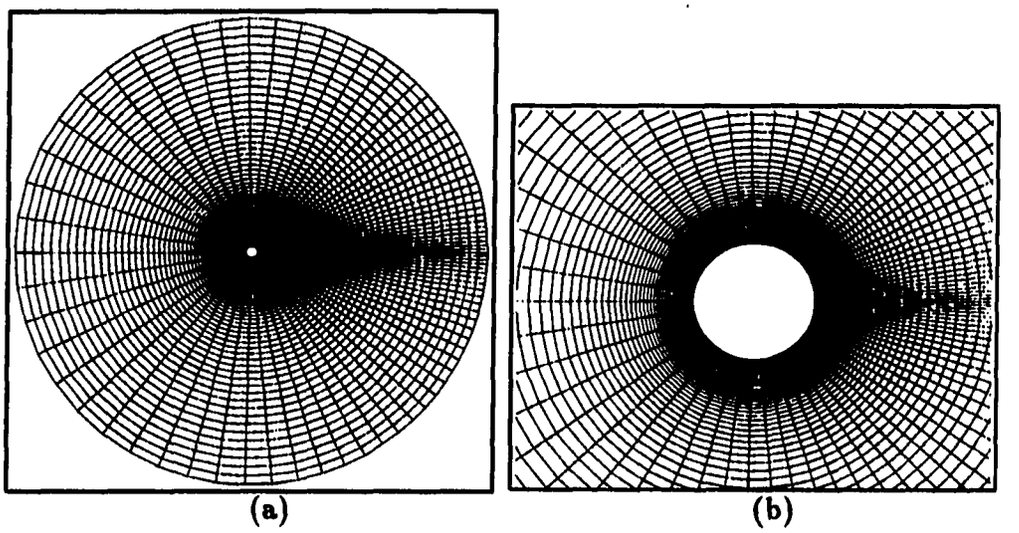

Figure 5.16: 81×101 O-type grid, Re=100, (a) entire domain, (b) close-up

implicit smoothing method [7] was also tried and it was found that the present explicit smoothing was less sensitive to the smoothing parameter ω.

5.1.2 Unsteady flow over a circular cylinder, Re = 100

This case was used to demonstrate the application of the present procedure to unsteady flows. This flow has been studied very extensively in the literature [77], [78]. At this Reynolds number, the flow is no longer symmetric and thus, flow must be computed in the full 360 degree domain. An O-type 81×101 grid was used with mesh clustering near the wall and in the wake region. Figure 5.16 shows this grid layout.

Before performing calculations on this unsteady problem, the implementation of periodic boundary conditions in the θ direction was verified to be trouble-free by running the previous steady state case (Re=40) again with the full 360 degree domain

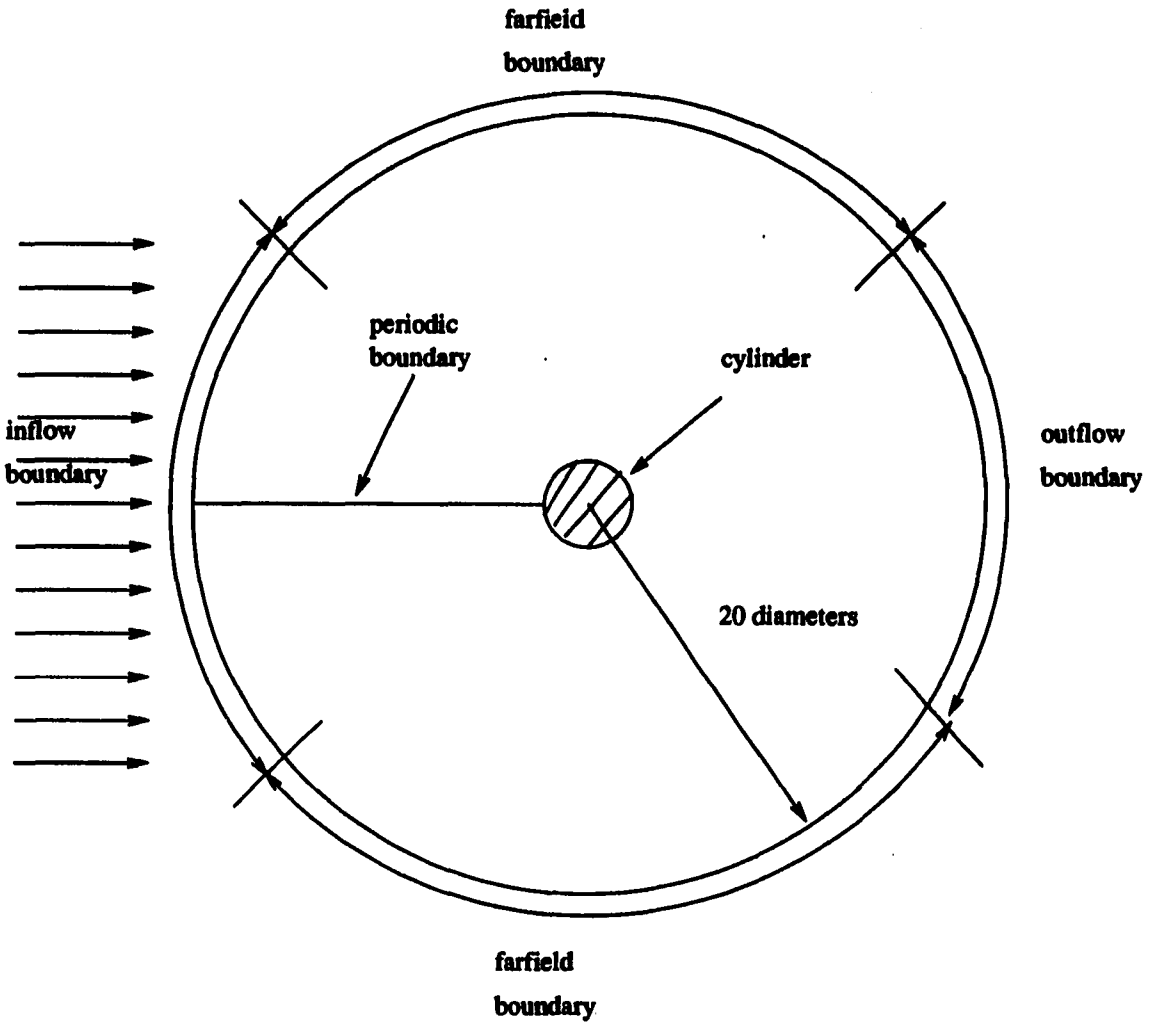

Figure 5.17: Labeling of boundary conditions for unsteady vortex shedding flow over a circular cylinder

and confirming flow symmetry. The outer boundary was located 20 diameters from the cylinder (see Fig. 5.17). An asymmetric trigger technique has been generally used by other investigators [77] to promote the early occurance of the vortex shedding for low Reynolds number flows. However, for a higher Reynolds number calculation, Pan and Chakravarthy [21] reported that the flow developed an asymmetric flow pattern without artificial perturbation. In this study, since the final periodic unsteady solution was of primary interest, the initial condition was efficiently generated by the steady state acceleration technique (local time) which quickly set up a flow pattern with a little asymmetry. The asymmetric trigger technique suggested by Lecointe and Piquet [77] was not needed. Starting from this initial solution, a constant nondimensional time step of 0.02 was used to march the solution in time. Subiterations were used at each time step to eliminate the linearization errors. Initially about 15 subiterations were needed at each time step but this number quickly reduced to 2 for most of the time marching history. The computation was stopped after several periodic cycles were observed. It should be noted that for a true unsteady vortex shedding problem a dense grid (at least locally) is apparently essential to assure that the local small scale transient phenomena are resolved. An attempt to solve this problem on a coarser grid (81×51) failed due to lack of convergence after a long calculation time.

Figure 5.18 shows the final four cycles of the lift coefficient having a constant amplitude of about 0.31 which is almost identical to the result reported by Visbal [78]. The Strouhal number [79] (can be thought as a nondimensional frequency) based on this is about 0.167. This result is within the experimental range $0.16 \sim 0.17$ reported by Roshko [80]. The good agreement of the lift coefficient and Strouhal number with

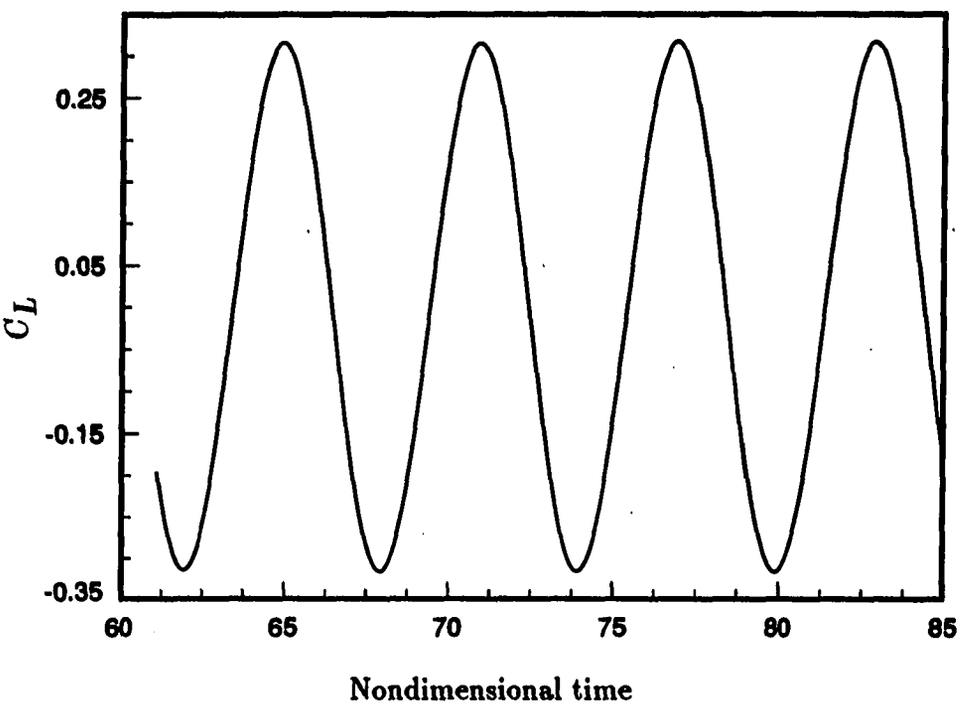

Figure 5.18: Time history of the lift coefficient for the final four cycles of the vortex shedding pattern, Re=100

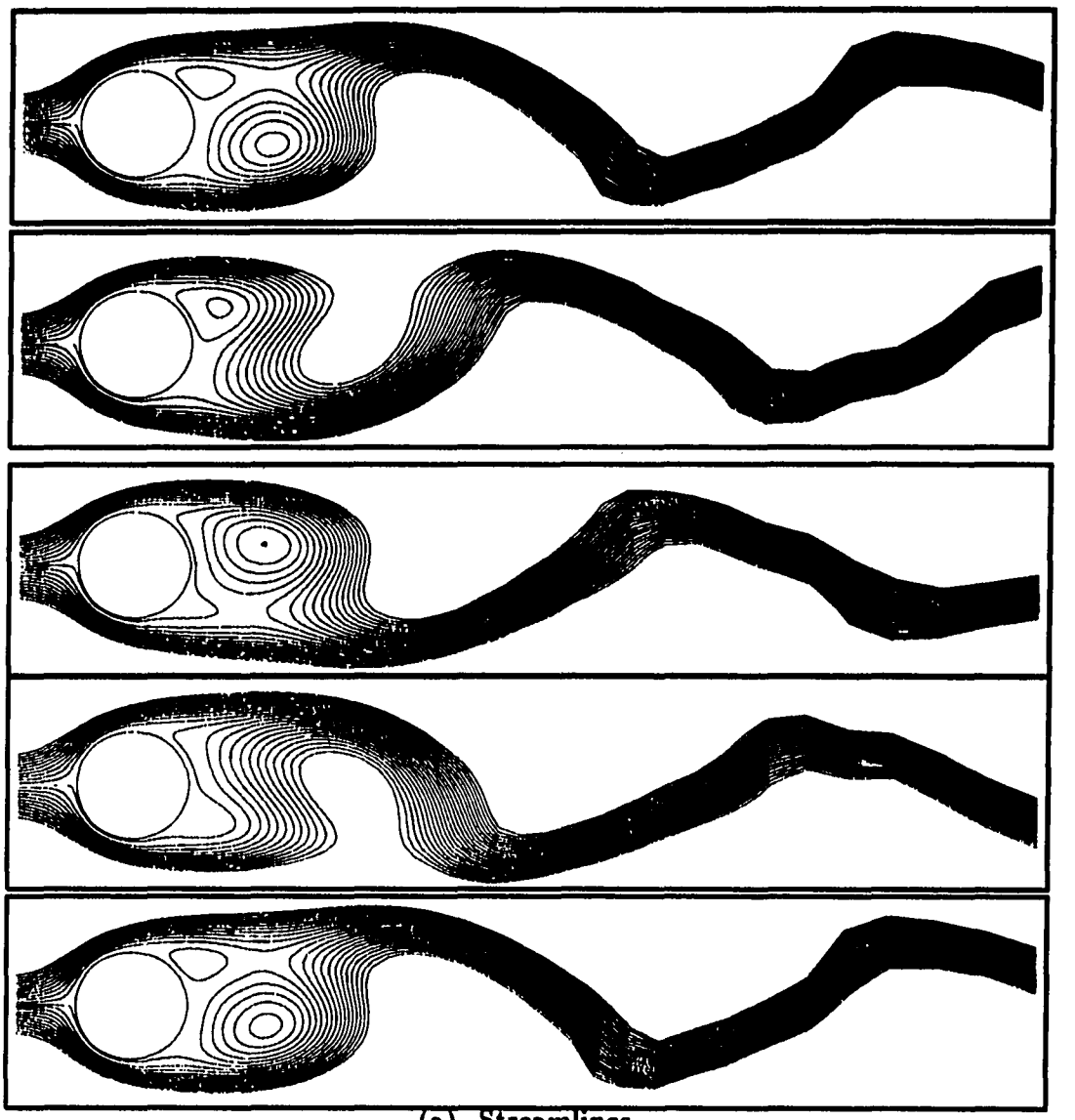

(a). Streamlines

Figure 5.19: Vortex shedding pattern for the final cycle, Re=100, (a) streamlines, (b) vorticity contours

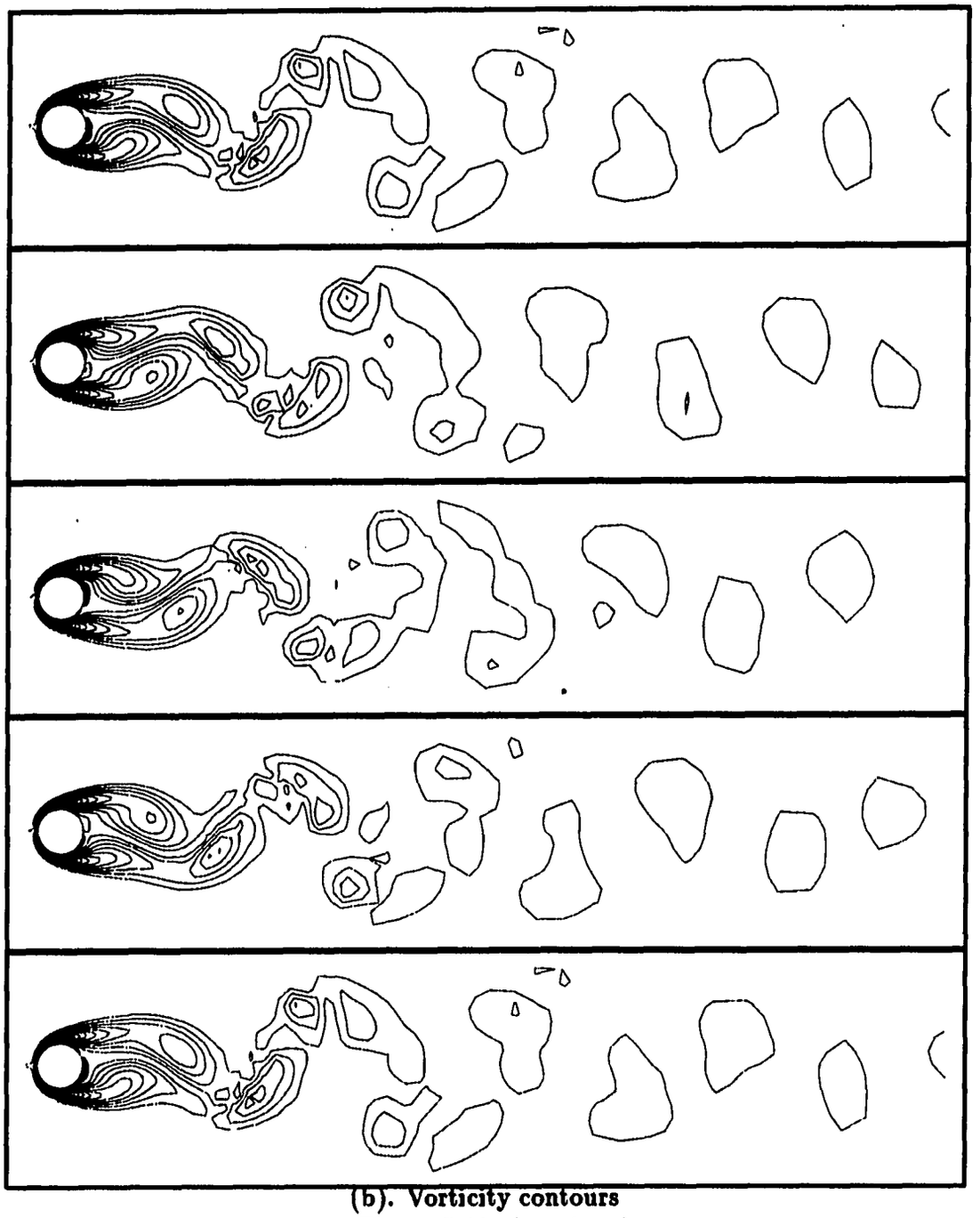

(b). Vorticity contours
Figure 5.19: (continue)

the data in the literature suggests that the present results are quantitatively accurate. Figure 5.19 shows qualitatively the results for streamlines and vorticity contours in the final cycle. The Mach number used was 0.2 and the energy equation was solved in this calculation.

5.1.3 Shock-boundary layer interaction problem

This case demonstrates the shock capturing capability of the present procedure. This case has been studied by several other researchers [8], [9] and a more detailed description of this problem can be obtained from their work. A schematic diagram of the flow configuration is shown in Fig. 5.20. The freestream Mach number is 2 and Reynolds number is 0.296×10^6. The reference length in the definition of this Reynolds number was based on the distance between the leading edge of the plate and the point at which the impinging shock intersected the plate.

The strength of the impinging shock was strong enough to cause the laminar boundary layer to separate. The angle of this impinging shock was 32.6 degrees. An 81×81 grid was used. The grid was uniform in the main flow direction and stretched in the cross-stream direction with the minimum nondimensional grid increment of 1.0×10^{-4} next to the wall. Figure 5.21 shows this grid layout. The computational domain began five grid points ahead of the leading edge of the plate, and top boundary was positioned far enough from the plate to allow the leading edge shock to pass through the outflow boundary. This treatment eliminated the need for using nonreflective boundary conditions at the top boundary.

Freestream conditions were specified at the inlet boundary below the impinging shock. The postshock conditions were specified at the inlet boundary above the

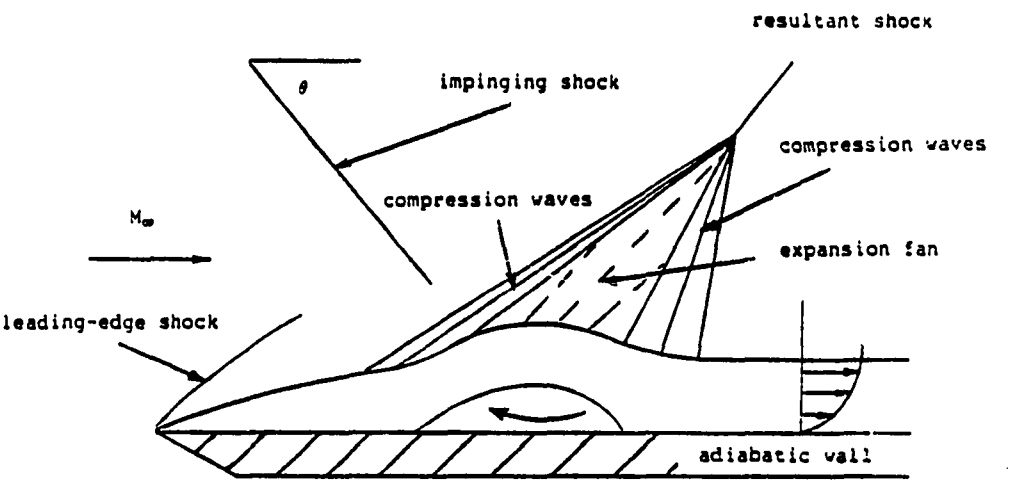

Figure 5.20: Schematic of a shock-boundary layer interaction problem

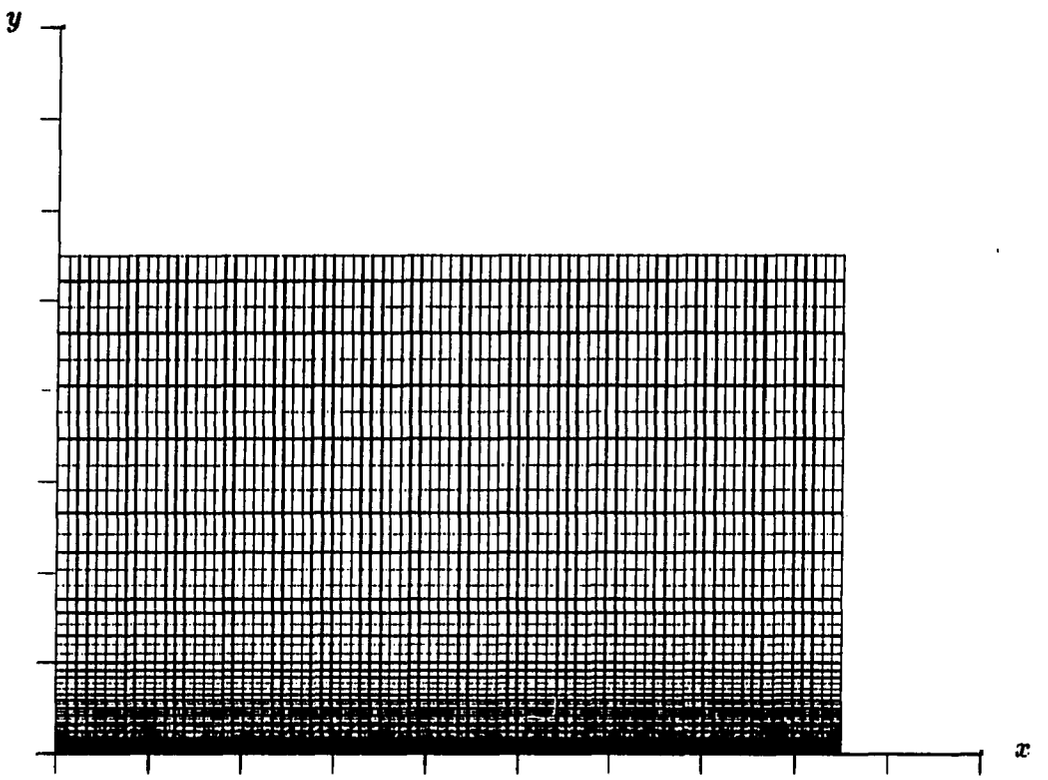

Figure 5.21: 81×81 grid for shock-boundary layer interaction problem.

impinging shock and along the top boundary. Extrapolation was used at the outflow boundary. Noslip conditions, zero normal pressure gradient and an adiabatic wall temperature were used at the wall.

The results are shown for wall pressure and skin-friction distributions in Fig. 5.22 and Fig. 5.23, respectively. The pressure contours are shown in Fig. 5.24. The above results compare reasonably well with the results in the literature [8], [81]-[83] and demonstrate the shock-capturing capability of the present scheme. About a thousand iterations were required to obtain the present converged solution.

For this supersonic case, smoothing was needed for all variables instead of pressure only as for low Mach number cases. Clearly, the shock resolution obtained by this method can be improved, but the present results suggest that the formulation of the scheme is fundamentally correct and sufficient for capturing shocks.

Most of the above calculations were performed on the Apollo DN 10,000 workstation. The CPU time was approximately 0.0048 sec/node/iteration.

5.2 Three-Dimensional Driven Cavity Results

Before solving the more complicated three-dimensional unsteady liquid sloshing problems, the flow inside a 3-D driven cavity was used to evaluate the present numerical algorithm for three-dimensional geometries. This case was used to test the accuracy and convergence property of the 3-D CSIP algorithm coupled with the artificial compressibility method for solving both steady and unsteady incompressible flows. A schematic diagram of the cubic cavity configuration is shown in Fig. 5.25.

The incompressible equations without the gravity term in Eq. (2.16) were used for this cavity flow calculation. The boundary condition treatment was similar to its

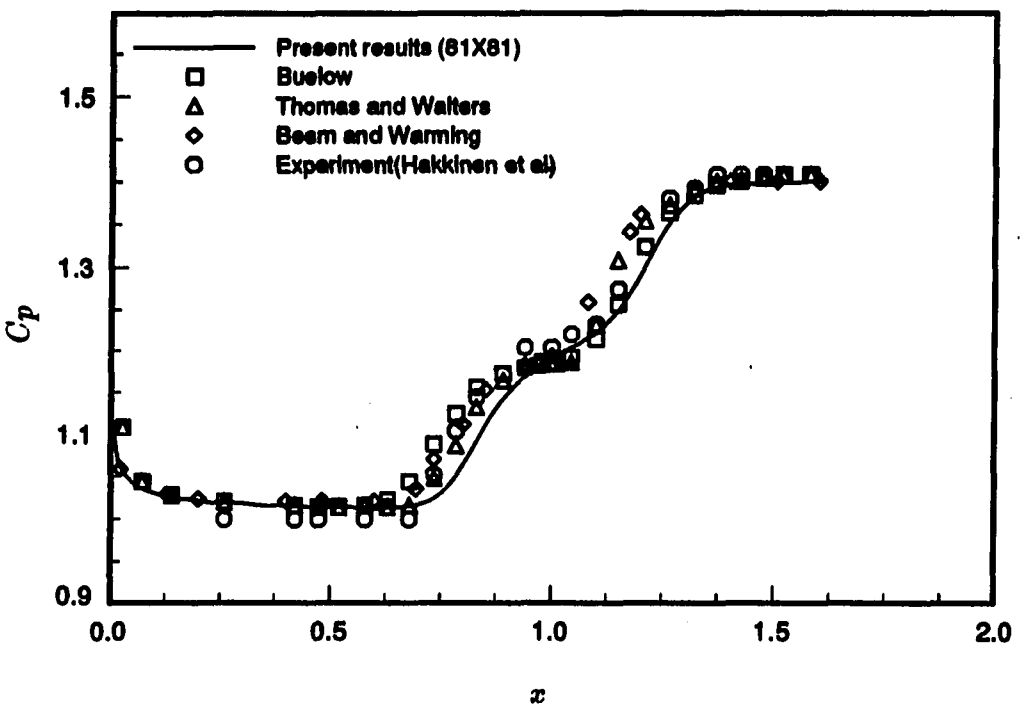

Figure 5.22: Pressure coefficient, C_p $(=\tilde{p}/\tilde{p}_\infty)$, distribution along the wall

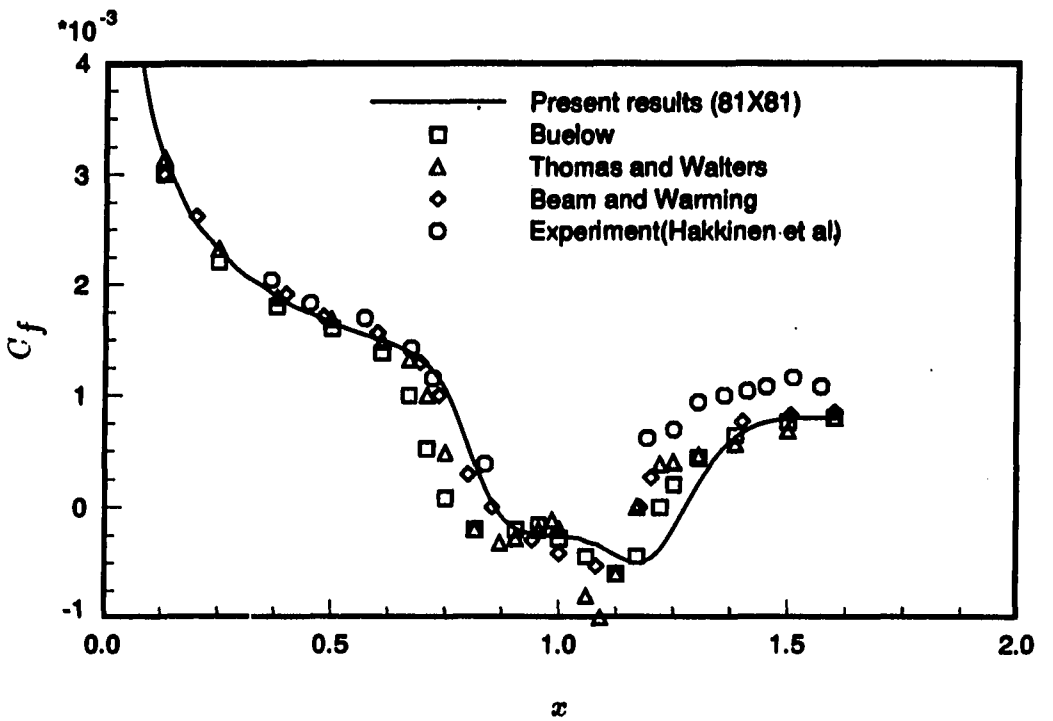

Figure 5.23: Skin-friction coefficient, C_f $(=2\tau_w/Re)$, distribution along the wall

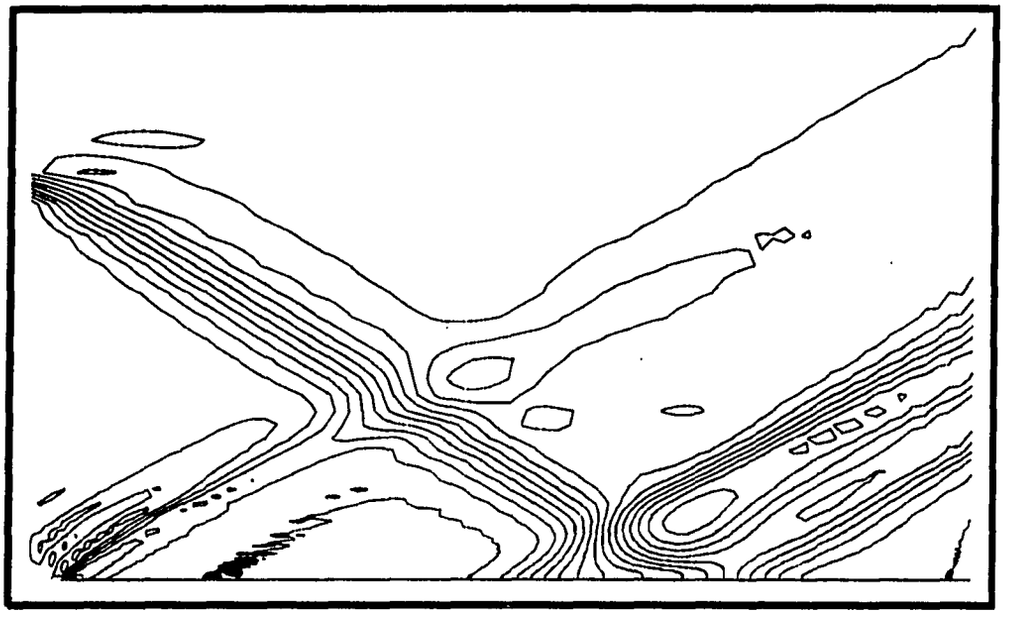

Figure 5.24: Pressure contours for shock-boundary layer interaction problem

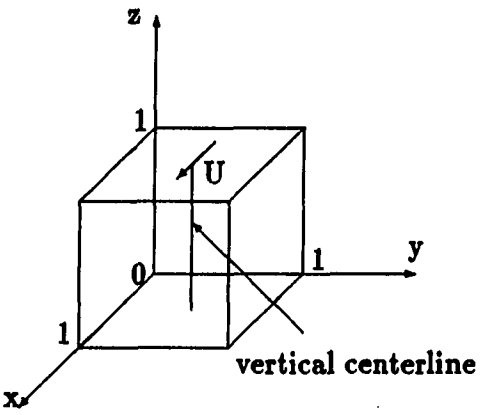

Figure 5.25: Schematic of a 3-D driven cavity flow

2-D counterpart. The noslip condition for three velocity components and the normal momentum equation were used at the wall of the cubic cavity. Second order central differences for all the spatial derivative terms and a first order forward difference for the time term were used. An artificial time derivative of pressure was added to the continuity equation to couple the continuity and momentum equations (see Eq. (4.15)). The continuity and momentum equations were then cast into the CSIP 7-point formula and solved simultaneously for the unknowns u, v, w and p. A flow of $Re = 100$ was investigated. For the steady state calculation, the convergence acceleration technique (see Eqs. (4.28) and (4.29)) was applied to obtain a faster convergence rate. Two grids, one 21×21×21 and the other 29×29×29 were used to study this flow. The distribution of the u velocity component along the vertical centerline at $y = 1/2$ plane is shown in Fig. 5.26. The agreement between the present solution and those obtained by Rosenfeld, Kwak and Vinokur [84] and Ku, Hirsh and Taylor [85] is good. Also shown in this figure is the effect of the grid refinement. It

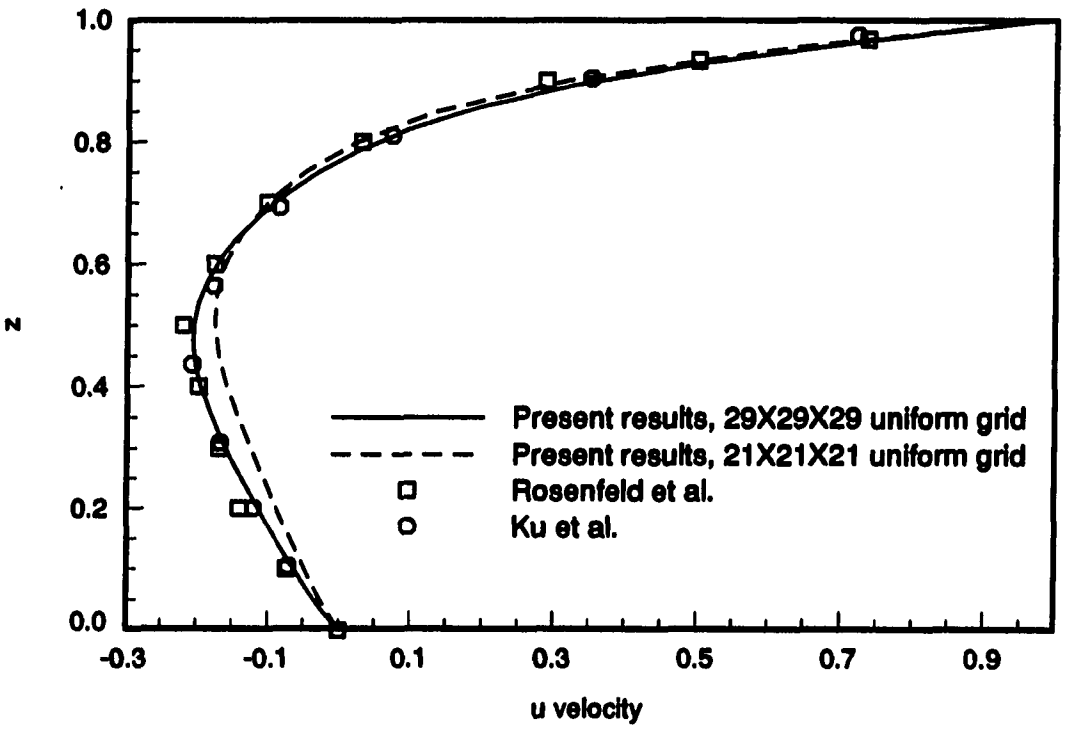

Figure 5.26: Predicted u velocity distribution along the vertical centerline of a 3-D driven cavity at y=1/2 plane, Re=100

required 145 iterations to obtain this converged solution for the 21×21×21 case and 194 iterations for the 29×29×29 case.

An impulsively started unsteady cavity flow was also studied to determine the unsteady convergence behavior of the 3-D CSIP procedure coupled with the artificial compressibility method. The Reynolds number was 100 and the grid was 21×21×21. Subiterations were required to obtain a true unsteady solution. A constant nondimensional time step of 0.02 was used. For the first time step, 85 subiterations were required. The number of subiterations dropped to about 10 after 10 time steps and finally became 1 for most of the time steps. The time history for velocity and pressure at the center point of the cubic cavity are shown in Figs. 5.27 and 5.28, respectively. There are no unsteady 3-D cavity data available in the literature at this time for comparison with the present results. However, the results obtained from this unsteady calculation do indicate that the present CSIP procedure coupled with the artificial compressibility method is an effective method to simulate unsteady three-dimensional flows. It should be noted that for the above calculations, with regular grids and central differences in the incompressible equations, a small amount of pressure smoothing using Eq. (5.6) was required to remove the spatial pressure oscillation. The compressible form of the Navier-Stokes equations was also used to solve this flow problem and it was found that the pressure oscillations were automatically removed. It confirmed again the favorable pressure smoothing properties of the present primitive variable CSIP formulation of the compressible form of equations.

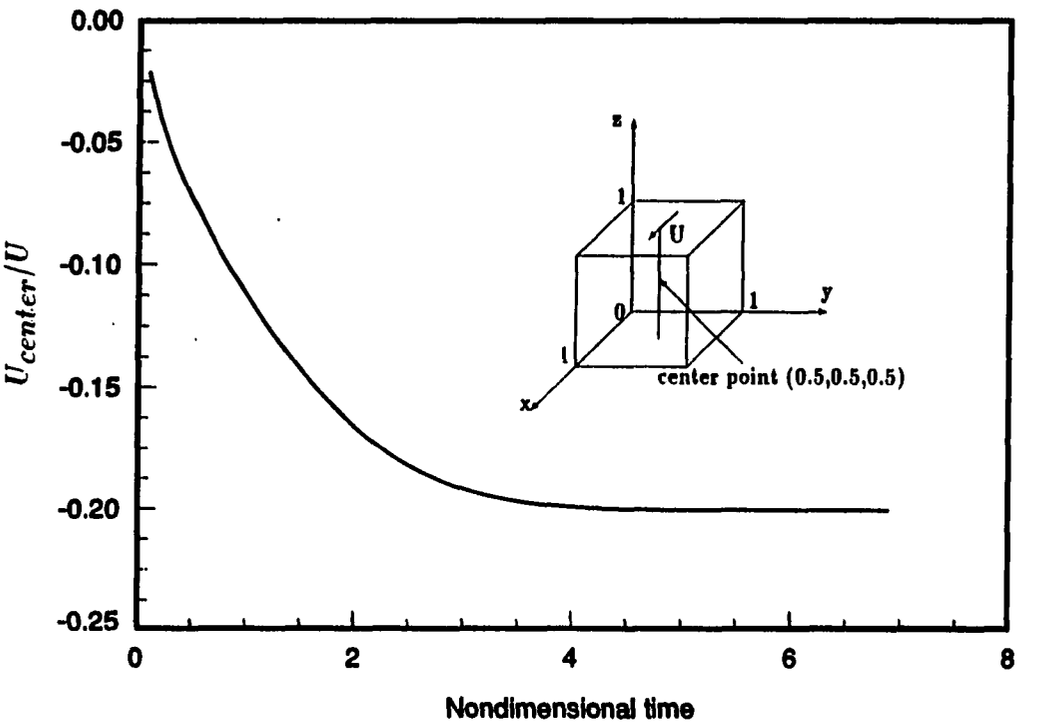

Figure 5.27: Time evolution of the u velocity component at the center point of the 3-D driven cavity, Re=100

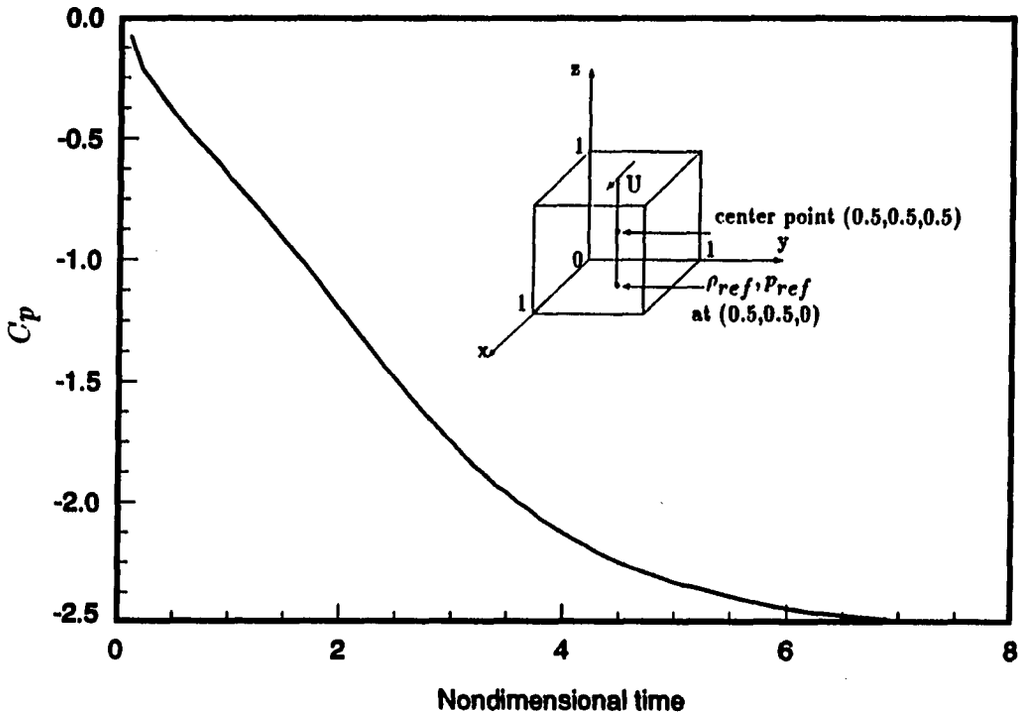

Figure 5.28: Time evolution of the pressure coefficient, C_p, at the center point of the 3-D driven cavity, Re=100, $(C_p = Re \times (\tilde{p}_{center} - \tilde{p}_{ref})/\tilde{\rho}_{ref} U^2)$

Table 5.3: Summary of test cases for the three-dimensional liquid sloshing flows

Case	Type of spin-up	Liquid	Rpm	Arm (cm)[a]	Re	Fr	We
1.	I.C.[b] sym.[c]	Glycerin	60	0	21.9	0.51	207.6
2.	I.C. sym.	Kerosene	60	0	2254.7	0.51	284.9
3.	Grd.[d] sym.	Glycerin	0~60	0	21.9	0.51	207.6
4.	Imp.[e] sym.	Glycerin	60	0	21.9	0.51	207.6
5.	I.C. asym.[f]	Glycerin	30	12.8	21.9	0.51	207.6
6.	I.C. asym.	Glycerin	60	44.7	181.4	3.25	12002.1

[a]Length of rotation arm.
[b]Initially capped.
[c]Symmetric.
[d]Gradually.
[e]Impulsively.
[f]Asymmetric.

5.3 Three-Dimensional Liquid Sloshing Results

A schematic of this partially filled spherical container undergoing a rotating-nutating motion is shown in Fig. 2.1. Even though several features have been included in the present formulation in anticipation of the interaction with the space structure as mentioned in Chapter 1, the scheme for treating the liquid sloshing itself must be validated to the extent possible before interaction with the structure is considered further. Several cases for which the steady state solution is known analytically will be investigated and validated in the following sections. The several cases investigated are listed in Table 5.3 and the fluid properties used for these calculations are listed in Table 5.4.

Table 5.4: Liquid properties [a] at 20 degree C used for the three-dimensional liquid sloshing flows

Liquid	$\nu^b\ (m^2/s)$	$\rho^c\ (kg/m^3)$	$\Gamma^d\ (N/m)$
Glycerin	1.18×10^{-3}	1264.0	6.33×10^{-2}
Kerosene	1.145×10^{-5}	767.2	2.8×10^{-2}

[a]Source: Ref. [86].
[b]Kinematic viscosity.
[c]Density.
[d]Surface tension coefficient.

5.3.1 Axisymmetric spin-up

Four axisymmetric spin-up problems were studied. The configuration of this first test case is shown in Fig. 5.29. The radius of the spherical container is equal to 6.4 centimeters and the rotation arm, h_i, is equal to 0. Due to the symmetry of this problem, the solution should be independent of position in the circumferential direction. This will provide one easy check on the validity of the code. As the spinning is initiated, the liquid and free surface begin to move relative to the container and eventually reach a steady-state equilibrium condition in which solid-body rotation prevails. Computations were made for fluids of two different viscosities, one corresponding to glycerin and one corresponding to kerosene, and for three different types of spin-up, one corresponding to an impulsive spin-up, one corresponding to a gradual spin-up and another corresponding to an initially capped spin-up. The three types of spin-up are described as follows:

1. **Impulsive spin-up:** At time zero, the spherical container half-filled with a liquid impulsively starts to rotate with a constant rotational speed about a

specified rotation axis (the axis of symmetry of the container, for the axisymmetric spin-up case). The initial absolute velocity is zero everywhere except at the wall of the container.

2. **Gradual spin-up:** At time zero, the spherical container half-filled with a liquid gradually starts to rotate with rotational speed starting from zero and smoothly increased to a desired constant value about a specified rotation axis. The initial absolute velocity is zero everywhere.

3. **Initially capped spin-up:** Initially, the spherical container half-filled with a liquid has been spun about a specified rotation axis at a constant rotational speed and has reached a solid-body rotation. A cap covers the liquid surface keeping it level. At time zero, the cap is suddenly removed (or broken) and the liquid surface starts to rise (or drop) until another equilibrium position is reached. The initial absolute velocity is distributed according to the condition of solid-body rotation.

For the same rotational speed of 60 rpm, the spin-up phenomena were found to be quite different for the two fluids and spin-up types. These four axisymmetric spin-up cases are described as follows.

5.3.1.1 Initially capped spin-up; liquid: glycerin Initially, the spherical container half-filled with glycerin has been spun about its axis of symmetry in a rotational speed of 60 rpm and has reached a solid-body rotation. Since the liquid surface was covered by a cap, there was no free surface motion at all. The initial

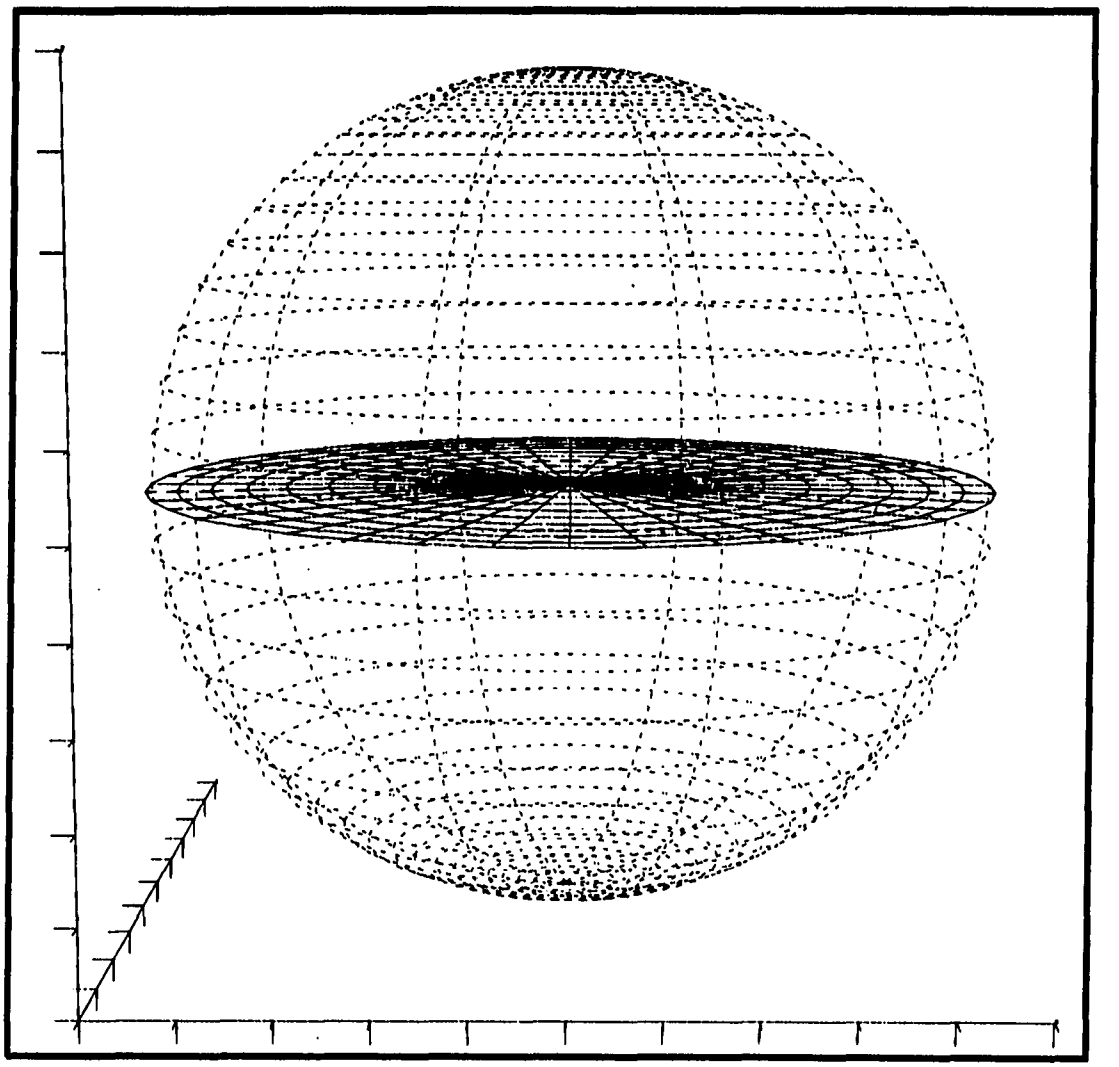

Figure 5.29: The half-filled spherical container; at rest configuration

absolute velocity distribution is as follows:

$$V_r = 0$$

$$V_\theta = r\omega$$

$$V_z = 0$$

where V_r is the velocity component in the radial direction, V_θ is the velocity component in the circumferential direction, V_z is the velocity component in the direction normal to the previous two directions, r is the distance in the radial direction away from the line of symmetry and ω is the rotational speed (60 rpm) (w.r.t. x_{23} axis). It should be noted that the governing equations were expressed in terms of the relative velocity (relative to the final solid-body rotation) and therefore u_{3_i}=0 was actually used as the initial condition for velocities. The hydrostatic pressure distribution was initially specified.

At time zero, the cap is suddenly removed (or broken) and the free surface starts to rise near the wall of the container and drop near the center of the free surface in response to the sudden change of the pressure field. The properties of glycerin are listed in Table 5.4. Some selected velocity vector plots illustrating the general flow pattern at different times are shown in Fig. 5.30. The results shown are in the $x_{22} = 0$ plane. The time shown on the figures has been nondimensionalized using a characteristic time based on the radius of the container and the rotational speed at the wall (equal to 0.1592 sec. in this case). The motion of this flow at different times can be seen from the velocity vectors in Fig. 5.30. The dotted lines inserted in Fig. 5.30 indicate the analytical steady state equilibrium (relative to the x_2 frame) free surface position. The analytical steady state equilibrium free surface solutions

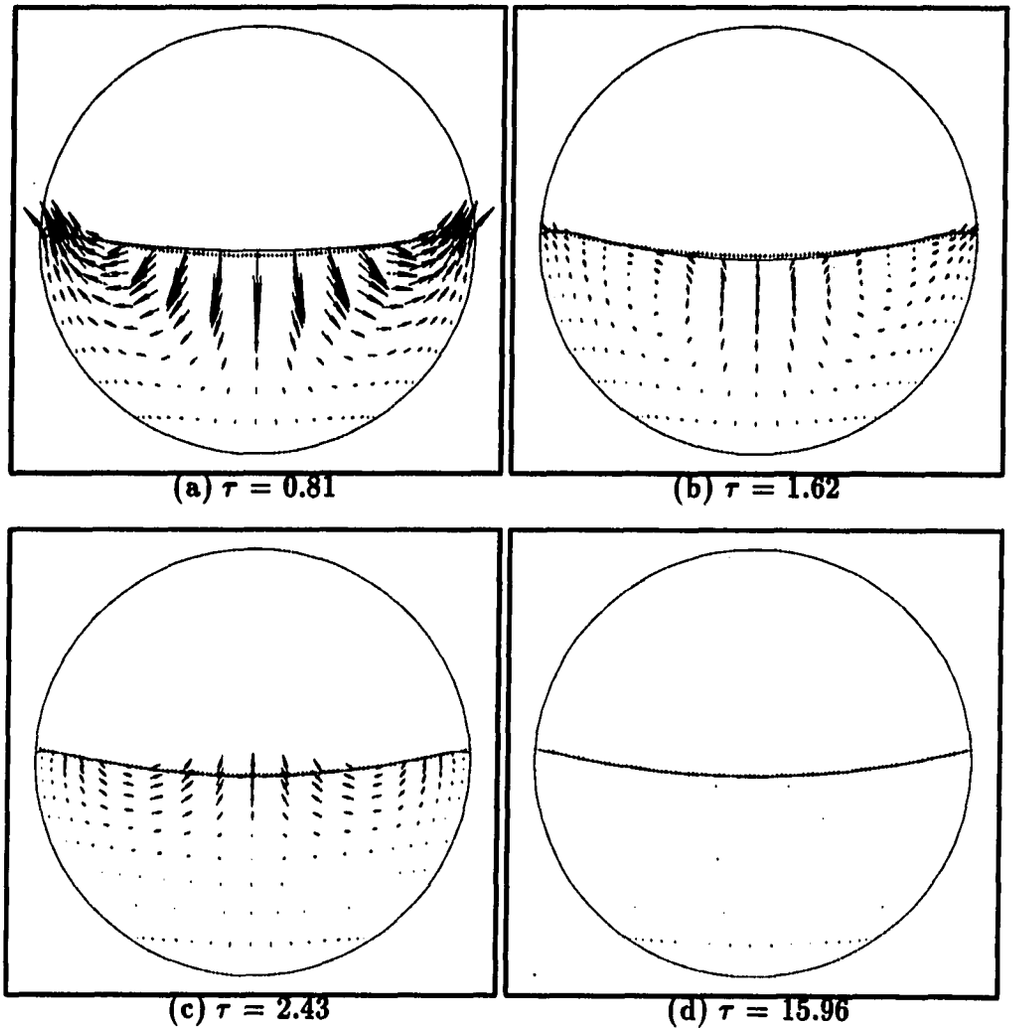

Figure 5.30: Selected velocity vector plots at x_{22}=0 plane for the axisymmetric initially capped spin-up of a spherical container half filled with glycerin (the dotted line indicates the steady state analytical free surface position)

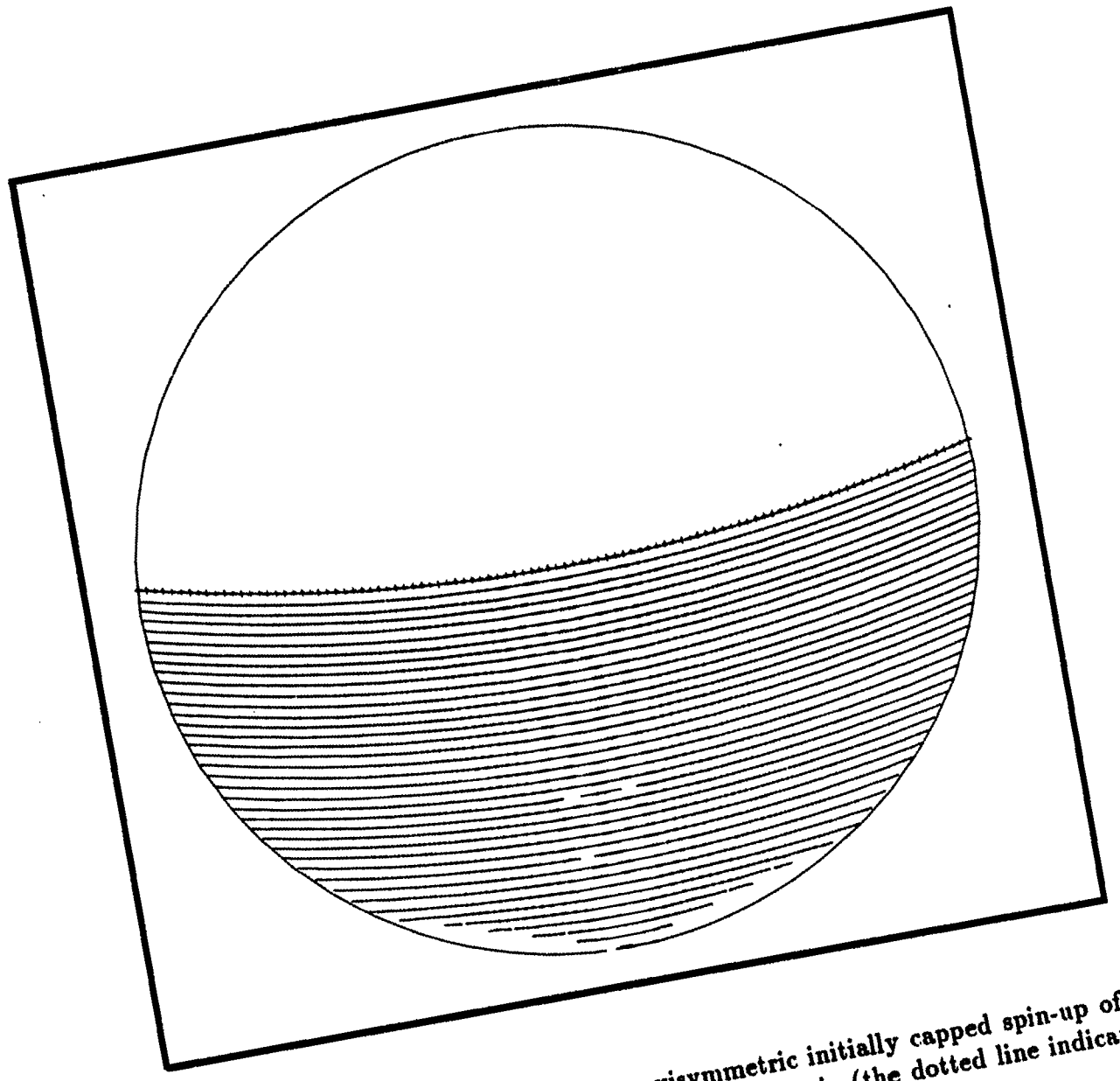

Figure 5.31: Pressure contours for the axisymmetric initially capped spin-up of a spherical container half filled with glycerin (the dotted line indicates the steady state analytical free surface position)

were derived by the present author and are listed in Appendix E. The velocities are largest near the free surface and are significantly smaller near the bottom of the container. As time goes on, the fluid continues to move and eventually passes (or overshoots) the equilibrium position. By time $\tau = 1.62$, magnitude of the flow has been reduced and the flow pattern has begun to reverse itself. This can be seen in Fig. 5.30b and more clearly in Fig. 5.30c. This flow continues to oscillate about the equilibrium position with diminishing amplitude until the new equilibrium position is reached at about $\tau = 15.96$ in Fig. 5.30d (see also Fig. 5.32). It should be noted that the magnitude of the velocities in Fig. 5.30d has become very small as the final solid-body rotation is approached. The velocities shown here are relative to the solid-body rotation expected at steady state, as pointed out in a previous section. The pressure contours are shown in Fig. 5.31. The numerical free surface position matches exceptionally well with the analytical solution.

To permit a more detailed analysis of the flow pattern under this spin-up condition, the time histories of the free surface positions at the wall of the container and at the center of the free surface and the x_{23} component of the velocity were recorded. Figure 5.32 shows the free surface position at the wall and at the center of the free surface for glycerin during the spin-up process. Probably due to the sudden removal of the cap, the free surface position oscillates about the equilibrium position. This oscillation, however, is damped out quickly by the viscosity of the fluid. Figure 5.33 illustrates the same phenomena but shows the time evolution of the component of the velocity (x_{23} component) normal to the free surface at the center of the container. These quantitatively results again show the effectiveness and accuracy (at least for the steady state solution) of the present numerical algorithm.

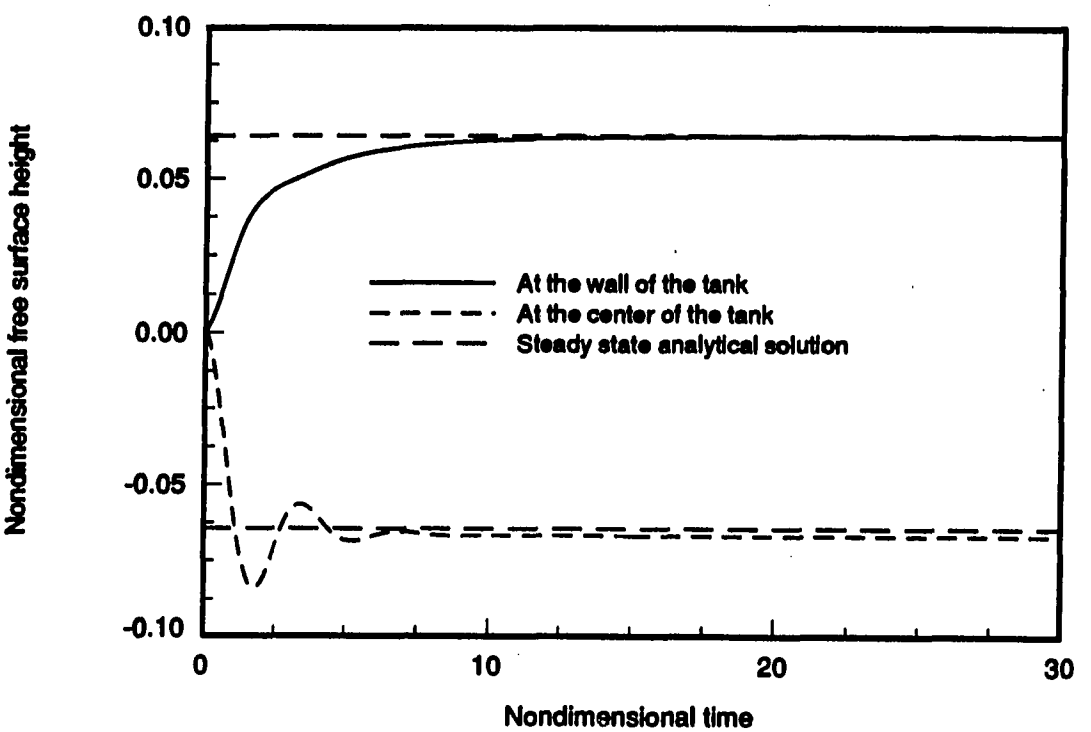

Figure 5.32: The time history of the nondimensional free surface height for the axisymmetric initially capped spin-up of a spherical container half filled with glycerin

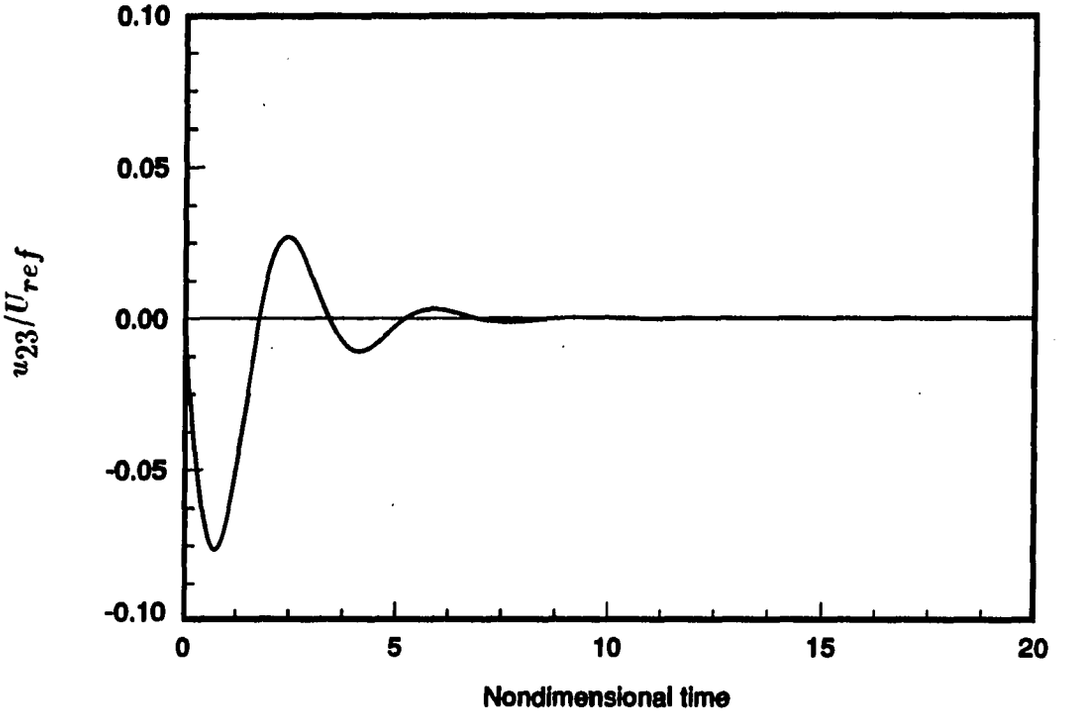

Figure 5.33: The time history of the u_{23} velocity component on the free surface at the center of rotation for the axisymmetric initially capped spin-up of a spherical container half-filled with glycerin

For this spin-up problem, the number of subiterations at the first time step was about 50 but then the number quickly dropped to less than 10 after 20 time steps and finally became 1 as the solution approached to the final steady state. A 11×11×11 grid was used for the calculation. A nondimensional time step of 0.015 was used throughout the calculation. The characteristic nondimensional parameters, Re, Fr and We, for this calculation are:

Reynolds number, $Re = 21.9$

Froude number, $Fr = 0.51$

Weber number, $We = 207.6$

The Reynolds number, Re, and Weber number, We, have been defined previously. The Froude number, Fr, is defined as follows:

$$Fr = \frac{V_{ref}}{\sqrt{gh}}$$

where h is the initial free surface depth and g the gravitational acceleration.

5.3.1.2 Initially capped spin-up; liquid: kerosene The initially capped spin-up calculations were repeated with kerosene, a fluid whose kinematic viscosity is only about 1 % of that of glycerin (see Table 5.4). All rotation parameters were identical with the previous glycerin case. The final analytical equilibrium free surface position is expected to be the same as for the glycerin case. With this less viscous fluid, the general flow pattern was found to be quite similar to the previous case and will not be repeated here; however several interesting results deserve further discussion.

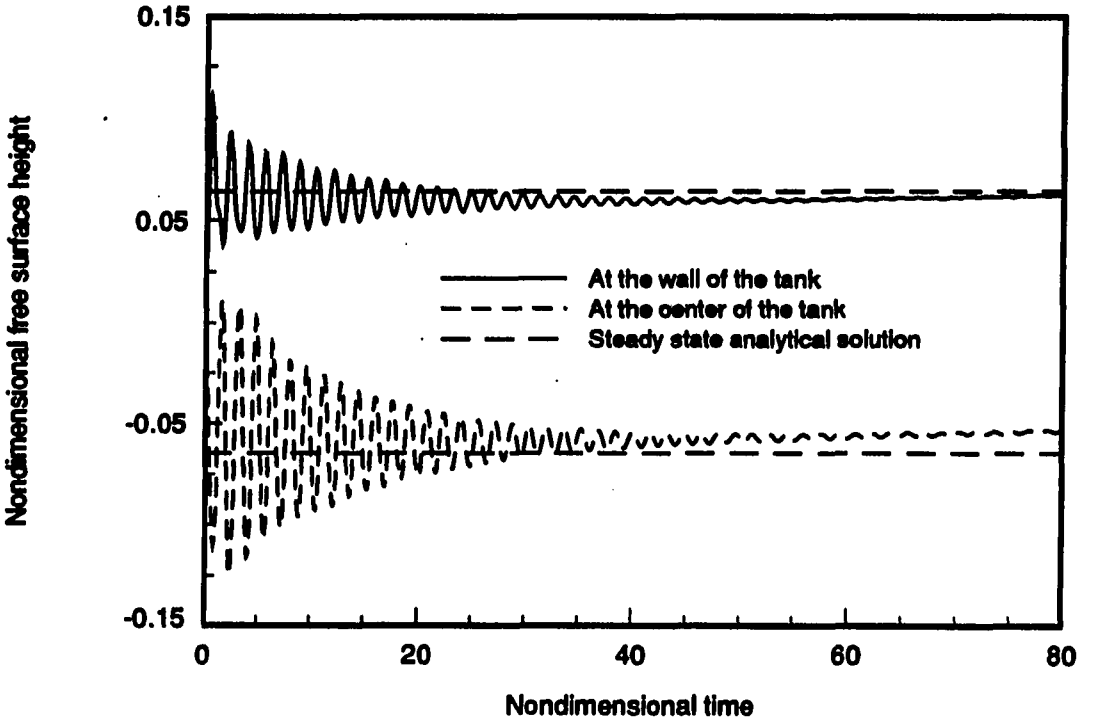

Figure 5.34: The time history of the nondimensional free surface height for the axisymmetric initially capped spin-up of a spherical container half filled with kerosene

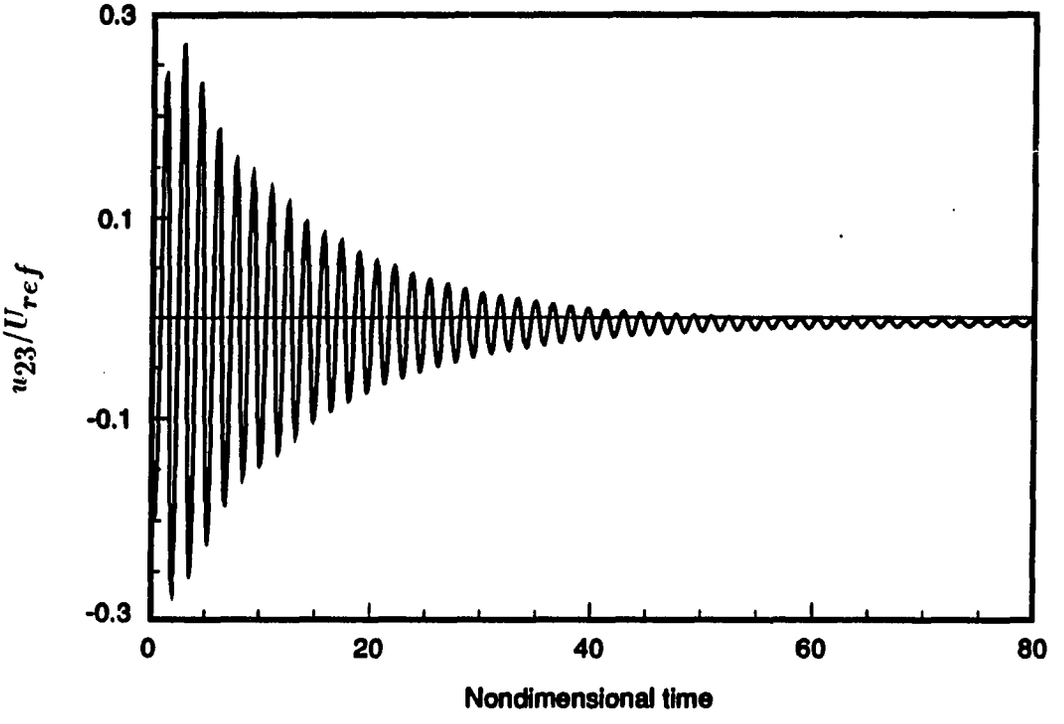

Figure 5.35: The time history of the u_{23} velocity component on the free surface at the center of rotation for the axisymmetric initially capped spin-up of a spherical container half-filled with kerosene

Figure 5.34 indicates the variation of the free surface position at the wall and tank center as a function of nondimensional time during the spin-up process for kerosene. Since the viscosity of kerosene is a factor of 100 less than that of glycerin, the free surface oscillations appear to damp out much more slowly than was observed for glycerin. This behavior is believed to be real although no experimental data have been found to date to clarify this point. The final computed steady state position of the free surface agrees reasonably well with the analytical solution. Figure 5.35 shows the computed velocity component normal to the free surface at the center of the container as a function of time. Slowly damped oscillatory motion is evident. The spin-up with kerosene took about four times longer than that with glycerin to reach final steady state solid-body rotation (both cases used the same reference time and this was estimated from the plots shown previously).

The kerosene calculations were made with the same grid as used to obtain the glycerin results. During the course of early computations, it was found that the free surface developed a saw-toothed profile of small amplitude in the radial direction which appeared to slow convergence at each time step. Due to much smaller viscosity of kerosene compared to glycerin, the effective Reynolds number of this flow is much higher than for the glycerin case. As a result, the saw-toothed profile might have been due to the use of central differences in the spatial derivative terms in the kinematic equation at the higher Reynolds number. If the use of central differences at high Reynolds numbers was the source of the problem, it could have been remedied by the use of a finer grid which, of course, would have increased the required computational effort considerably. Instead, a small amount of smoothing was added to remove this undesired profile and stabilize the calculation. The smoothing was of the following

form:

$$F^{new} = F^{old} + s(\frac{\partial^2 F^{old}}{\partial z_2^2}) \tag{5.7}$$

where s is the smoothing parameter, F is the free surface height function (see free surface kinematic equation) and z_2 is the radial direction. A value of $s = 9 \times 10^{-3}$ was used for this case. The second derivative in the expression above was represented, of course, in difference form. The characteristic nondimensional parameters for this calculation are:

Reynolds number, $Re = 2254.7$

Froude number, $Fr = 0.51$

Weber number, $We = 284.9$

It should be noted that the use of the smoothing in computing the free surface height function, F, for this calculation resulted in slightly less than a 1% loss of the initial total volume. Although this discrepancy was insignificant, further investigation on this subject is warranted in the future. We will discuss this effect further in another section.

5.3.1.3 Gradual spin-up; liquid: glycerin As mentioned before, the high frequency free surface oscillations were possibly due to natural overshoots arising from the sudden removal of the cap during the spin-up process. To further understand this phenomenon, a third test for this configuration was conducted for glycerin again in the following way. The container was spun up with the rotational speed being gradually increased from 0 to 60 rpm by a sine function of time during the nondimensional time interval from zero to five. This rotational speed was specified as:

$\omega = 30(\sin\theta + 1)$ rpm, for $0 \leq \tau \leq 5$

where $\theta = \frac{\pi}{5}\tau - \frac{\pi}{2}$

and

$\omega = 60$ rpm, for $\tau > 5$

Figure 5.36 indicates the variation of the free surface position at the wall and tank center as a function of nondimensional time during the gradual spin-up process. The oscillatory phenomena in Fig. 5.32 disappeared and instead, a nonoscillatory ramp-up of the free surface at the wall and drop at the tank center was observed. This suggests that the oscillations are promoted by the abrupt nature of the sudden removal of the cap during the spin-up process. The final steady state free surface positions agree very well the analytical solutions.

5.3.1.4 Impulsive spin-up; liquid: glycerin At time zero, the spherical container half-filled with glycerin impulsively started to rotate about its axis of symmetry. The initial absolute velocity was zero everywhere except at the wall of the container at which a rotational speed of 60 rpm was suddenly applied. Due to the use of the relative velocity in the formulation, a negative distribution of the solid-body rotation velocity was specified everywhere initially except at the wall where a zero relative velocity was specified. A $11\times11\times11$ grid was used again for this case. The free surface positions at the wall of the container and at the center of the free surface are shown in Fig. 5.37. No free surface overshoots were observed in this case. Probably due to being spun up impulsively, the flow reached the final steady state equilibrium position earlier than for the previous gradual spin-up case. The velocity component normal to the free surface at the center point of the free surface is shown

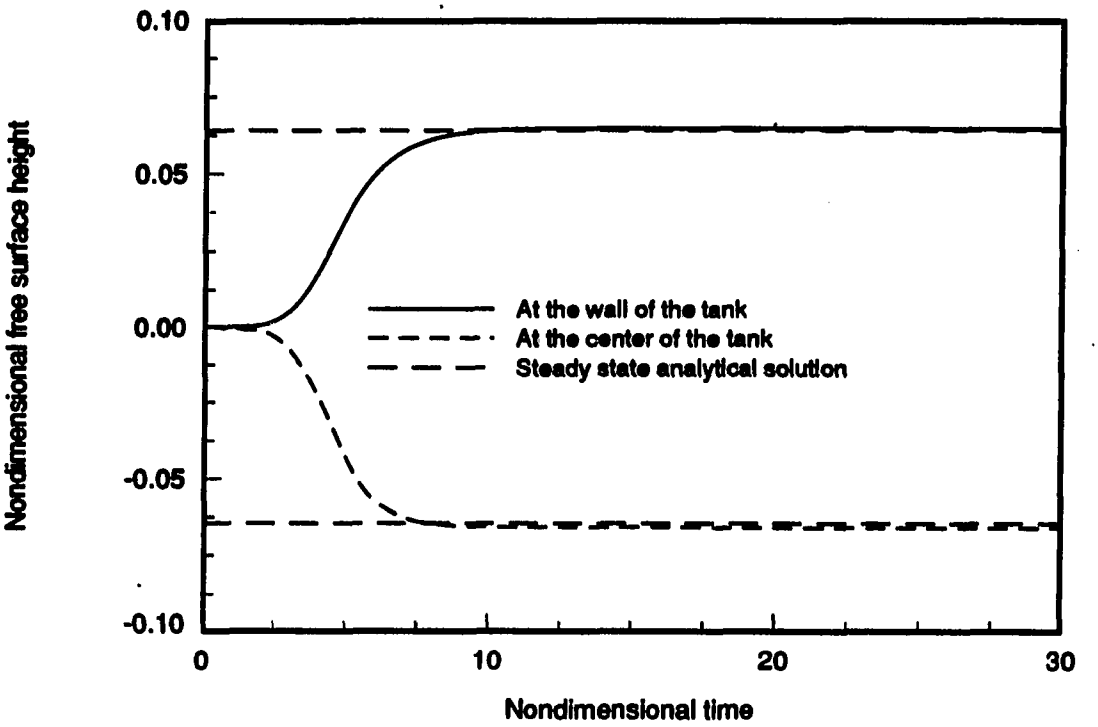

Figure 5.36: The time history of the nondimensional free surface height for the axisymmetric gradual spin-up of a spherical container half filled with glycerin

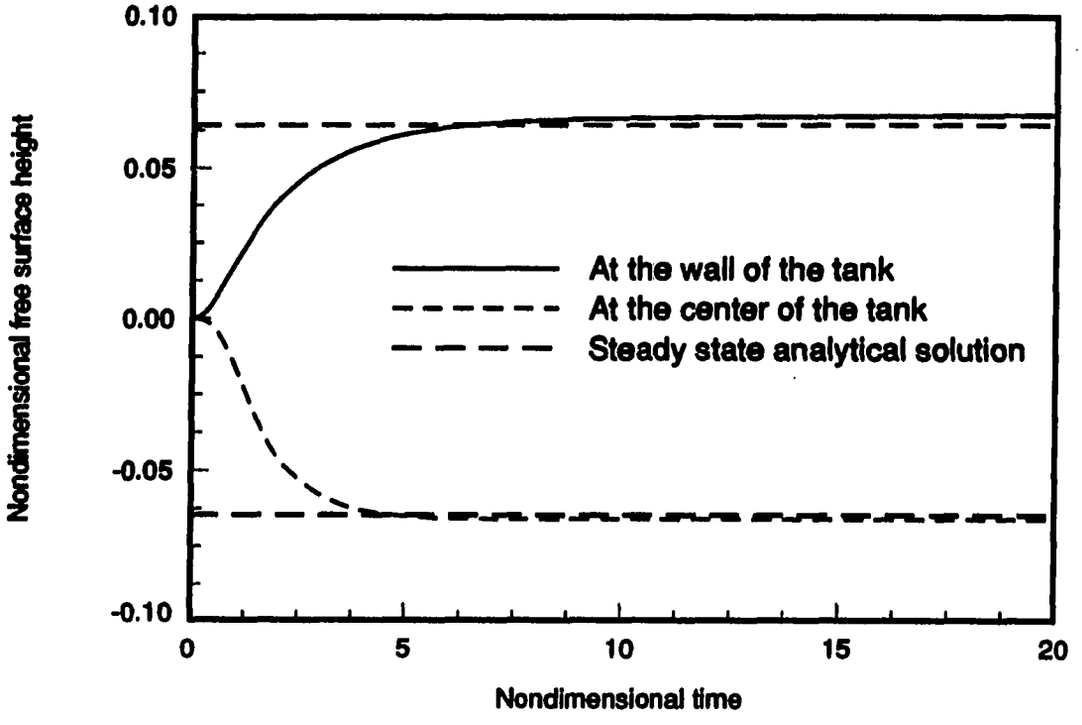

Figure 5.37: The time history of the nondimensional free surface height for the axisymmetric impulsive spin-up of a spherical container half filled with glycerin

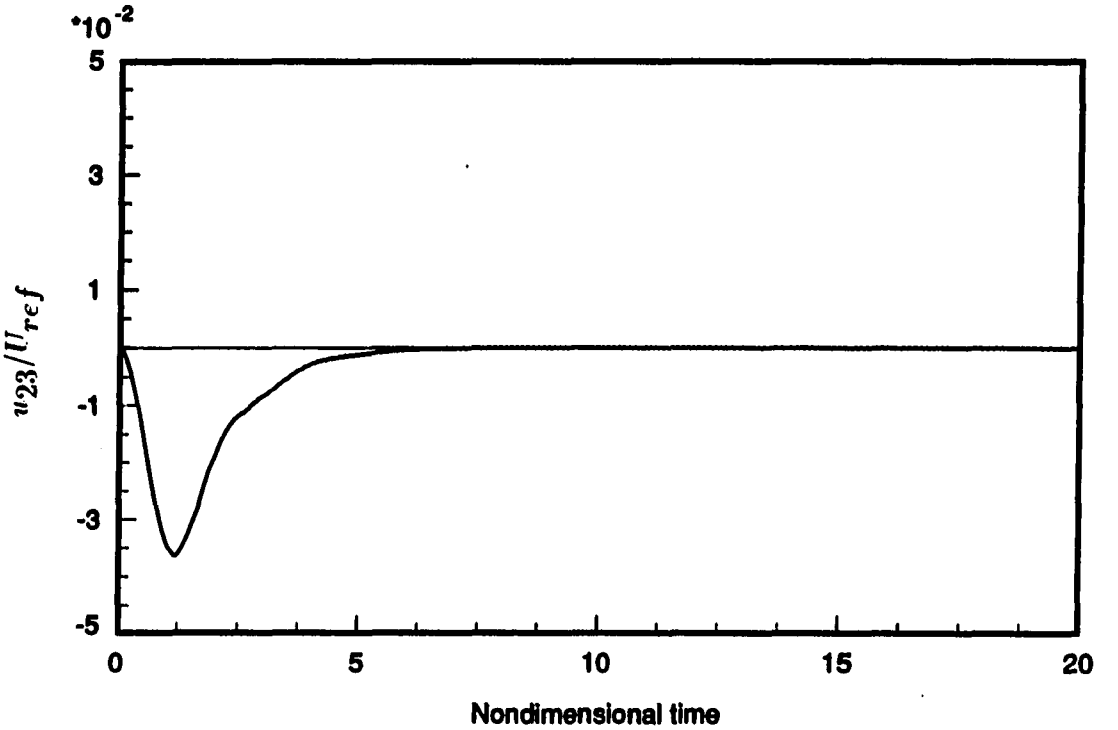

Figure 5.38: The time history of the u_{23} velocity component on the free surface at the center of rotation for the axisymmetric impulsive spin-up of a spherical container half-filled with glycerin

in Fig. 5.38. Again the relative velocity must be zero (shown in the figure) as the solid-body rotation prevails.

5.3.2 Asymmetric spin-up

When the rotation arm, h_i, is nonzero, the solutions will no longer be symmetric. A schematic diagram for this type of spin-up is shown in Fig. 5.39. Two asymmetric cases were computed as a part of the present study with each corresponding to a different rotational speed and rotation arm as listed in Table 5.3. These two cases belong to the initially capped spin-up type as explained in the previous section. The liquid used was glycerin. These two cases are described in the next two sections.

5.3.2.1 Case 1: ω=30 rpm and h_1=12.8 cm The same container as before was half filled again with glycerin. It was initially covered by a cap and rotated in an orbit with a constant rotational speed under the condition of solid-body rotation. At time zero, the cap was removed to allow the liquid surface to move under this spinning condition. The rotational speed was 30 rpm and the rotational arm, h_1 (x_{01} component of h_i), was 12.8 cm which was twice the radius of the container. Based on the above physical quantities, the characteristic nondimensional parameters are:

$Re = 21.9$

$Fr = 0.51$

$We = 207.6$

where the reference velocity, V_{ref}, was based on the rotational speed of the center of the container, i.e., $V_{ref} = \omega h_1$.

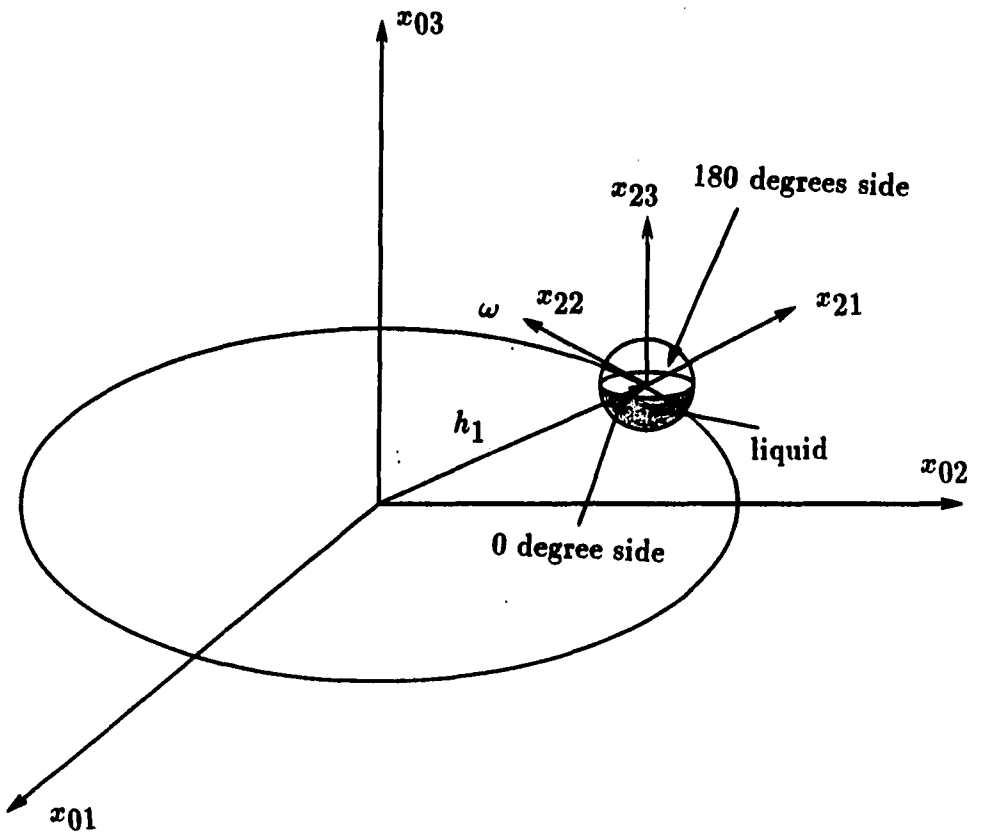

Figure 5.39: Schematic of an asymmetric spin-up container half filled with glycerin

A 41×11×11 grid was used to compute this case with the 41 points being placed in the circumferential direction. A constant nondimensional time step of 0.01 was used for this calculation. At the first time step, 170 subiterations were required for convergence, but the number of subiterations required dropped rapidly and varied between 10 and 15 for most of the calculation. Compared with the previous axisymmetric cases, this calculation was more difficult in two respects. First, the free surface was asymmetric and more grid points were required to resolve the solution in the circumferential direction. The solution would sometimes diverge suddenly if the resolution of the grid was not fine enough or if the grid distribution after the grid adaptation procedure contained a locally sharp slope. This unpleasant grid distribution is more severe near the wall. Second, more computational effort was required to obtain the solution at each time step.

In this calculation, the value of ϕ_τ in the the free surface tracking coordinates was no longer zero. Therefore, the present test case also served as a check for this transformation. For this case, the computation was carried out until the final solid-body steady state solutions were obtained.

In Fig. 5.40 a series of results showing the free surface position at different instants of time are presented. There is no symmetry for this case. The centrifugal force is larger at the right hand side (RHS) (far away from the spin axis) of the tank in Fig. 5.40 than at the left hand side (LHS) (closer to the spin axis). In response to this sudden change, the free surface begins to rise at the RHS and to depress at the LHS from its initial position. The free surface begins to distort and becomes a curved surface as can be seen in Figs. 5.40d-5.40f. It finally becomes a parabolic surface at the new equilibrium position at about $\tau = 7.2$.

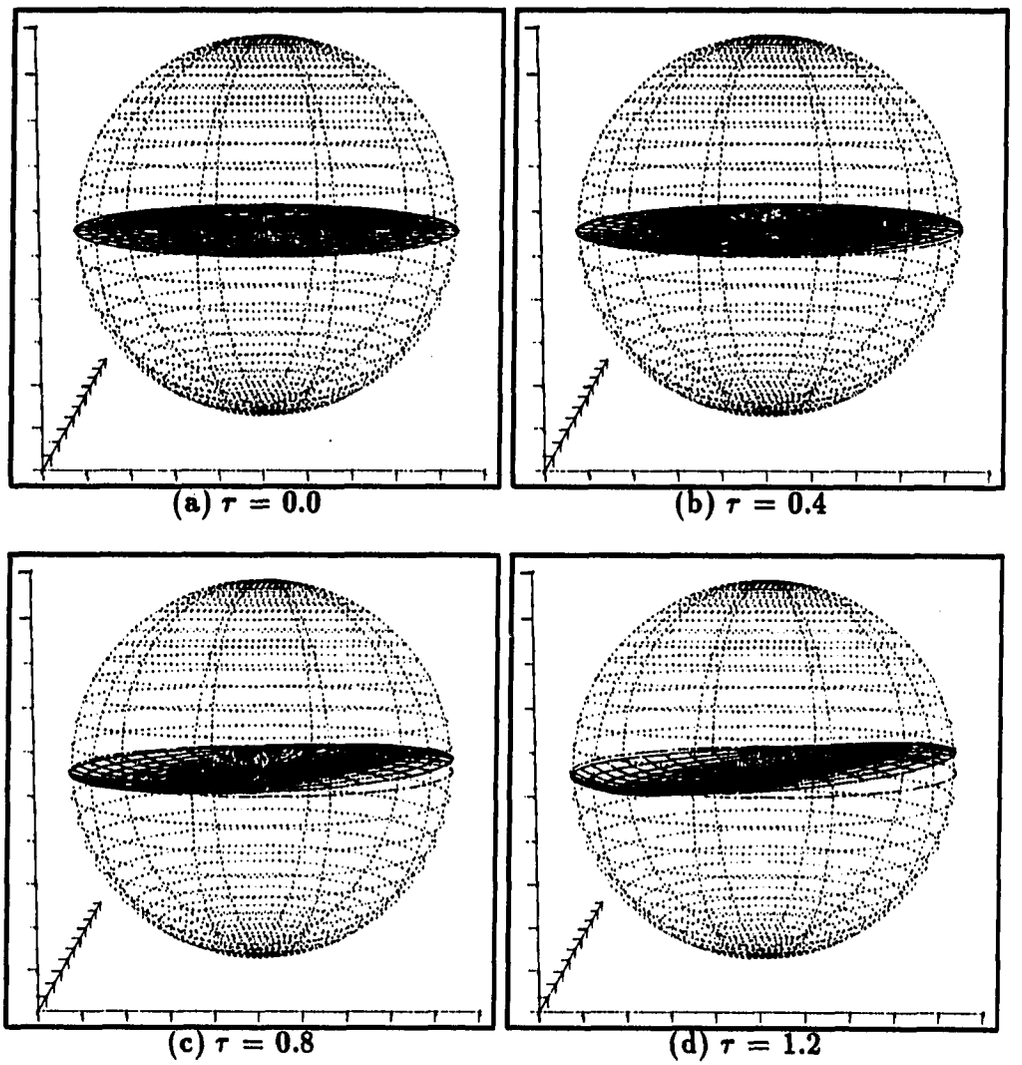

Figure 5.40: Selected free surface plots for the asymmetric initially capped spin-up of a spherical container half filled with glycerin: case 1

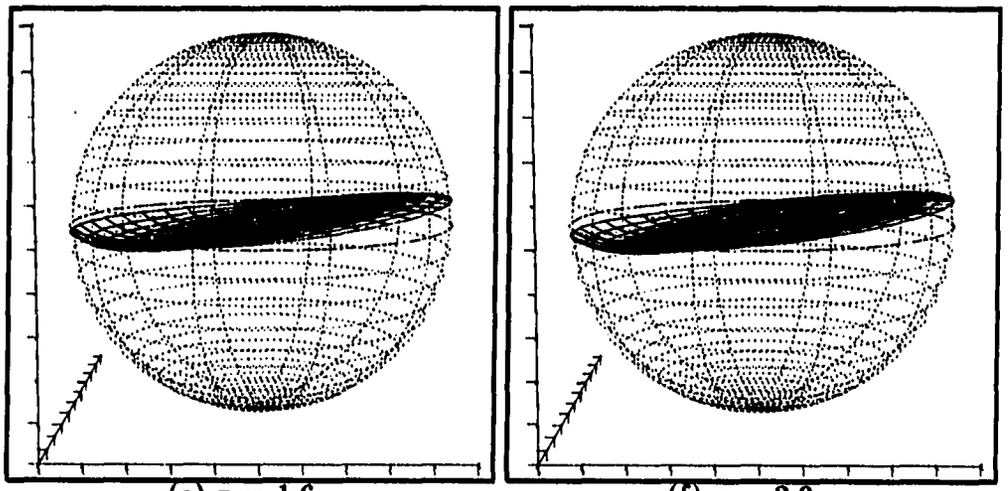

(e) $\tau = 1.6$ (f) $\tau = 2.0$

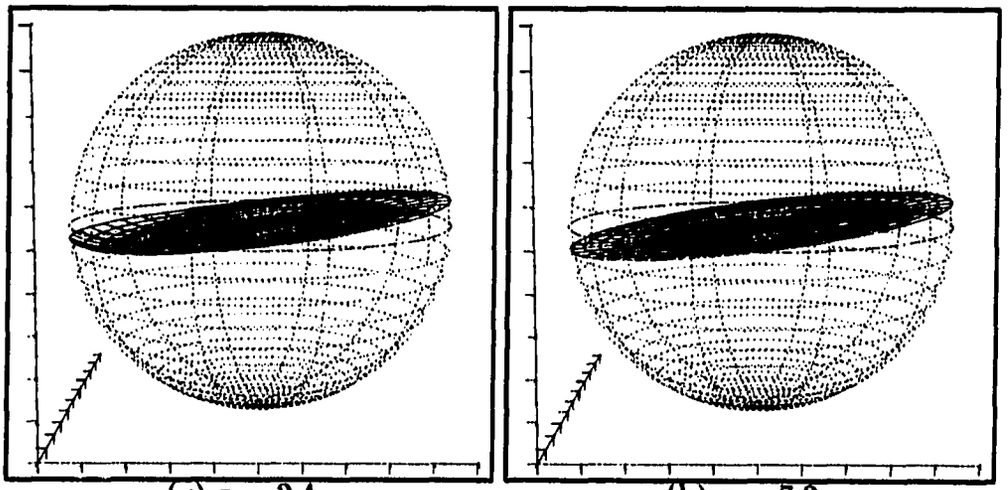

(g) $\tau = 2.4$ (h) $\tau = 7.2$

Figure 5.40: (continued)

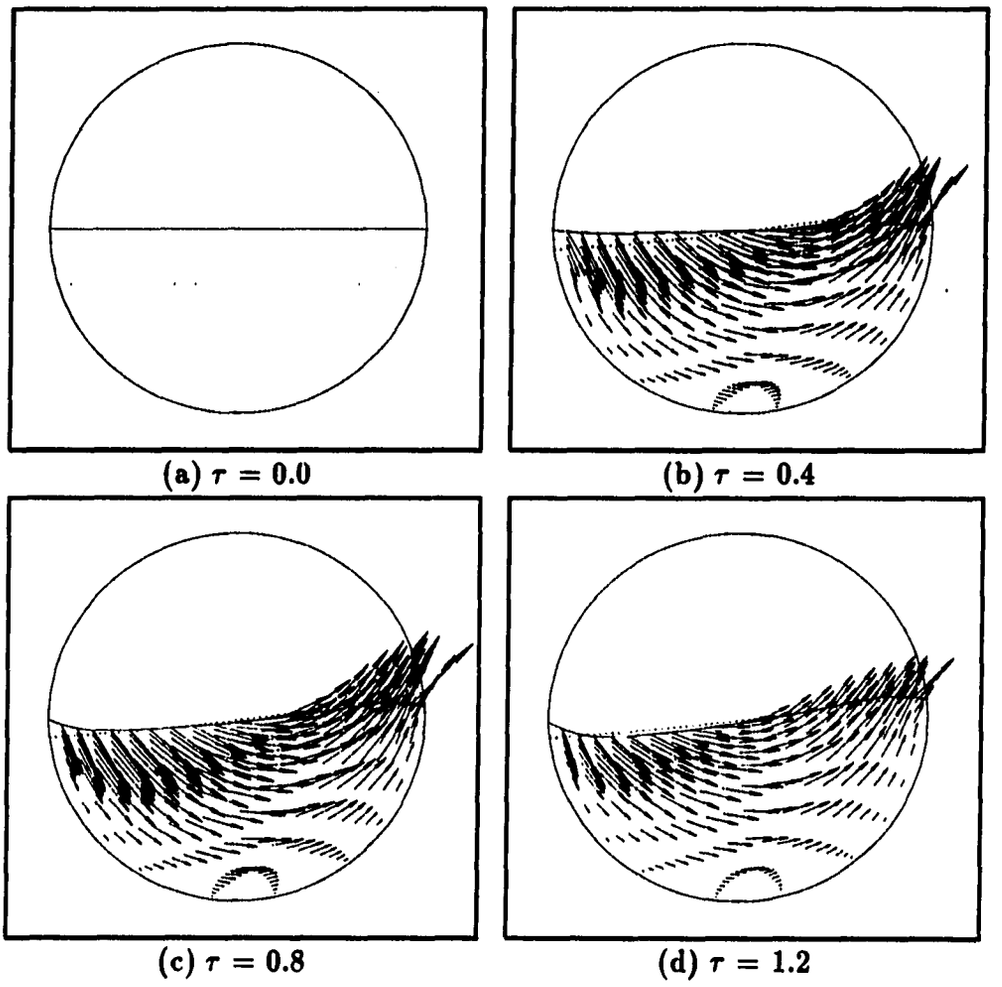

Figure 5.41: Selected velocity vector plots at x_{22}=0 plane for the asymmetric initially capped spin-up of a spherical container half filled with glycerin: case 1 (the dotted line indicates the steady state analytical free surface position)

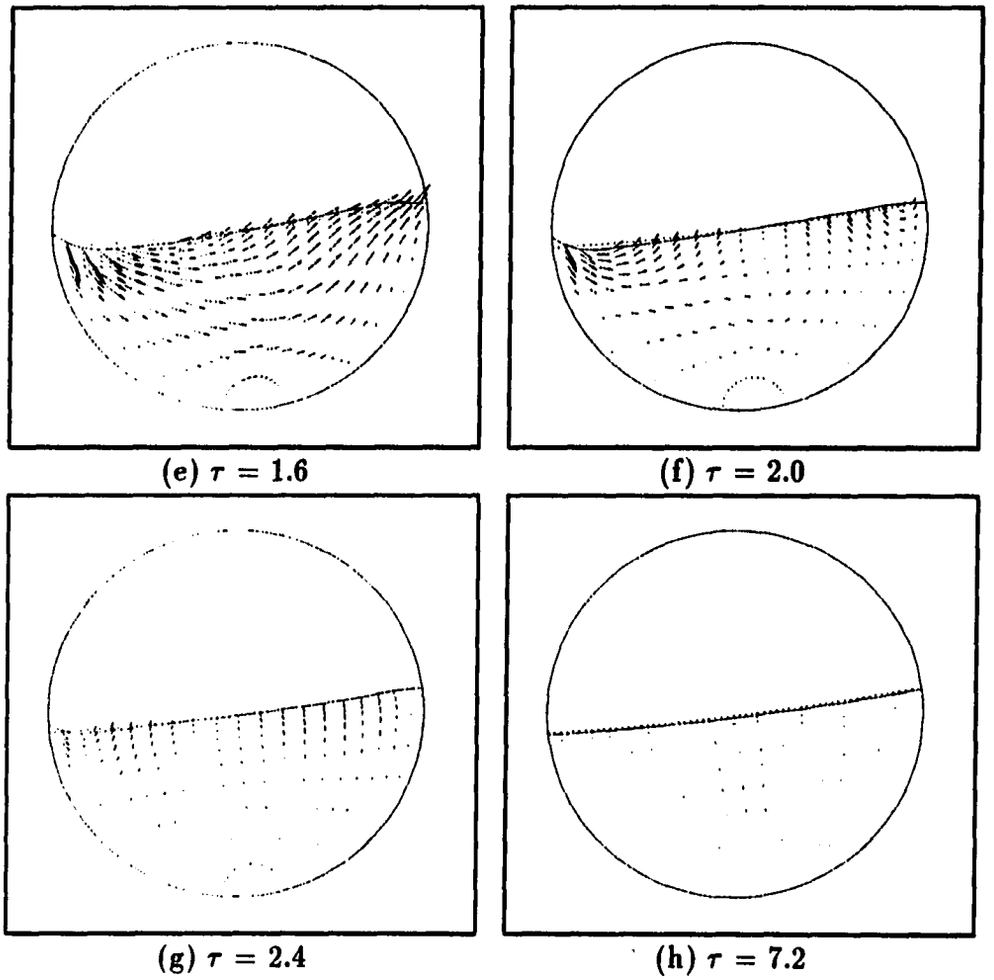

(e) $\tau = 1.6$ (f) $\tau = 2.0$

(g) $\tau = 2.4$ (h) $\tau = 7.2$

Figure 5.41: (continued)

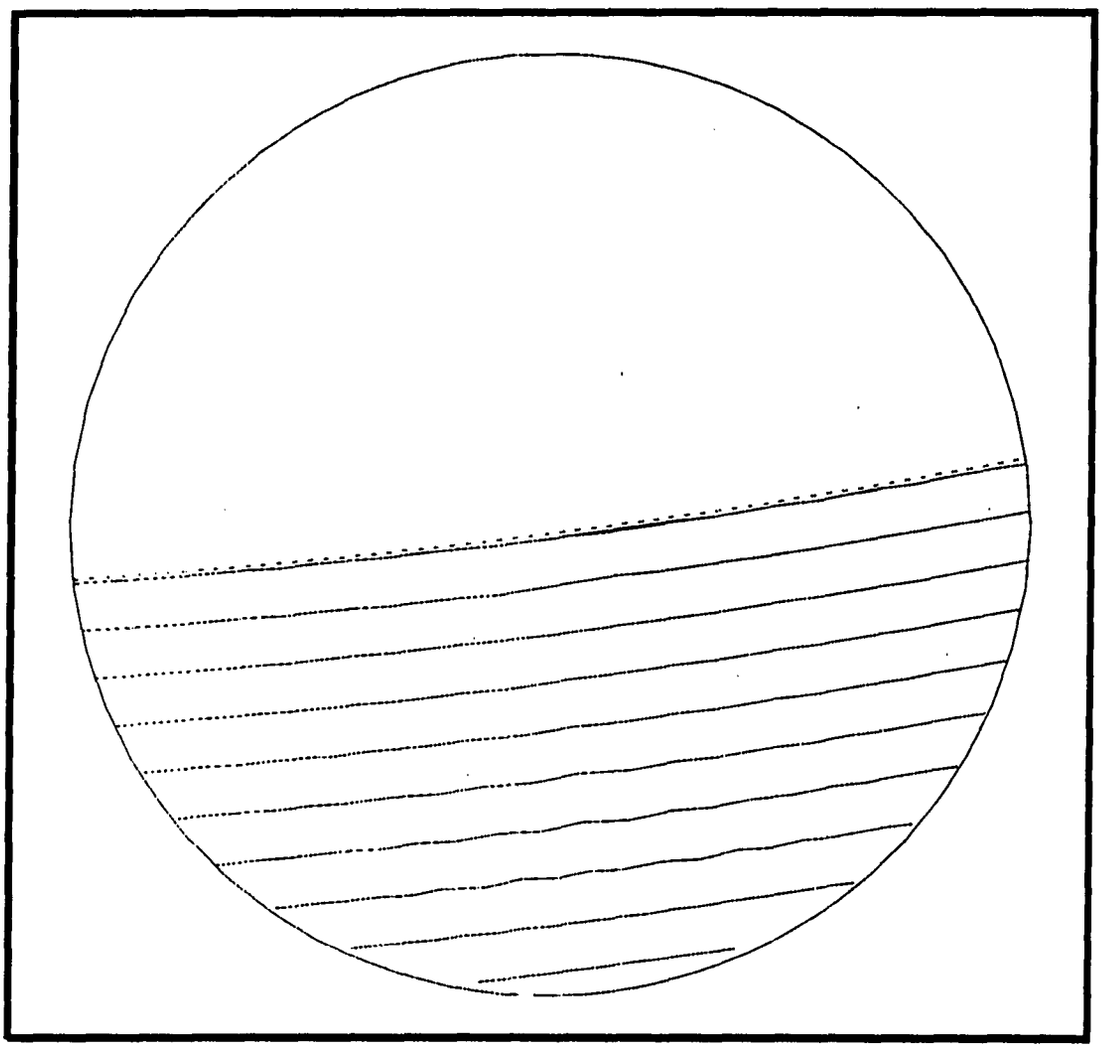

Figure 5.42: Pressure contours for the asymmetric initially capped spin-up of a spherical container half filled with glycerin: case 1 (the dotted line indicates the steady state analytical free surface position)

Some selected velocity vector plots for different times in the x_{22}=0 plane are shown in Fig. 5.41 with the analytical equilibrium free surface position superimposed. The derivation of this analytical solution can be found in Appendix E. The fluid particles were trying to move toward to one side of the tank in response to the combination of the centrifugal and gravitational accelerations. The velocity of the fluid particles was still significant in the early stage of spin-up even near the bottom of the tank. The largest velocity vectors occurred near the free surface and gradually died down. The computation was carried out until the nondimensional time equaled 7.2 at which time solid-body rotation prevailed. The final free surface position can be seen to agree fairly well with the analytical solution. The pressure contours for the final state of solid-body rotation are shown in Fig. 5.42.

Again, the numerical steady state free surface positions at the wall of the container were plotted against the analytical solution. Figure 5.43 shows the time evolution of the free surface position at the wall for positions of 0 (LHS) and 180 (RHS) degrees (see also Fig. 5.39). This plot indicates the free surface rise at the RHS and drop at the LHS from its initial position (equal to zero for half full container). The small discrepancy between the current numerical solution for the free surface position and the analytical solution is probably due to a relatively coarse grid used in this calculation. Further study with a finer grid may help to resolve this discrepancy. Figure 5.44 shows the same evolution but for the rotation angle, ϕ_r, which is the angle used to adjust the free surface tracking coordinates, x_3 coordinates, indicated in Fig. 2.3. It approaches the final analytical solution very closely.

An animation tape based on the above results was made to visualize the liquid sloshing motion for the nondimensional time period between 0 and 4. This calcula-

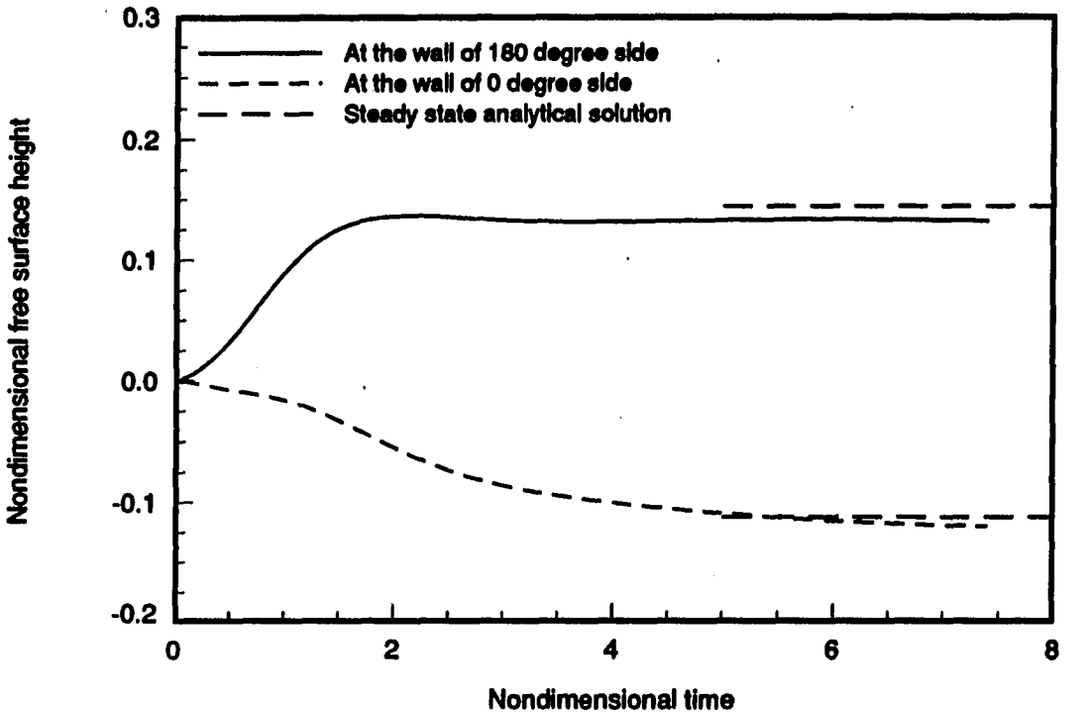

Figure 5.43: The time history of the nondimensional free surface height for the asymmetric initially capped spin-up of a spherical container half filled with glycerin: case 1

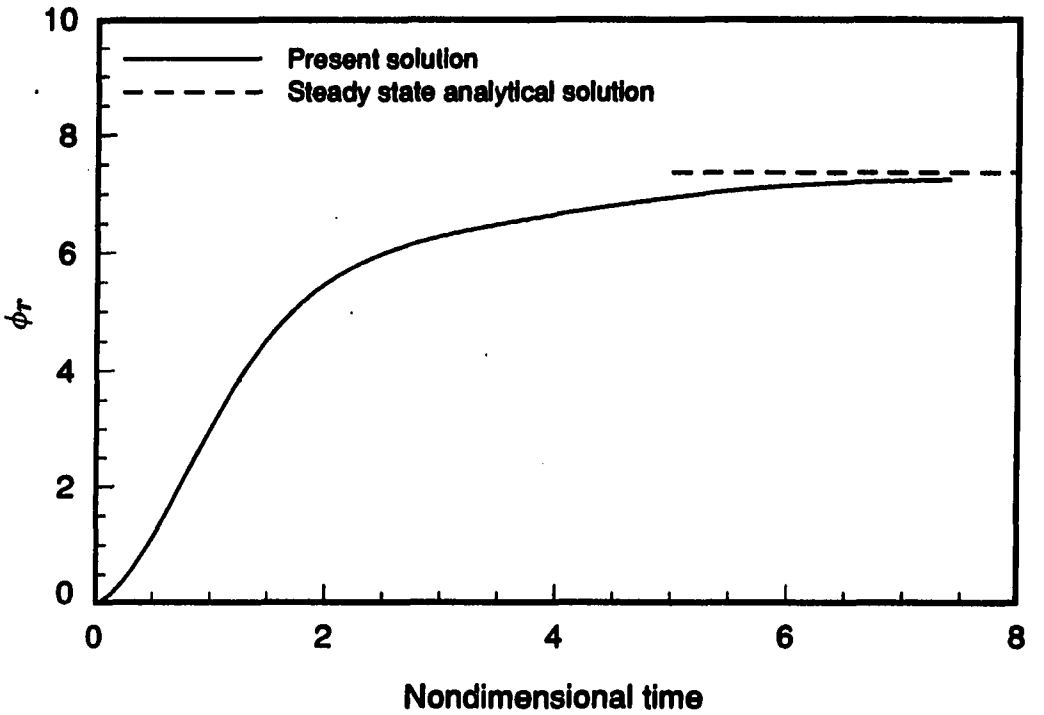

Figure 5.44: The time history of the angle, ϕ_T, for the asymmetric initially capped spin-up of a spherical container half filled with glycerin: case 1

tion took about 22 hours of CPU time on the Apollo DN 10,000 workstation. This animation should contribute toward a better understanding of the liquid sloshing motion in a partially filled container.

5.3.2.2 Case 2: ω=60 rpm and h_1=44.7 cm This is the final test case for the present algorithm in this study, and it represents the most difficult case that has been run by the present author to date. The combination of the high rotational speed and the longer rotation arm in this case creates a centrifugal force which is about 14 times higher than that in the previous case. The radius of the container has been changed to 7.62 centimeters. Based on the above physical quantities, the characteristic nondimensional parameters are:

$$Re = 181.4$$

$$Fr = 3.25$$

$$We = 12002.1$$

where the definitions of the reference quantities are the same as the previous case.

A 51×11×11 grid was used to compute this case with the 51 points being placed in the circumferential direction. A constant nondimensional time step of 0.01 was used for this calculation. Due to the extremely high centrifugal force in this case, the free surface was found to rise (drop) almost to the top (bottom) of the tank during the transient state and the motion of the free surface was more abrupt than that in the previous case. This abrupt free surface motion caused two kinds of numerical difficulties which resulted in the divergence of the solution suddenly after a long calculation time.

First, it was found that the free surface tracking angle, ϕ_r, must be handled very carefully. As described earlier, the purpose of this tracking angle was to facilitate the present grid generation scheme and to keep the free surface height function, F, single-valued. The resulting effect of this tracking angle (and its time rate) was reflected in the governing equations. During the first attempts to compute this case, the free surface (and also ϕ_r) was observed to oscillate in time after nondimensional time, τ=1.8, and the time rate of change in ϕ_r ($\dot{\phi}_r$) began to grow very rapidly. The magnitude of the additional terms (resulting from this ϕ_r rotation) in the governing equations finally became dominant and caused the solution to diverge. In order to reduce this effect, the angle, ϕ_r, used to construct the transformation matrix, S, was obtained by averaging angles from two time levels. This treatment smoothed out the ϕ_r and $\dot{\phi}_r$ and prevented the numerical instability.

Second, it was found that the free surface exhibited a saw-toothed profile locally at about τ=2.6 that began to propagate to neighboring points. This saw-toothed profile created a very unfavorable grid distribution (the interior grids tended to follow the bad grid distribution in the free surface) and resulted in divergence of the solution. Instead of using central differences to represent the spatial derivative terms in the free surface kinematic equation, a first-order upwind difference scheme was used to evaluate those spatial derivative terms. The saw-toothed profile was then removed.

A series of results showing the free surface position at different instants of times are presented in Fig. 5.45. The final solid-body rotation was achieved at about τ=34 which corresponded to about one revolution of rotation. The velocity vectors and pressure contours are shown in Figs. 5.46 and 5.47, respectively. Again, the free surface position at the wall is shown in Fig. 5.48 and the rotation angle is shown

in Fig. 5.49. The number of subiterations at each time step was also recorded and is shown in Fig. 5.50. The sudden increase of subiterations for the nondimensional time between 3 and 5 was due to the oscillation of the free surface angle as described above. For this case the total CPU time was about 58 hours on the Apollo DN 10,000 workstation.

It can be seen in Figs. 5.46 and 5.47 that the steady state free surface position did not match with the analytical solution very well. The volume of the liquid was not conserved. About a 10% discrepancy in volume was estimated. The cause of this mass conservation problem had not been conclusively determined at the time this dissertation was prepared. However, it is suspected that the discrepancy can be attributed to the use of the upwind differencing for the free surface kinematic equation. This point is currently under study.

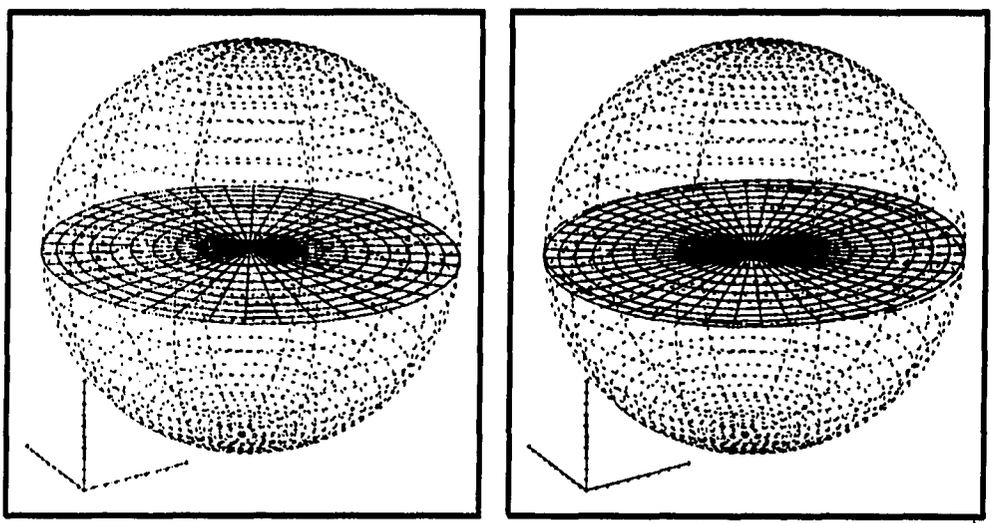

(a) $\tau = 0.0$ (b) $\tau = 0.9$

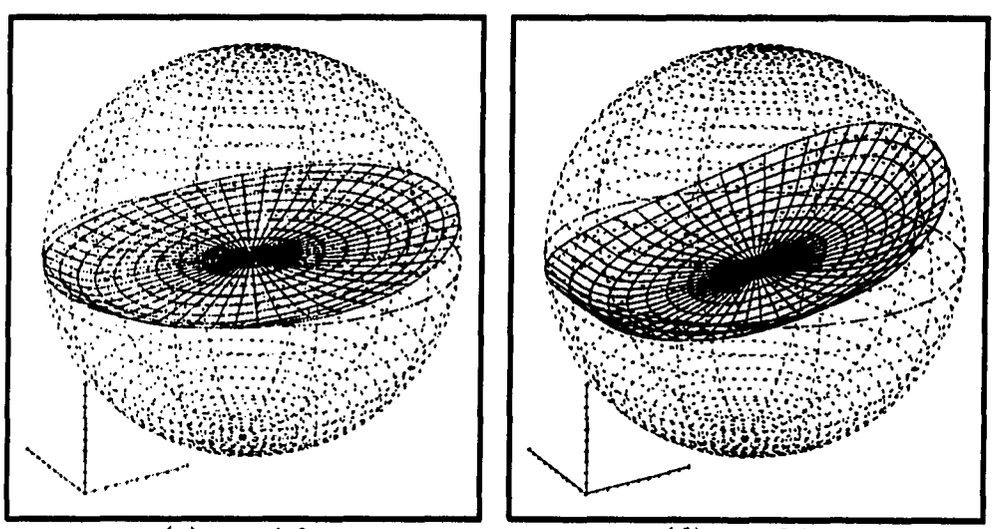

(c) $\tau = 1.8$ (d) $\tau = 2.7$

Figure 5.45: Selected free surface plots for the asymmetric initially capped spin-up of a spherical container half filled with glycerin: case 2

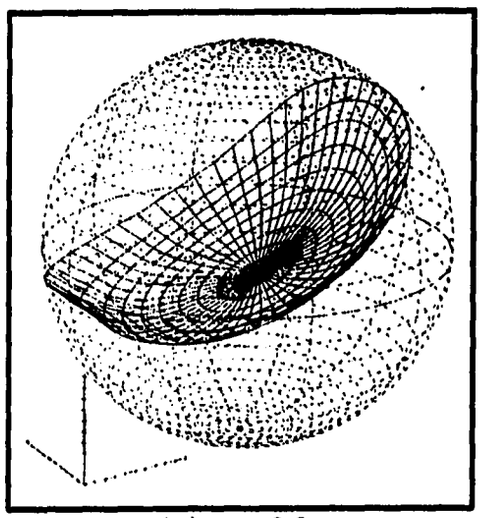

(a) $\tau = 3.6$

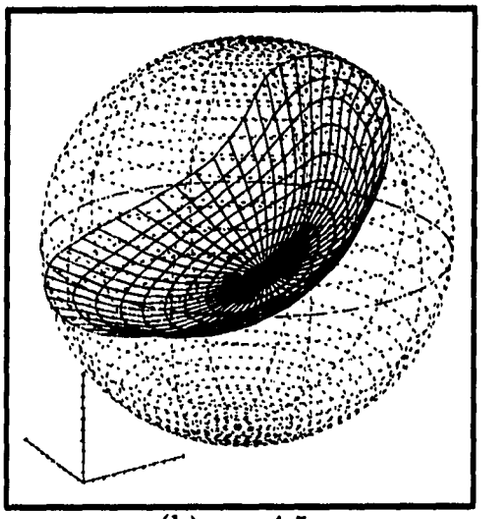

(b) $\tau = 4.5$

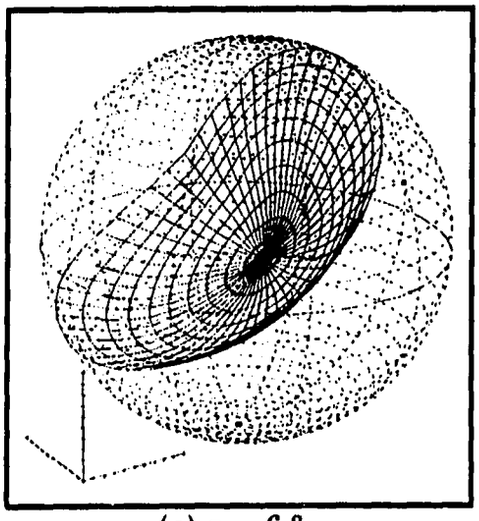

(c) $\tau = 6.3$

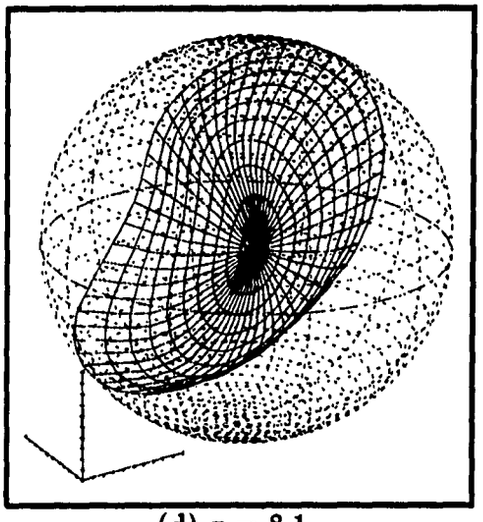

(d) $\tau = 8.1$

Figure 5.45: (continued)

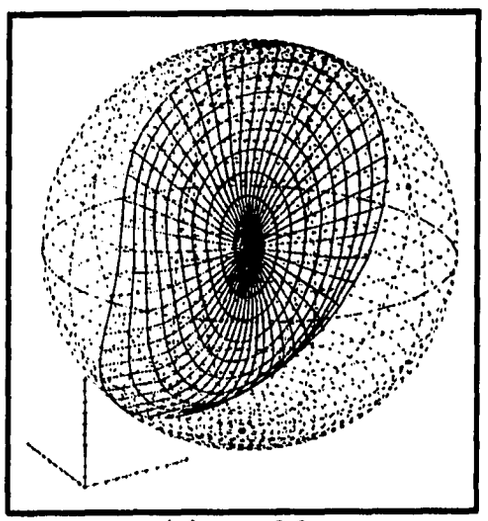

(a) $\tau = 9.9$

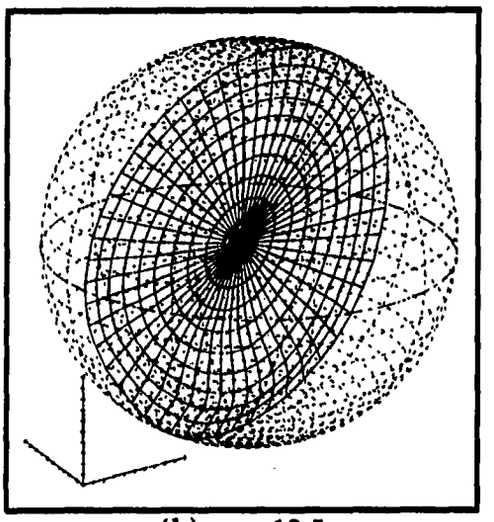

(b) $\tau = 13.5$

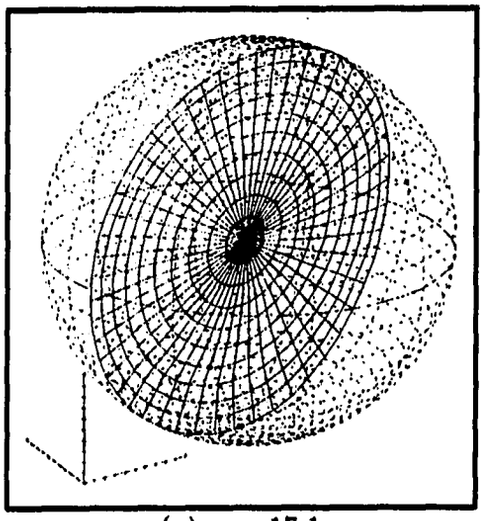

(c) $\tau = 17.1$

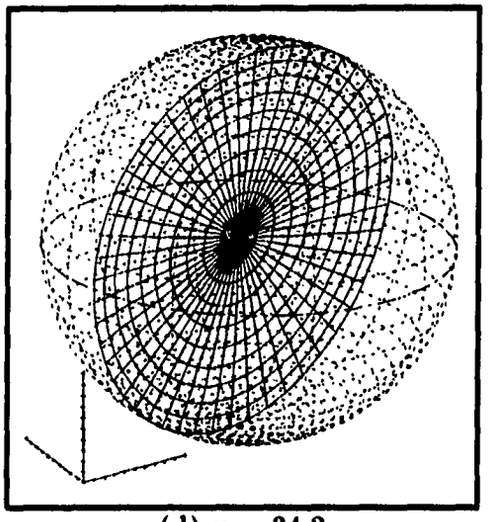

(d) $\tau = 34.2$

Figure 5.45: (continued)

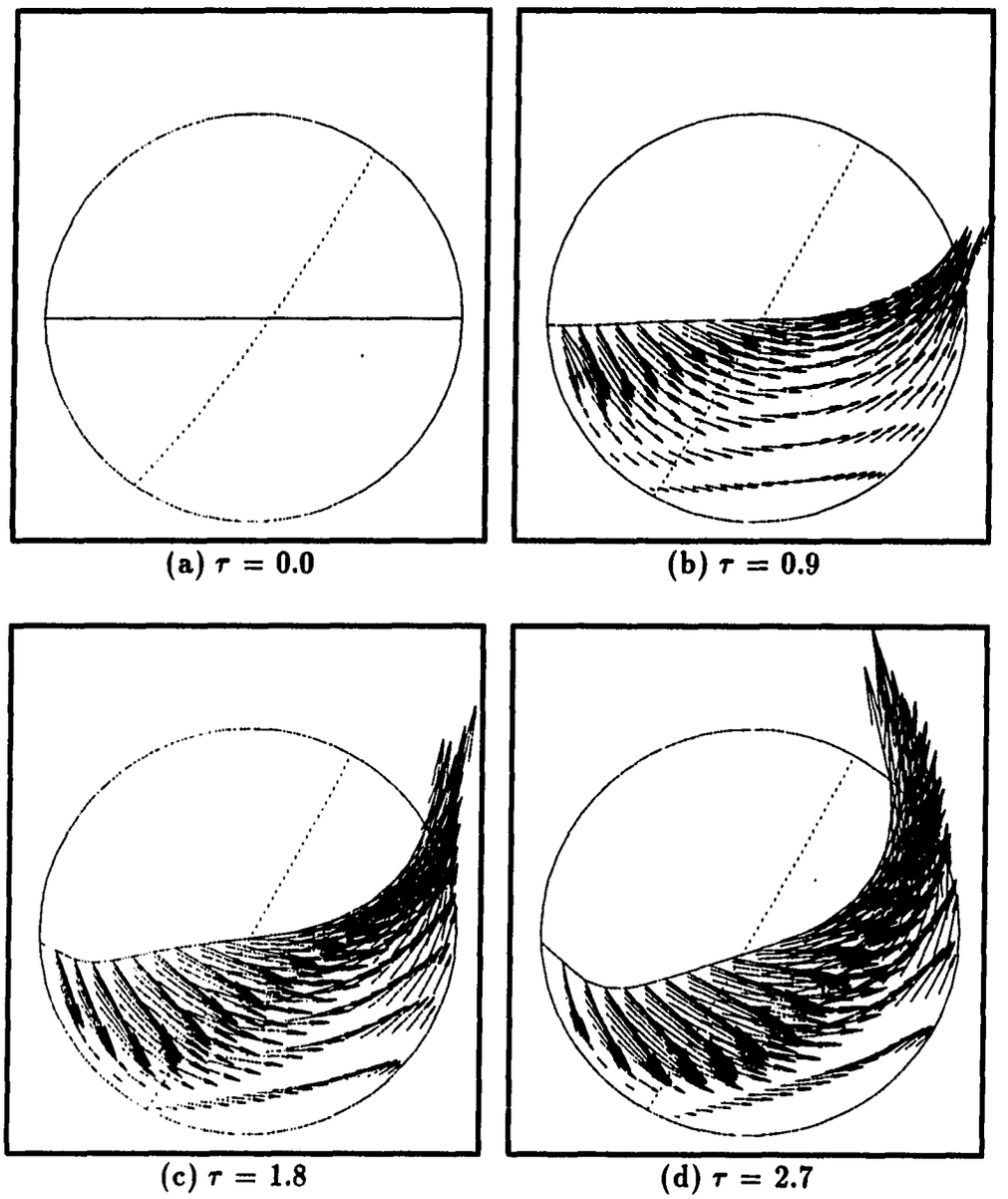

Figure 5.46: Selected velocity vector plots at x_{22}=0 plane for the asymmetric initially capped spin-up of a spherical container half filled with glycerin: case 2 (the dotted line indicates the steady state analytical free surface position)

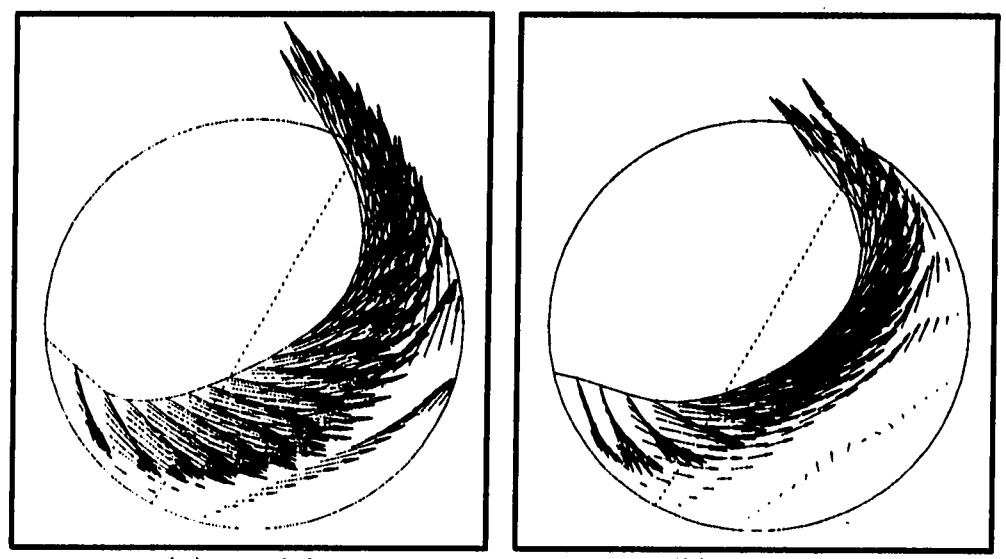

(a) $\tau = 3.6$ (b) $\tau = 4.5$

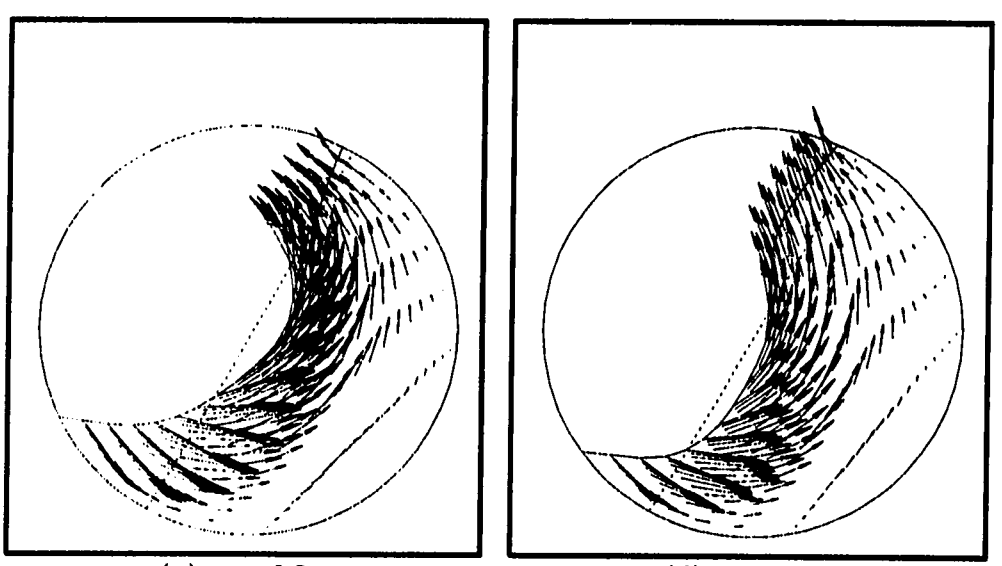

(c) $\tau = 6.3$ (d) $\tau = 8.1$

Figure 5.46: (continued)

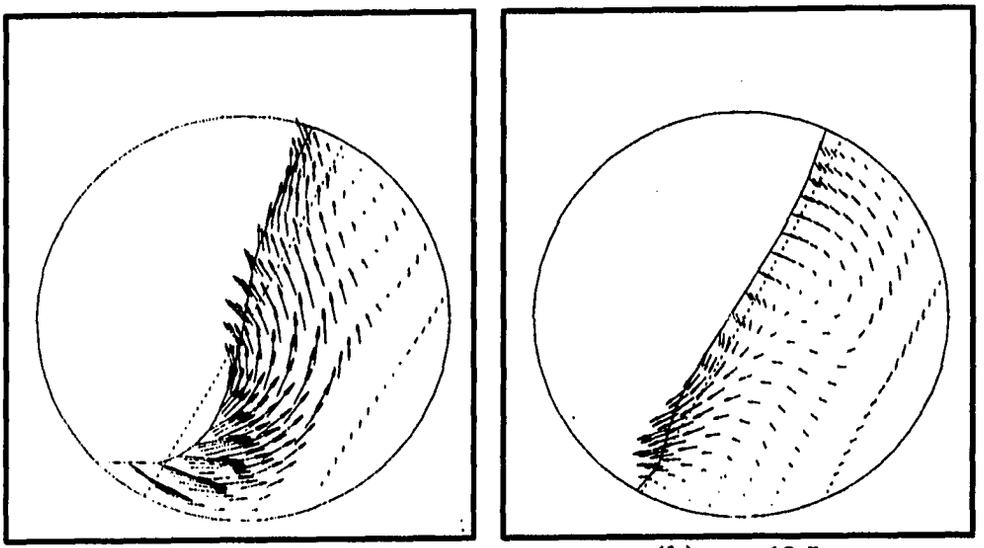

(a) $\tau = 9.9$ (b) $\tau = 13.5$

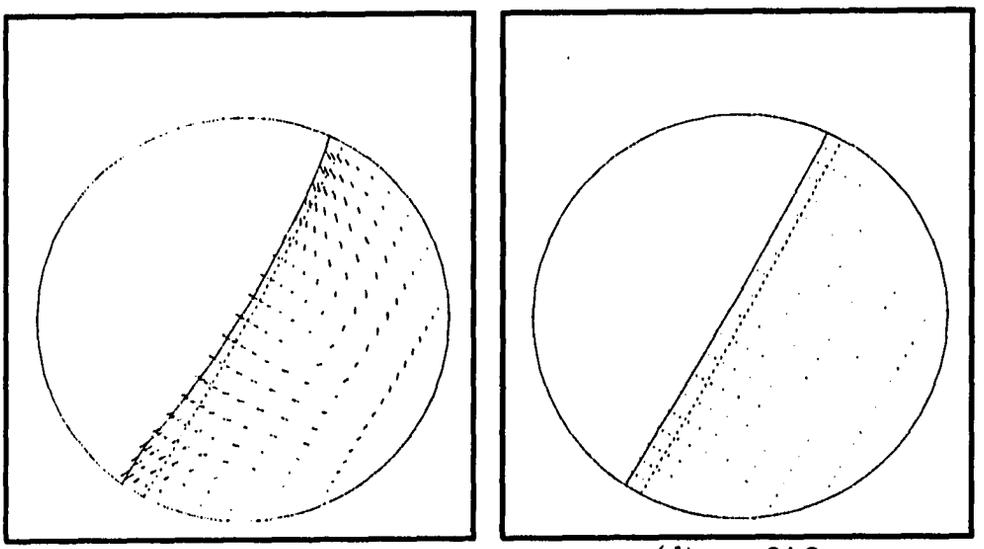

(c) $\tau = 17.1$ (d) $\tau = 34.2$

Figure 5.46: (continued)

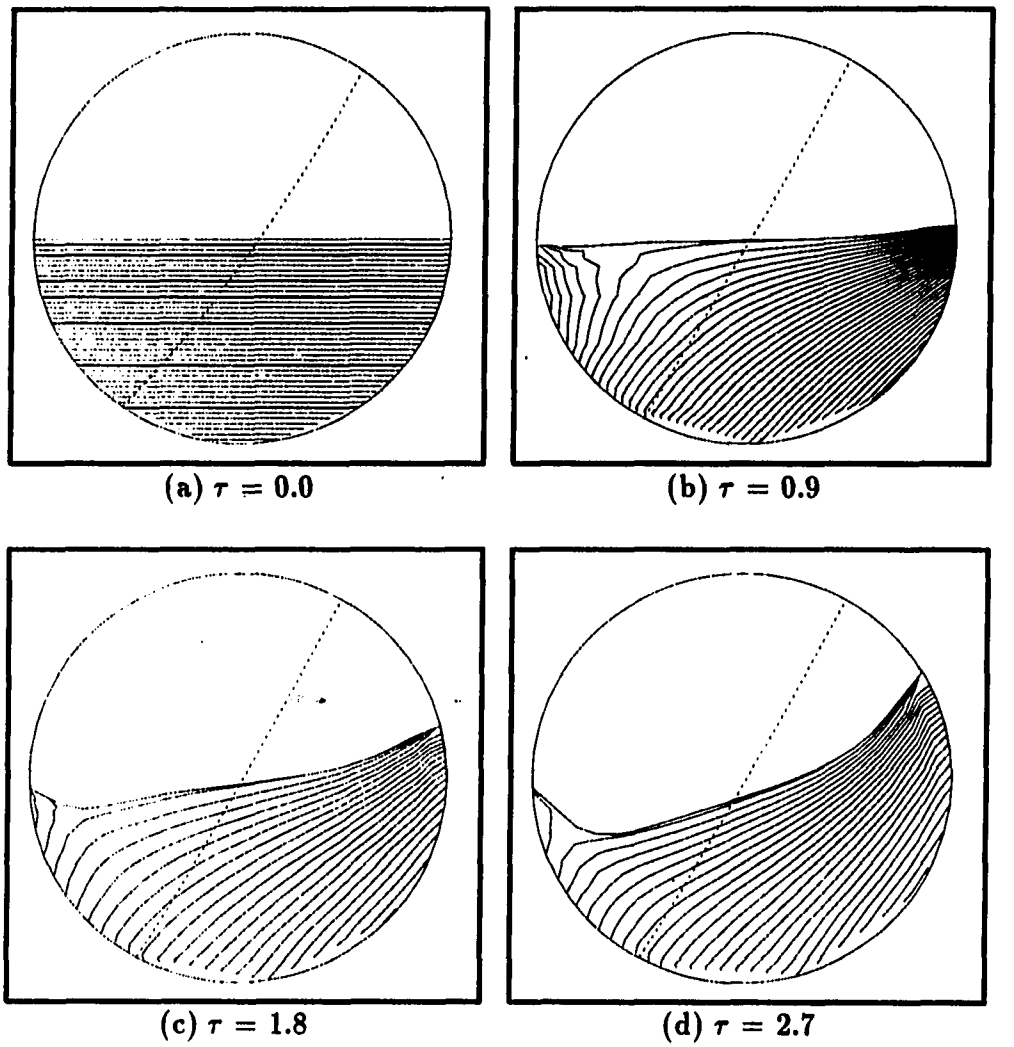

Figure 5.47: Selected pressure contour plots at x_{22}=0 plane for the asymmetric initially capped spin-up of a spherical container half filled with glycerin: case 2 (the dotted line indicates the steady state analytical free surface position)

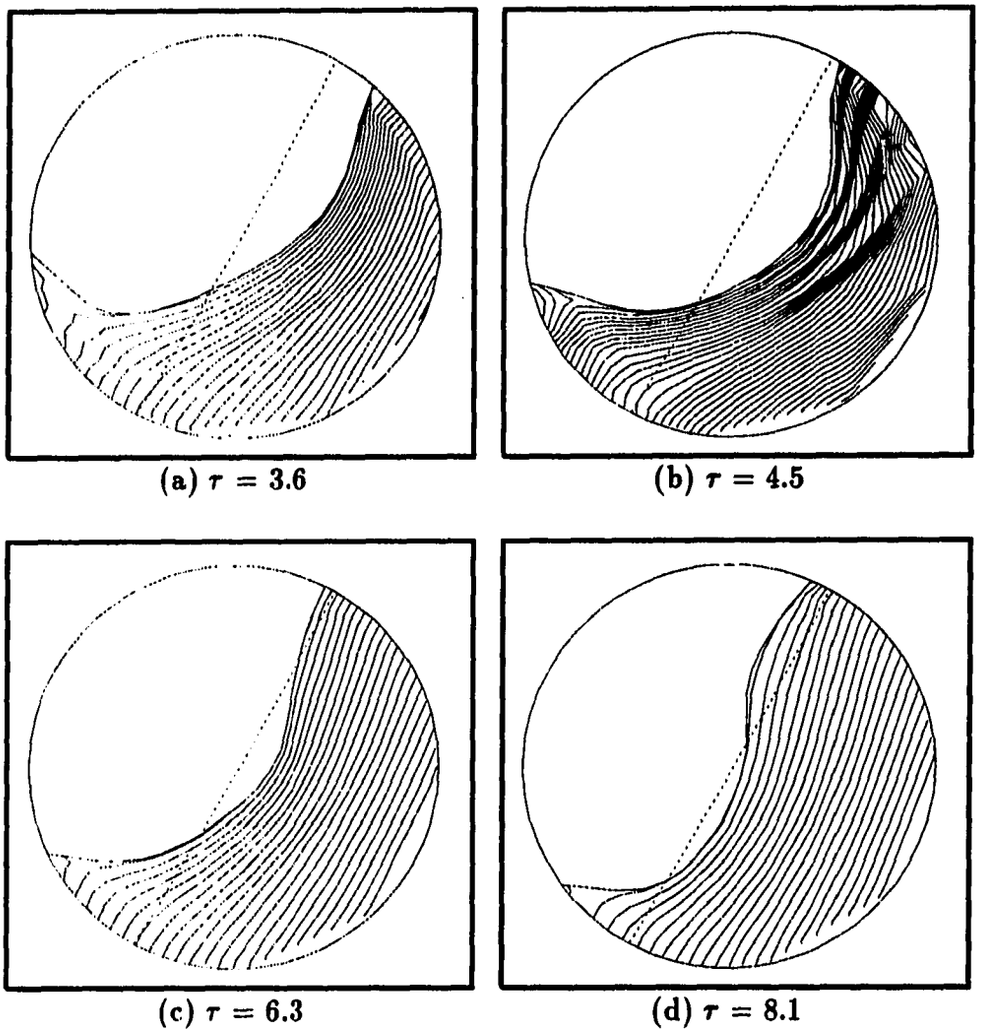

(a) $\tau = 3.6$ (b) $\tau = 4.5$

(c) $\tau = 6.3$ (d) $\tau = 8.1$

Figure 5.47: (continued)

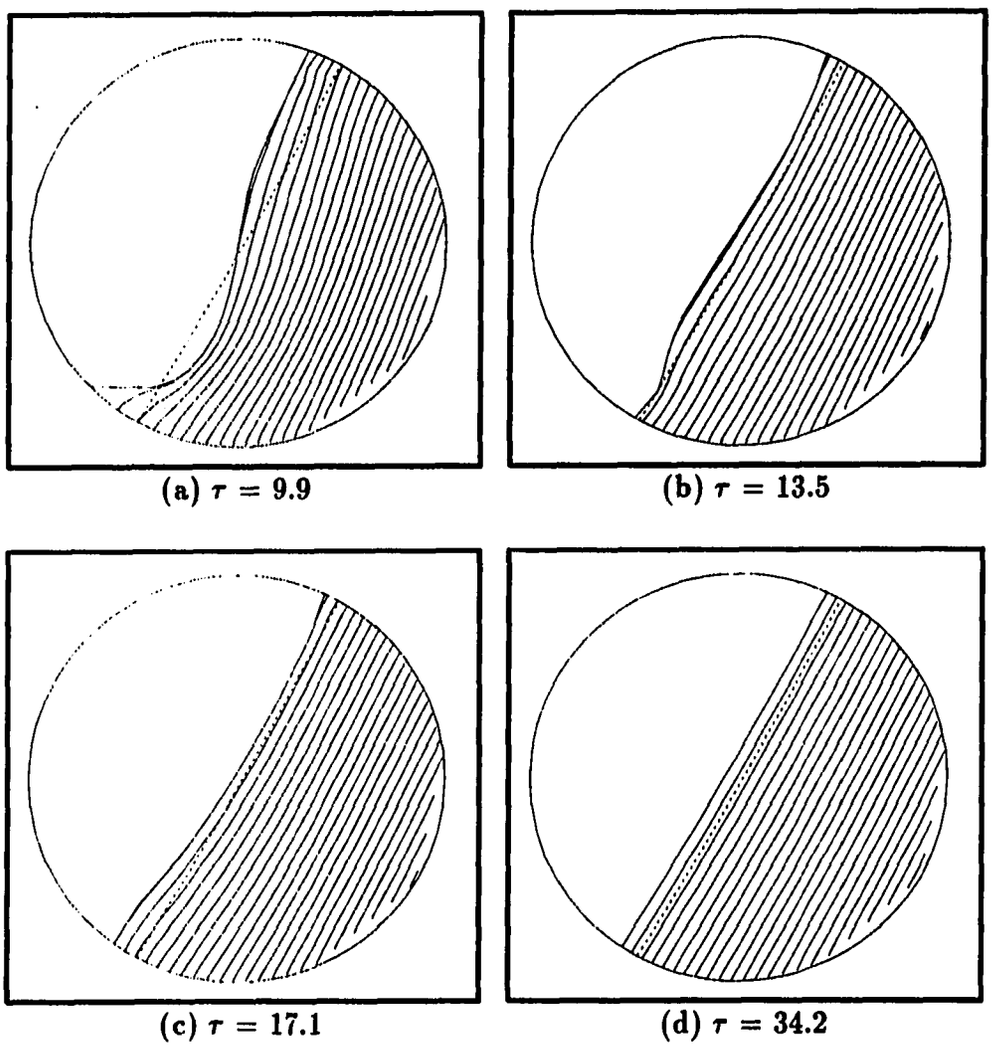

(a) $\tau = 9.9$ (b) $\tau = 13.5$

(c) $\tau = 17.1$ (d) $\tau = 34.2$

Figure 5.47: (continued)

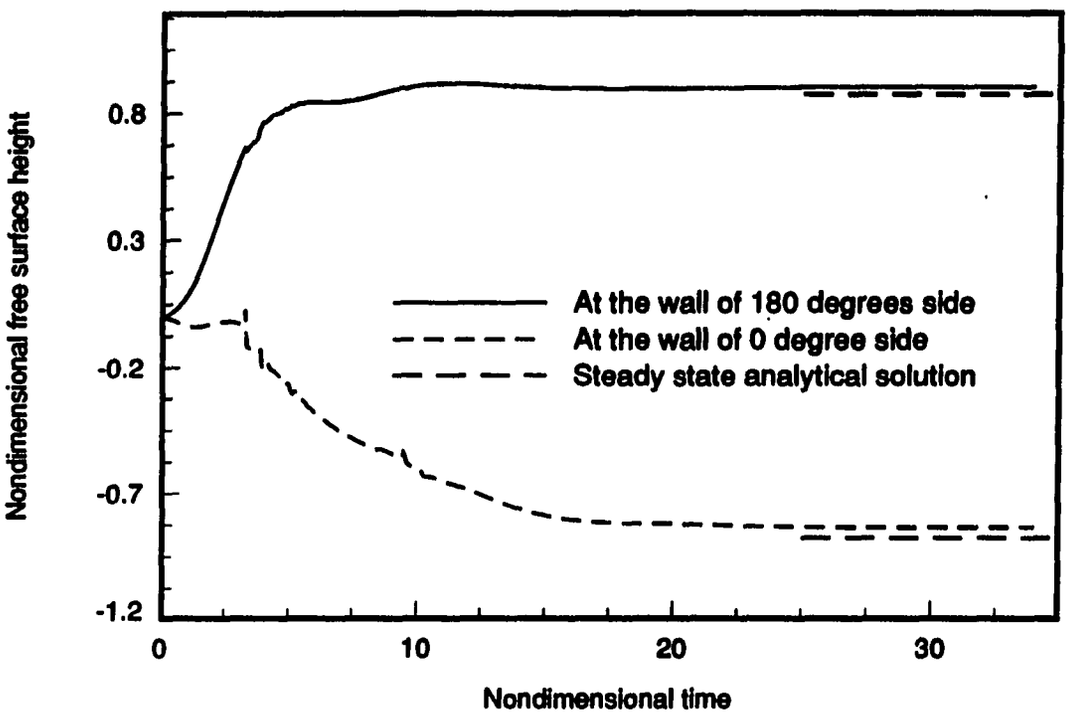

Figure 5.48: The time history of the nondimensional free surface height for the asymmetric initially capped spin-up of a spherical container half filled with glycerin: case 2

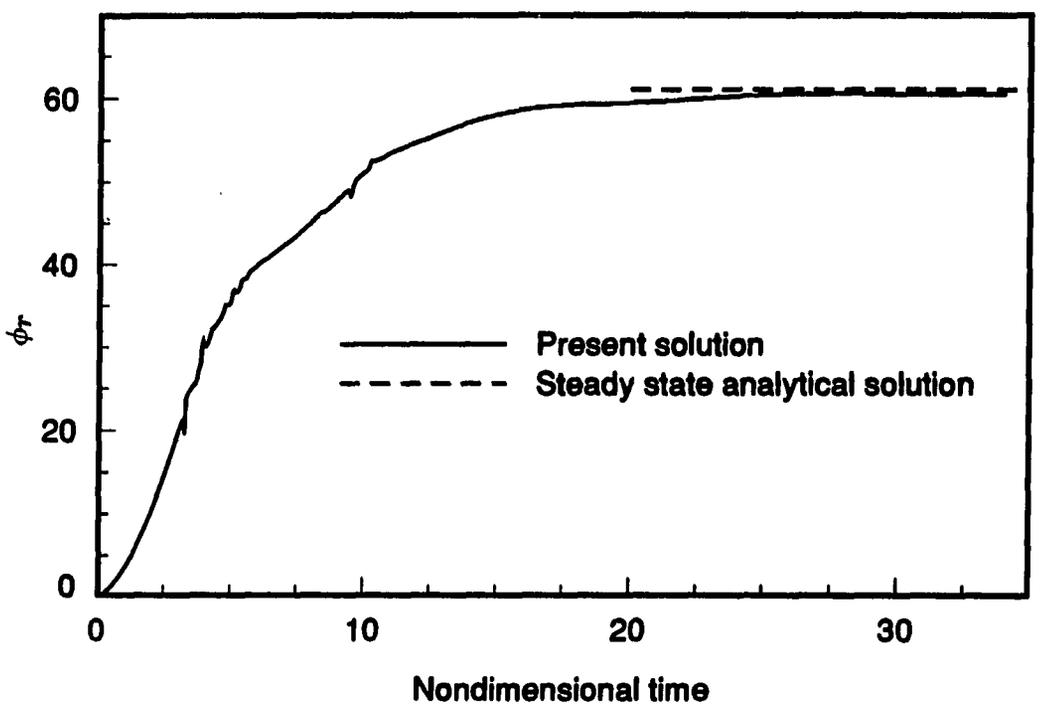

Figure 5.49: The time history of the angle, ϕ_T, for the asymmetric initially capped spin-up of a spherical container half filled with glycerin: case 2

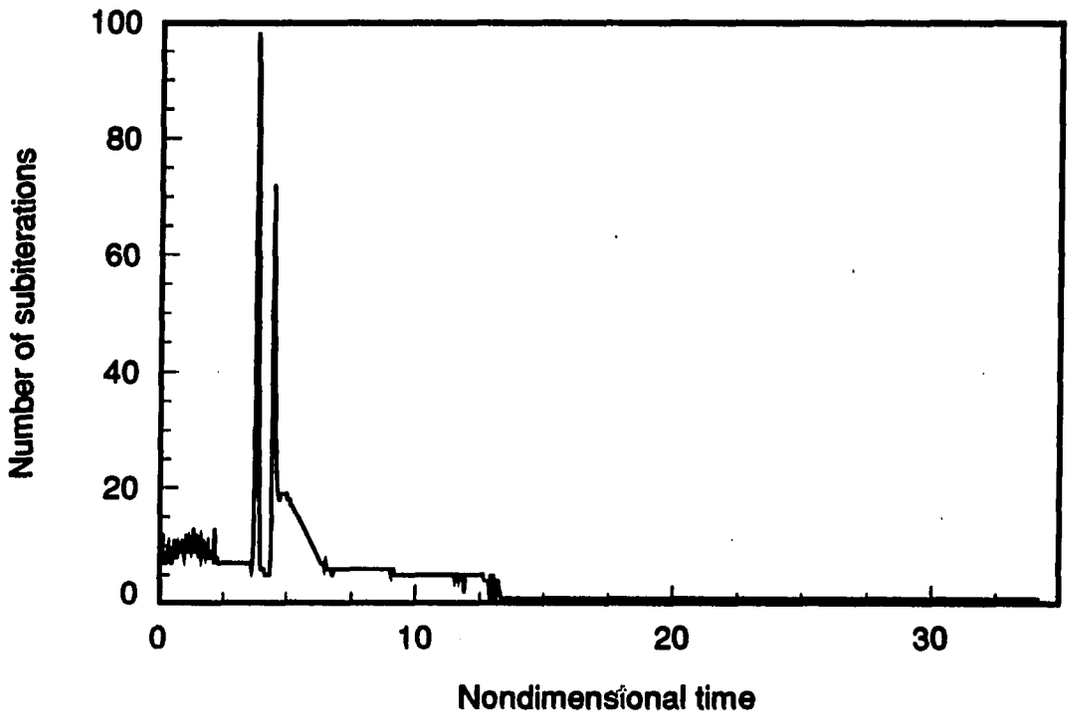

Figure 5.50: The time history of the number of subiterations at each time step for the asymmetric initially capped spin-up of a spherical container half filled with glycerin: case 2

6. CONCLUDING REMARKS

6.1 Conclusions

A coupled solution strategy for the time-dependent two and three-dimensional Navier-Stokes equations was developed. Both compressible and incompressible flows have been considered. The present solution algorithm was also applied to solve flows with free surfaces.

It appears that this algorithm for solving the two-dimensional compressible form of the Navier-Stokes equations is effective for Mach numbers ranging from the incompressible limit ($M_\infty \sim 0.01$) to supersonic. The approach employs the strong conservation law form of the governing equations but uses primitive (u, v, p, T) variables rather than the more traditional conserved (ρ, ρu, ρv, E_t) variables as unknowns. This choice of variables simplifies the treatment of viscous terms and enhances effectiveness at low Mach numbers by allowing the density to be removed from the difference equations. A coupled modified strongly implicit procedure was used to efficiently solve the Newton-linearized algebraic equations. Generally, it was found that smoothing was not needed to control spatial oscillations in pressure for subsonic flows despite the use of central differences. Dual time stepping was found to further accelerate convergence for steady flows. Generally good agreement between the predictions and results in the literature was observed for several test cases includ-

ing steady and unsteady low Mach number internal and external flows and a steady shock-boundary layer interaction flow on a flat plate in a supersonic stream.

For three-dimensional liquid sloshing flows, the solution strategy for the two-dimensional compressible equations coupled with the artificial compressibilty method forms a unified solution algorithm which solves for the primitive variables in a coupled manner. The pressure Poisson equation was not required in this procedure; instead, the continuity equation was directly coupled with the momentum equations and the pressure information was obtained along with the velocity field directly. This avoids the complexity of deriving and solving the pressure Poisson equation for the complicated three-dimensional problem encountered in this study. It appears that this procedure can handle the three-dimensional unsteady flows very efficiently (with only a few subiterations needed for most of the time steps) even in the presence of a free surface which requires that the flow field be computed in a new domain at every time step. Six different kinds of spin-up problems have been computed with this algorithm in three-dimensional configurations, including two axisymmetric initially capped spin-up cases with glycerin and kerosene, one axisymmetric gradual spin-up case with glycerin, one axisymmetric impulsive spin-up case with glycerin and two asymmetric initially capped spin-up cases with glycerin under different rotational conditions.

The SIP method demonstrated very good convergence properties for solving the algebraic system of equations. Its strongly implicit nature provides a faster convergence rate and enhances the robustness of the present algorithm. However, despite the positive features of this method, a large amount of storage is required, especially for a three-dimensional block matrix system. Whether the storage disadvantage will

offset its favorable convergence property and robustness depends on the availability of computer storage. According to the present author's experience on the Apollo DN 10,000 workstation, SIP is a very suitable candidate for solving a coupled system in two dimensions with a reasonably dense grid; however, for a three-dimensional coupled system, it required considerable amount of computer memory even with a moderate grid (say 41×41×41). Such storage requirements are expected to be less of a problem in the future since the trend is toward providing larger and larger memory capability for computers.

6.2 Recommendations for Future Research

Although the present solution algorithm has been shown to be capable of handling different types of two and three-dimensional flow problems, several areas still deserve further study. They are described as follows.

1. The pressure smoothing capability of the centrally-differenced compressible form of the Navier-Stokes equations for low Mach number nearly incompressible flows deserves further investigation. In the present study, the success of the pressure smoothing was only demonstrated for two and three-dimensional cavity flows. The same procedure should be tested for incompressible flow problems with different geometries in order to further evaluate the success of this concept.

2. The extension of the present algorithm to an upwind scheme would be desirable in the future. The problem related to the slow convergence for the high Reynolds number cases in the two-dimensional compressible calculations may

be due to the use of the central differences. A type of upwind scheme similar to that described in the work by Pan and Chakravarthy [21] would be a candidate for extension to the present scheme.

3. The cases presented in this study for the three-dimensional liquid sloshing simulation were obtained with a relative coarse grid. Finer grid results are definitely desirable.

4. The mass conservation problem arising in some of the three-dimensional calculations deserves further study.

5. In this study, only laminar flows were considered. The implementation of turbulence modeling would allow the present scheme to compute turbulent flows. This extension is nontrivial, and would provide a challenging task in the future.

6. Vectorization of the present algorithm, especially for the SIP recursive formula, will greatly increase the efficiency of the present algorithm on vector machines.

7. BIBLIOGRAPHY

[1] Miyata, H. "Finite-Difference Simulation of Breaking Waves." *Journal of Computational Physics*, 65, 179-214, 1986.

[2] Miyata, H., Sato, T. and Baba, N. "Difference Solution of a Viscous Flow with Free-Surface Wave about an Advancing Ship." *Journal of Computational Physics*, 72, 393-421, 1987.

[3] Hirt, C. W. and Shannon, J. P. "Free Surface Stress Conditions for Incompressible-Flow Calculations." *Journal of Computational Physics*, 2, 403-411, 1968.

[4] Meakin, R. and Suhs, N. "Unsteady Aerodynamic Simulation of Multiple Bodies in Relative Motion." AIAA 89-1996, 1989.

[5] Meakin, R. "Overset Grid Methods for Aerodynamic Simulation of Bodies in Relative Motion." To be presented at 8th Aircraft/stores compatibility symposium, Ramada Beach Resort, Fort Walton Beach, Florida, 23-25 Oct. 1990.

[6] Chiu, I. T. *On Computations of the Integrated Space Shuttle Flowfield Using Overset Grids.* Ph.D. Dissertation. Iowa State University, Ames, Iowa, 1990.

[7] Anderson, D. A., Tannehill, J. C., and Pletcher, R. H. *Computational Fluid Mechanics and Heat Transfer.* McGraw-Hill Book Co., New York, 1984.

[8] Beam, R. M. and Warming, R. F. "An Implicit Factored Scheme for the Compressible Navier-Stokes Equations." *AIAA Journal*, 16, No. 4, 393-402, 1978.

[9] Liou, M.-S. "Newton/Upwind Method and Numerical Study of Shock Wave/Boundary Layer Interactions." *International Journal for Numerical Methods in Fluids*, 9, 747-761, 1989.

[10] Hall, E. and Pletcher, R. H. "A Comparison of Central Difference Algorithms with a Novel Conjugate Gradient TVD Scheme." AIAA 88-3527, 1988.

[11] Hindman, R. G. "On Shock Capturing Methods and Why They Work." AIAA 88-0622, 1988.

[12] Karki, K. C. and Patankar, S. V. "Pressure Based Calculation Procedure for Viscous Flows at All Speeds in Arbitrary Configurations." *AIAA Journal*, 27, No. 9, 1167-1174, 1989.

[13] Van Doormaal, J. P., Raithby, G. D. and Mcdonald, B. H. "The Segregated Approach to Predicting Viscous Compressible Fluid flows." *Journal of Turbomachinery*, Transactions of the ASME, 109, 268-277, 1987.

[14] Patankar, S. V. *Numerical Heat Transfer and Fluid Flow.* Hemisphere Publishing Corp., New York, 1981.

[15] Roache, P. *Computational Fluid Dynamics.* Hermosa Publishers, Albuquerque, New Mexico, 1972.

[16] Osswald, G. A., Ghia, K. N. and Ghia, U. "A Direct Algorithm for Solution of Incompressible Three-Dimensional Unsteady Navier-Stokes Equations." AIAA-87-1139, 1987.

[17] Guj, G. and Stella, F. "Numerical Solutions of High-Re Recirculating flows in vorticity-velocity form." *International Journal for Numerical Methods in Fluids*, 8, 405-416, 1988.

[18] Gegg, S. *A Dual Potential Formulation of the Navier-Stokes Equations.* Ph.D. Dissertation, Iowa State University, Ames, Iowa, 1989.

[19] Rogers, S. E. and Kwak, D. "An Upwind Differencing Schemes for the Time-Accurate Incompressible Navier-Stokes Equations." AIAA 88-2583, 1988.

[20] Merkle, C. L. and Athavale, M. "Time-Accurate Unsteady Incompressible Flow Algorithm Based on Artificial Compressibility." AIAA-87-1137, 1987.

[21] Pan, D. and Chakravarthy, S. "Unified Formulation for Incompressible Flows." AIAA-89-0122, 1989.

[22] Chorin, A. J. "A Numerical Method for Solving Incompressible Viscous Flows Problems." *Journal of Computational Physics*, 2, 12-26, 1967.

[23] Issa, R. I. "Numerical Methods for Two- and Three-Dimensional Recirculating Flows." *Computational Methods for Turbulent, Transonic and Viscous Flows*, Ed. by J. A. Essecs. Hemisphere Publishing Corp., New York, 1983.

[24] Karki, K. C. *A Calculation Procedure for Viscous Flows at All Speeds in Complex Geometries.* Ph.D. Dissertation. University of Minnesota, 1986.

[25] Merkle, C. L. and Choi, Y.-H. "Computation of Compressible Flows at Very Low Mach Numbers." AIAA 86-0351, 1986.

[26] TenPas, P. W. and Pletcher, R. H. "Solution of the Navier-Stokes Equations for Subsonic Flows using a Coupled Space-Marching Method." AIAA-87-1173-cp, 1987.

[27] Feng, J. and Merkle, C. L. "Evaluation of Preconditioning Methods for Time-Marching Systems." AIAA-90-0016, 1990.

[28] Warming, R. F. and Beam, R. M. "On the Construction and Application of Implicit Factored Schemes for Conservation Laws." *SIAM-AMS Proceedings*, 11, 85-129, 1978.

[29] Stone, H. L. "Iterative Solution of Implicit Approximations of Multi-dimensional Partial Differential Equations." *SIAM Journal of Numerical Analysis*, 5, No. 3, 1968.

[30] Schneider, G. E. and Zedan, M. "A Modified Strongly Implicit Procedure for the Numerical Solution of Field Problems." *Numerical Heat Transfer*, 4, 1-19, 1981.

[31] Harlow, F. H. and Amsden, A. A. "Numerical Calculation of Almost Incompressible Flow." *Journal of Computational Physics*, 3, 80-93, 1968.

[32] Peterson, L. D., Crawley, E. F. and Hansman, R. J. "Nonlinear Fluid Slosh Coupled to the Dynamics of a Spacecraft." *AIAA Journal*, 27, No. 9, 1230-1240, 1989.

[33] Kana, D. D. "Validated Spherical Pendulum Model for Rotary Liquid Slosh." *Journal of Spacecraft and Rockets*, 26, No. 3, 188-195, 1989.

[34] Van Schoor, M. C., Peterson, L. D. and Crawley, E. F. "The Coupled Nonlinear Dynamic Characteristics of Contained Fluids in Zero Gravity." AIAA-90-0996-CP, 1990.

[35] Vaughn, H. R., Oberkampf, W. L. and Wolfe, W. P. "Fluid Motion Inside a Spinning Nutating Cylinder." Journal of Fluid Mechanics, 150, 121-138, 1985.

[36] Chorin, A. J. "Numerical Solution of the Navier-Stokes Equation." *Mathematics of Computation*, 22, No. 104, 745-762, 1968.

[37] Harlow, F. H. and Welch, J. E. "Numerical Calculation of Time-Dependent Viscous Incompressible Flow of Fluid with Free Surface." *The Physics of Fluids*, 8, No. 12, 2182-2189, 1965.

[38] Kassinos, A. C. and Prusa, J. M. "A Numerical Modeling for 3-D Viscous Sloshing in a Moving Container." To be presented in ASME Annual Winter Meeting, Symposium on Recent Advances and Applications in CFD, Dallas, TX, Nov. 25-30, 1990.

[39] Hirt, C. W. and Nichols, B. D. "Volume of Fluid (VOF) Method for the Dynamics of Free Boundaries." *Journal of Computational Physics*, 39, 201-225, 1981.

[40] Floryan, J, M. and Rasmussen, H. "Numerical Methods for Viscous Flows with Moving Boundaries." *Applied Mechanics Reviews*, 42, No. 12, 323-341, 1989.

[41] Chakravarthy, S. R. "Numerical Simulation of Laminar, Incompressible Flow within Liquid filled Shells." Contract Report ARBRL-CR-00491, US Army Research and Development Command, Ballistic Research Laboratory, 1982.

[42] Holler, H. and Ranov, T. "Unsteady Rotating Flow in a Cylinder with a Free Surface." ASME Paper No. 68-FE-13, 1968.

[43] Nakamura, S. *Computational Methods in Engineering and Science with Applications to Fluid Dynamics and Nuclear System.* Wiley, New York, 1977.

[44] Zedan, M. and Schneider, G. E. "A Coupled Strongly Implicit Procedure for Velocity and Pressure Calculation in Fluid Flow Problems." *Numerical Heat Transfer*, 8, 537-557, 1985.

[45] Weinstein, H. G., Stone, H. L. and Kwan, T. V."Iterative Procedure for Solution of Systems of Parabolic and Elliptic Equations in Three Dimensions." *I & EC Fundamentals*, 8, No. 2, 281-287, 1969.

[46] Zedan, M. and Schneider, G. E. "A Three-Dimensional Modified Strongly Implicit Procedure for Heat Conduction." *AIAA Journal*, 21, No. 2, 295-303, 1983.

[47] Walters, R. W., Dwoyer, D. L. and Hassan, H. A. "A Strongly Implicit Procedure for the Compressible Navier-Stokes Equations." *AIAA Journal*, 24, No. 1, 6-12, 1986.

[48] Reddy, D. R. and Rubin, S. G. "Consistent Boundary Conditions for Reduced Navier-Stokes (RNS) Scheme Applied to Three-Dimensional Internal Viscous Flows." AIAA-88-0714, 1988.

[49] Rubin, S. G. and Khosla, P. G. "Navier-Stokes Calculations with a Coupled Strongly Implicit Method - I: Finite Difference Solutions." *Computers and Fluids*, 9, 163-180, 1981.

[50] Ramakrishnan, S. V. and Rubin, S. G. "Time-Consistent Pressure RNS Solutions for Unsteady Subsonic Flow over Airfoils." AIAA 88-3561-CP, 1988.

[51] Vinokur, M. "Conservation of Equations of Gas Dynamics in Curvilinear Coordinate Systems." *Journal of Computational Physics*, 14, 105-125, 1974.

[52] Sorenson, R. L. *The 3DGRAPE Book: Theory, Users' Manual, Examples.* NASA TM-102224, 1989.

[53] Hindman, R. G. "Generalized Coordinate Forms of Governing Fluid Equations and Associated Geometrically Induced Errors." *AIAA Journal*, 20, No. 10, 1359-1367, 1982.

[54] Golub, G. H. and Van Loan, C. F. *Matrix Computations.* Johns Hopkins University Press, Baltimore, Maryland, 1983.

[55] Hesse, W. J. and Mumford, N. V. S., Jr. *Jet Propulsion for Aerospace Applications.* Pitman Pub. Corp., New York, 1964.

[56] Morihara, H. and Cheng, R. T. "Numerical Solution of the Viscous Flow in Entrance Region of Parallel Plates." *Journal of Computational Physics*, 11, 550-572, 1973.

[57] McDonald, J. W., Denny, V. E. and Mills, A. F. "Numerical Solutions of the Navier-Stokes Equations in Inlet Regions." *Journal of Applied Mechanics*, Series E, 39, 873-878, 1972.

[58] Bodoia, J. R. and Osterle, J. F. "Finite Difference Analysis of Plane Poiseuille and Couette Flow Development." *Applied Scientific Research*, Section A, 10, 265-276, 1961.

[59] Hwang, C.-L. and Fan, L.-T. "Finite Difference Analysis of Forced Convection Heat Transfer in Entrance Region of a Flat Rectangular Duct." *Applied Scientific Research*, Section A, 13, 401-422, 1964.

[60] Ghia, U., Ghia, K. N. and Shin, C. T. "High-Re Solutions for Incompressible Flow Using the Navier-Stokes Equations and a Multigrid Method." *Journal of Computational Physics*, 48, 387-411, 1982.

[61] Napolitano, M. and Walters, R. W. "An Incremental Block-Line-Gauss-Seidel Method for the Navier-Stokes Equations." *AIAA Journal*, 24, No. 5, 770-776, 1986.

[62] Goodrich, J. W. and Soh, W. Y. "Time Dependent Viscous Incompressible Navier-Stokes Equations: The Finite Difference Galerkin Formulation and Streamfunction Algorithm." *Journal of Computational Physics*, 84, No. 1, 207-241, 1989.

[63] Mansour, M. L. and Hamed, A. "Implicit Solutions of the Incompressible Navier-Stokes Equations in Primitive Variables." AIAA-87-0717, 1987.

[64] Abdallah, S. "Numerical Solutions for the Incompressible Navier-Stokes Equations in Primitive Variables Using a Nonstaggered Grids, I and II." *Journal of Computational Physics*, 70, 193-202, 1987.

[65] Chen, C.-J., Ho, K.-S. and Cheng, W.-S. "The Finite Analytic Method." Volume 5, IIHR Report No. 232-V. Iowa Institute of Hydraulic Research, The University of Iowa, Iowa City, Iowa, 1982.

[66] Ghia, K. N., Hankey, W. L., Jr., and Hodge, J. K. "Study of Incompressible Navier-Stokes Equations in Primitive Variables Using Implicit Numerical Technique." AIAA-77-648, 1977.

[67] Goodrich, J. W., Gustafson, K. and Halasi, K. "Hopf Bifurcation in the Driven Cavity." NASA TM 102334 (or ICOMP-89-21), Oct. 1989.

[68] Shyy, W. "Computation of Complex Fluid Flows Using an Adapted Grid Method." *International Journal for Numerical Methods in Fluids*, 8, 475-489, 1988.

[69] Burggraf, O. R. "Analytic and Numerical Studies of the Structure of Steady Separated Flows." *Journal of Fluid Mechanics*, Part 1, 24, 113-151, 1966.

[70] Roache, P. and Salari, K. "Weakly Compressible Navier-Stokes Solutions with an Implicit Approximate Factorization Code." AIAA-90-0235, 1990.

[71] Fornberg, B. "A numerical Study of Steady Viscous Flow Past a Circular Cylinder." *Journal of Fluid Mechanics*, Part 4, 98, 819-855, 1980.

[72] Majumdar, S. and Rodi, W. "Numerical Calculations of Turbulent Flow Past Circular Cylinders." 3-13 - 3-25. *Third Symposium on Numerical and Physical Aspects of Aerodynamic Flows, Long Beach*, California State University, 1985.

[73] Acrivos, A., Leal, L. G., Snowden, D. D. and Pan, F. "Further Experiments on Steady Separated Flow Past Bluff Objects." *Journal of Fluid Mechanics*, 34, 25-48, 1968.

[74] Rhie, C. M. *A Numerical Study of the Flow Past an Isolated Airfoil with Separation.* Ph.D. Dissertation. University of Illinois, 1981.

[75] Son, J. S. and Hanratty, T. J. "Numerical Solution for the Flow Around a Circular Cylinder at Reynolds Number of 40, 200 and 500." *Journal of Fluid Mechanics*, 35, 369-386, 1969.

[76] Peyret, R. and Taylor, T. D. *Computational Methods for Fluid Flow.* Springer-Verlag, New York, 1983.

[77] Lecointe, Y. and Piquet, J. "On the Use of Several Compact Methods for the Study of Unsteady Incompressible Viscous Flow Around a Circular Cylinder." *Computers & Fluids*, 12, No. 4, 255-280, 1984.

[78] Visbal, M. R. "Evaluation of an Implicit Navier-Stokes Solver for Some Unsteady Separated Flows." AIAA-86-1053, 1986.

[79] Panton, R. L. *Incompressible Flow.* Wiley, New York, 1984.

[80] Roshko, A. "On the Development of Turbulent Wakes from Vortex Streets." NACA TN-2913, 1953.

[81] Thomas, J. L. and Walters, R. W. "Upwind Relaxation Algorithms for the Navier-Stokes Equations." AIAA-85-1501, 1985.

[82] Buelow, P. E. *Comparison of TVD Schemes Applied to the Navier-Stokes Equations.* Master Thesis. Iowa State University, 1988.

[83] Hakkinen, R. J., Greber, I., Trilling, L. and Arbarbanel, S. S. "The Interaction of an Oblique Shock Wave with a Laminar Boundary Layer." NASA Memo-2-18-59W, March, 1959.

[84] Rosenfeld, M., Kwak, D. and Vinokur, M. "A Solution Method for the Unsteady and Incompressible Navier-Stokes Equations in Generalized Coordinates Systems." AIAA-88-0718, 1988.

[85] Ku, H., Hirsh R. and Taylor, T. "A pseudospectral Method for Solution of Three-Dimensional Navier-Stokes Equations." *Journal of Computational Physics*, 70, 439-462, 1987.

[86] White, F. M. *Fluid Mechanics.* McGraw-Hill Book Co., New York, 1986

8. APPENDIX A: DERIVATION OF THE TRANSFORMATION MATRIX A AND S

8.1 Transformation Matrix A

Each of the three successive rotations (see Fig. 2.2) can be expressed as:

$$x_0 = [\bar{\bar{A}}_{01}]\bar{\bar{x}}_1$$

$$\bar{\bar{x}}_1 = [\bar{A}_{01}]\bar{x}_1$$

$$\bar{x}_1 = [A_{01}]x_1$$

where $[\bar{\bar{A}}_{01}]$, $[\bar{A}_{01}]$ and $[A_{01}]$ are the transformation matrices with respect to each axis rotation. These three transformation matrices are:

$$[\bar{\bar{A}}_{01}] = \begin{bmatrix} C_3 & -S_3 & 0 \\ S_3 & C_3 & 0 \\ 0 & 0 & 1 \end{bmatrix}$$

$$[\bar{A}_{01}] = \begin{bmatrix} C_2 & 0 & S_2 \\ 0 & 1 & 0 \\ -S_2 & 0 & C_2 \end{bmatrix}$$

$$[A_{01}] = \begin{bmatrix} 1 & 0 & 0 \\ 0 & C_1 & -S_1 \\ 0 & S_1 & C_1 \end{bmatrix}$$

where $C_i = \cos\psi_i$ and $S_i = \sin\psi_i$.

Therefore, the relationship between coordinates x_0 and x_1 can be expressed as:

$$\begin{aligned} x_0 &= [\bar{A}_{01}][\bar{A}_{01}][A_{01}]x_1 \\ &= [A]x_1 \end{aligned}$$

The final transformation matrix $[A]$ is:

$$[A] = \begin{bmatrix} C_2C_3 & S_1S_2C_3 - C_1S_3 & C_1C_3S_2 + S_1S_3 \\ C_2S_3 & S_1S_2S_3 + C_1C_3 & C_1S_2S_3 - S_1C_3 \\ -S_2 & S_1C_2 & C_1C_2 \end{bmatrix}$$

8.2 Transformation Matrix S

The transformation for this rotation can be seen in Fig. 2.3. The resulting matrix is:

$$[S] = \begin{bmatrix} \cos\phi_r & 0 & -\sin\phi_r \\ 0 & 1 & 0 \\ \sin\phi_r & 0 & \cos\phi_r \end{bmatrix}$$

9. APPENDIX B: UNIT NORMAL VECTOR AT THE WALL OF THE CONTAINER

In the present formulation the container wall coincides with the $z = z_{2max}$ surface (see Fig. 9.1). Letting $\vec{n}$ be a unit vector normal to the wall, then it can be expressed as:

$$\vec{n} = -\frac{\nabla z_2}{|\nabla z_2|})_{at\ \ wall}$$

Since ∇z_2 is equal to $\hat{e}_{31}\eta_{2,1} + \hat{e}_{32}\eta_{2,2} + \hat{e}_{33}\eta_{2,3}$, the expression for $\vec{n}$ can be written as:

$$\vec{n} = -\frac{\hat{e}_{31}\eta_{2,1} + \hat{e}_{32}\eta_{2,2} + \hat{e}_{33}\eta_{2,3}}{(\eta_{2,1}^2 + \eta_{2,2}^2 + \eta_{2,3}^2)^{1/2}})_{at\ \ wall}$$

or

$$n_i = -\frac{\eta_{2,i}}{(\eta_{2,j}^2)^{1/2}})_{at\ \ wall}$$

where $\hat{e}_{31}$, $\hat{e}_{32}$ and $\hat{e}_{33}$ are the unit base vectors in the x_{31}, x_{32} and x_{33} directions respectively.

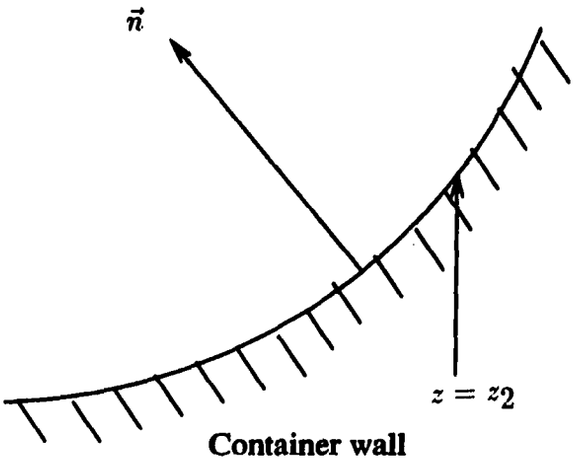

Figure 9.1: Notation for the unit normal vector at the wall of the spherical container

10. APPENDIX C: UNIT NORMAL VECTORS AT THE FREE SURFACE

At the free surface, the unit normal vector (see Fig. 10.1) can be expressed as:

$$n_i = -\frac{\eta_{3,i}}{(\eta_{3,j}^2)^{1/2}})_{at\ \ free\ \ surface}$$

The two unit tangential vectors can be derived from the condition of orthogonality and the requirement of unit length. They are expressed as:

$$\vec{\tau}_1 = \frac{\hat{e}_{31} - \hat{e}_{32}\alpha}{(1+\alpha^2)^{1/2}}$$

and

$$\vec{\tau}_2 = \frac{-\hat{e}_{31}\alpha\beta + \hat{e}_{32}(1+\alpha^2) - \hat{e}_{33}\beta}{(1+\alpha^2+\beta^2)^{1/2}(1+\alpha^2)^{1/2}}$$

where $\hat{e}_{31}$, $\hat{e}_{32}$ and $\hat{e}_{33}$ are the unit base vectors in the x_{31}, x_{32} and x_{33} directions respectively and $\alpha = \frac{n_1}{n_3}$ and $\beta = \frac{n_2}{n_3}$.

The three curvature terms are:

$$\kappa_1 = \frac{\frac{\partial^2 F}{\partial x_{31}^2}}{[1 + (\frac{\partial F}{\partial x_{31}})^2]^{3/2}}$$

$$\kappa_2 = \frac{\frac{\partial^2 F}{\partial x_{32}^2}}{[1 + (\frac{\partial F}{\partial x_{32}})^2]^{3/2}}$$

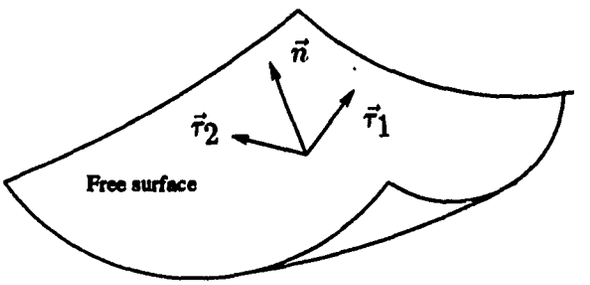

Figure 10.1: Notation for the unit vectors at the free surface

$$\kappa = \frac{\frac{\partial^2 F}{\partial x_{31}^2} + \frac{\partial^2 F}{\partial x_{32}^2}}{[1 + (\frac{\partial F}{\partial x_{31}})^2 + (\frac{\partial F}{\partial x_{32}})^2]^{3/2}}$$

Central differences were used to evaluate the spatial derivatives in the above three curvature terms.

11. APPENDIX D: EQUIVALENCE OF THE JACOBIAN AND NEWTON LINEARIZATION METHODS

The Jacobian method is often used to linearize the compressible Navier-Stokes equations [7]. This method usually evaluates the coefficient matrices at the previous time level. On the other hand, the Newton method [7] usually evaluates the coefficient matrices at the previous iteration level of the current time time step. It was found that if the conservative variables were used as the primary variables, both linearization schemes gave equivalent forms of the algebraic equations. Both schemes would be identical if the coefficient matrices were evaluated at the previous time level (instead of previous iteration level of the current time step) for the Newton method. However, both schemes could give a different form of the algebraic equations, depending on how the conservative variables were converted to the primitive variables, if the primitive variables were used. The conclusion is that both linearization methods are equivalent and will become identical if the Newton method is used in the linearization required to convert the conservative variables to the primitive variables, and if the coefficient matrices are evaluated at the same level for both schemes. This equivalence can be demonstrated as follows.

The two-dimensional Euler equations are used here to demonstrate the equivalence of the present Newton linearization method and the Jacobian matrices method.

To be consistent with the equations used in the present work, an isothermal condition with $p=\rho\beta$ relation was assumed in the Euler equations without any loss of generality. The two-dimensional Euler equations with the above conditions in Cartesian coordinates are given by:

$$\frac{\partial Q}{\partial t}+\frac{\partial E}{\partial x}+\frac{\partial F}{\partial y}=0 \tag{11.1}$$

where

$$Q=\begin{pmatrix} p \\ pu \\ pv \end{pmatrix}, \quad E=\begin{pmatrix} pu \\ pu^2+\beta p \\ puv \end{pmatrix}, \quad F=\begin{pmatrix} pv \\ puv \\ pv^2+\beta p \end{pmatrix}$$

A forward difference in time and central difference in space (FTCS) scheme will be used for all the following difference forms. The FTCS scheme was chosen to easily demomstrate the present derivation only. Other differencing schemes certainly can be used as well.

11.1 Conservative Variables

11.1.1 Jacobian method

When the FTCS scheme is applied to the above equation with $\frac{\Delta t}{\Delta x}=\frac{\Delta t}{\Delta y}=1$(for simplicity), the finite-difference form is given as

$$-A^n_{i-1,j}Q^{n+1}_{i-1,j}-B^n_{i,j-1}Q^{n+1}_{i,j-1}+Q^{n+1}_{i,j}+B^n_{i,j+1}Q^{n+1}_{i,j+1}+A^n_{i+1,j}Q^{n+1}_{i+1,j}=Q^n_{i,j} \tag{11.2}$$

where

$$A = \frac{\partial E}{\partial Q} = \begin{bmatrix} 0 & 1 & 0 \\ -\frac{m_2^2}{m_1^2} + \beta & \frac{2m_2}{m_1} & 0 \\ -\frac{m_2 m_3}{m_1^2} & \frac{m_3}{m_1} & \frac{m_2}{m_1} \end{bmatrix}, \quad B = \frac{\partial F}{\partial Q} = \begin{bmatrix} 0 & 0 & 1 \\ -\frac{m_2 m_3}{m_1^2} & \frac{m_3}{m_1} & \frac{m_2}{m_1} \\ -\frac{m_3^2}{m_1^2} + \beta & 0 & \frac{2m_3}{m_1} \end{bmatrix}$$

are the Jacobian matrices. The superscript n represents the previous time level. The m_1, m_2 and m_3 are the conservative variables in Q vector, i.e., m_1=p, m_2=pu and m_3=pv.

11.1.2 Newton method

If a Newton linearization method is used to linearize the convective terms in E and F vectors, a typical nonlinear term in the third element of E is given as:

$$\frac{m_2 m_3}{m_1} \simeq -\frac{\bar{m}_2 \bar{m}_3}{\bar{m}_1^2} m_1 + \frac{\bar{m}_3}{\bar{m}_1} m_2 + \frac{\bar{m}_2}{\bar{m}_1} m_3$$

where $\bar{m}_1$, $\bar{m}_2$ and $\bar{m}_3$ are the values at the previous iteration level. After all the terms are linearized in the same way as above and the FTCS scheme is applied to the Euler equations, the final difference form, after collecting all terms in front of each unknown, is given as:

$$-A^k_{i-1,j} Q^{n+1}_{i-1,j} - B^k_{i,j-1} Q^{n+1}_{i,j-1} + Q^{n+1}_{i,j} + B^k_{i,j+1} Q^{n+1}_{i,j+1} + A^k_{i+1,j} Q^{n+1}_{i+1,j} = Q^n_{i,j} \tag{11.3}$$

where the superscript k indicates the previous iteration level. Equation (11.2) and Eq. (11.3) are identical if k is equal to n. This means if no subiteration is used at each time step. Therefore, the final difference form derived from the Newton method can be obtained directly from Eq. (11.2) by evaluating the Jacobian matrices A and

B in the previous iteration level k instead of the previous time level n. In many low speed flow problems, subiterations are usually desirable and Eq. (11.3) is more appropriate to use.

11.2 Primitive Variables

11.2.1 Jacobian method

One more step is needed to convert the conservative variable vector, Q, to a primitive variable vector, $\tilde{Q}$, if a primitive variables approach is desired. There are different ways of conversion (or linearization). The way we choose here is a Newton method and it is expressed as:

$$Q \simeq C\tilde{Q} - Q_0^n \tag{11.4}$$

where

$$\tilde{Q} = \begin{pmatrix} p \\ u \\ v \end{pmatrix}, \quad Q_0 = \begin{pmatrix} 0 \\ pu \\ pv \end{pmatrix}, \quad C = \frac{\partial Q}{\partial \tilde{Q}} = \begin{bmatrix} 1 & 0 & 0 \\ u & p & 0 \\ v & 0 & p \end{bmatrix}$$

The Q_0 term is evaluated at the previous time level, n, to be consistent with the Jacobian time linearization. After substituting Eq. (11.4) into Eq. (11.2), the following difference form is obtained for the primitive variables:

$$-\tilde{A}^n_{i-1,j}\tilde{Q}^{n+1}_{i-1,j} - \tilde{B}^n_{i,j-1}\tilde{Q}^{n+1}_{i,j-1} + C^n_{i,j}\tilde{Q}^{n+1}_{i,j} + \tilde{B}^n_{i,j+1}\tilde{Q}^{n+1}_{i,j+1} + \tilde{A}^n_{i+1,j}\tilde{Q}^{n+1}_{i+1,j} = Q^n_{i,j} + Q^n_{0i,j} - Q^n_{Ai-1,j} - Q^n_{Bi,j-1} + Q^n_{Bi,j+1} + Q^n_{Ai+1,j} \tag{11.5}$$

where

$$\tilde{A} = AC = \begin{bmatrix} u & p & 0 \\ u^2+\beta & 2pu & 0 \\ uv & pv & pu \end{bmatrix}, \quad \tilde{B} = BC = \begin{bmatrix} v & 0 & p \\ uv & pv & pu \\ v^2+\beta & 0 & 2pv \end{bmatrix}$$

$$Q_A = AQ_0 = \begin{pmatrix} pu \\ 2pu^2 \\ 2puv \end{pmatrix}, \quad Q_B = BQ_0 = \begin{pmatrix} pv \\ 2puv \\ 2pv^2 \end{pmatrix}$$

11.2.2 Newton method

If the Newton method is applied to linearize the nonlinear terms such as

$$pu \simeq \bar{u}p + \bar{p}u - \bar{p}\bar{u},$$

$$puv \simeq \bar{u}\bar{v}p + \bar{p}\bar{v}u + \bar{p}\bar{u}v - 2\bar{p}\bar{u}\bar{v},$$

$$pu^2 \simeq \bar{u}^2 p + 2\bar{p}\bar{u}u - 2\bar{p}\bar{u}^2,$$

and the FTCS scheme is used again, then after collecting all coefficients in front of each unknown, the final difference form is given as:

$$-\tilde{A}^k_{i-1,j}\tilde{Q}^{n+1}_{i-1,j} - \tilde{B}^k_{i,j-1}\tilde{Q}^{n+1}_{i,j-1} + C^k_{i,j}\tilde{Q}^{n+1}_{i,j} + \tilde{B}^k_{i,j+1}\tilde{Q}^{n+1}_{i,j+1} + \tilde{A}^k_{i+1,j}\tilde{Q}^{n+1}_{i+1,j} = Q^n_{i,j} + Q^k_{0i,j} - Q^k_{Ai-1,j} - Q^k_{Bi,j-1} + Q^k_{Bi,j+1} + Q^k_{Ai+1,j} \quad (11.6)$$

where the superscript k indicates the previous iteration level. The above equation is identical to the Eq. (11.5) except that all the coefficients in the left-hand side and most quantities in the right-hand side are evaluated at the previous iteration level, k. By simply marching in time without subiterations at each time step, the Newton method is identical to the Jacobian time linearization method; however, the former provides more flexibility in subiterations than the later.

12. APPENDIX E: DERIVATION OF THE STEADY STATE ANALYTICAL FREE SURFACE POSITION

The analytical free surface position for two kinds of spin-up problems will be derived in this appendix.

12.1 Axisymmetric Spin-Up

When solid-body rotation prevails, the following equations can be derived from a force balance:

$$-\frac{\partial p}{\partial r} = -\rho\Omega^2 r$$
$$-\frac{1}{r}\frac{\partial p}{\partial \theta} = 0$$
$$-\frac{\partial p}{\partial z} = \rho g$$

where Ω is the rotational speed in the z direction.

The pressure solution can be obtained by direct integration from the above three equations. The solution for pressure is:

$$p = \frac{1}{2}\rho\Omega^2 r^2 - \rho g z + C$$

The constant C can be determined by assuming that the pressure at the free surface is equal to the atmospheric pressure, p_a. The final form of the pressure solution is:

$$p - p_a = \frac{1}{2}\rho\Omega^2 r^2 - \rho g(z - z_m)$$

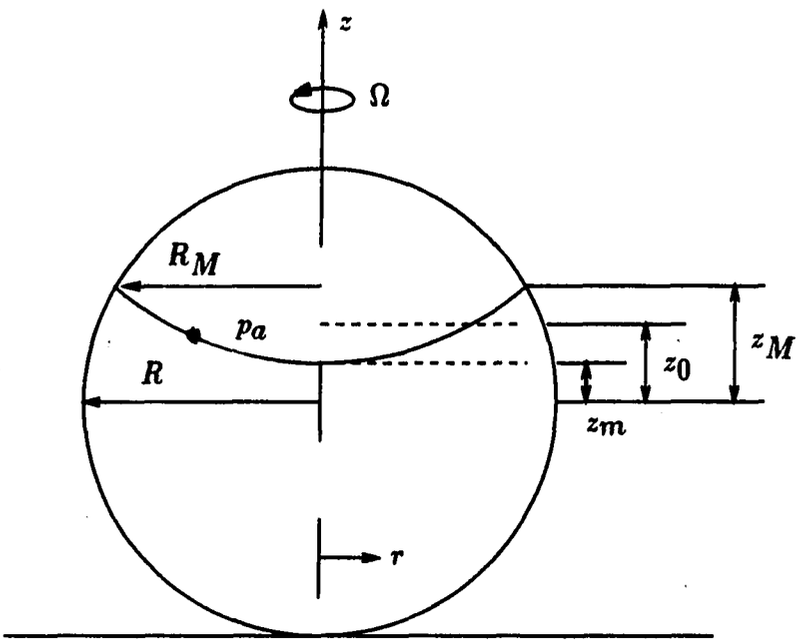

Figure 12.1: Notation for the free surface of the spherical container

where z_m is the free surface height at the center point (see Fig. 12.1).

Letting $p = p_a$ in the above equation, the free surface position can be written as a function of r as:

$$z = \frac{\Omega^2 r^2}{2g} + z_m$$

12.1.1 Determination of z_m

If the spherical container is initially partially filled by a fluid at a height of z_0, then the volume of fluid can be expressed as:

$$V_0 = \frac{4}{3}\pi R^3 - \frac{1}{3}\pi(R - z_0)^2(2R + z_0)$$

When the final solid-body rotation prevails, the volume of fluid can be expressed as:

$$V_s = \frac{4}{3}\pi R^3 - \frac{1}{3}\pi(R - z_M)^2[3R - (R - z_M)] - \frac{1}{2}\pi R_M^2(z_M - z_m)$$

By equating $V_0 = V_s$, we can obtain the following nonlinear equation in terms of the unknown z_M:

$$z_M^4 + \frac{1}{A} z_M^3 - 2R^2 z_M^2 - \frac{3R^2}{A} z_M + (R^4 + \frac{2R^3}{A} - \frac{B}{A}) = 0$$

where $A = \frac{3\Omega^2}{4g}$ and $B = (R - z_0)(2R + z_0)$.

The Newton-Raphson method was used to solve for the unknown z_M. Once z_M is calculated, z_m can be obtained from:

$$z_m = z_M - \frac{\Omega^2}{2g}(R^2 - z_M^2)$$

12.2 Asymmetric Spin-Up

The same procedure as given above can be used to derive the equation for the free surface height for the asymmetric spin-up case. The equation for the free surface height is:

$$z = \frac{\Omega^2}{g}(\frac{1}{2}r^2 + hr\cos\theta) + z_m$$

where h is the length of the rotational arm.

The constant z_m has to be determined by mass conservation using the same procedure as above. However, in this case there is no analytical form of the volume of fluid for the final solid-body rotation. It has to be determined numerically as suggested in the following procedure.

12.2.1 Determination of z_m - secant method

Let z_0 and z_1 be two initial guesses for the solution z_m. Then two fluid volumes corresponding to these two initial guesses can be determined, say V_0 and V_1. If the

initial volume of fluid is designated as V_i, then the following secant method can be used to iterate to obtain the solution for z_m which satisfies mass conservation:

$$f = V_1 - V_i$$

$$f' = (V_1 - V_0)/(z_1 - z_0)$$

$$z_{new} = z_1 - f/f'$$

12.2.2 Determination of the volume of fluid

The following procedures were used to determine the volume of fluid once a z_m had been guessed:

1. Find the coordinates (r_w,z_w) of the free surface at the wall for each θ direction from the solution of the following two equations:

$$z = \frac{\Omega^2}{g}(\frac{1}{2}r^2 + hr\cos\theta) + z_m$$

and

$$r^2 + z^2 = 1$$

This will involve using the Newton-Raphson method to solve the resulting nonlinear equations.

2. Find the area and centroid of the area of the fluid for each θ direction by the trapezoidal rule.

3. Calculate the volume of fluid by summing up all areas for each θ direction by the trapezoidal rule.

13. APPENDIX F: FORMULA FOR CALCULATING [L] AND [U] MATRICES FOR SIP METHOD

13.1 Two-Dimensional 9-Point Equations

$$a_{i,j} = A^6_{i,j} \tag{13.1}$$

$$b_{i,j} = (A^5_{i,j} - a_{i,j}f_{i-1,j-1} - \alpha A^4_{i,j}f_{i+1,j-1})(1 - \alpha f_{i,j-1}f_{i+1,j-1})^{-1} \tag{13.2}$$

$$c_{i,j} = A^4_{i,j} - b_{i,j}f_{i,j-1} \tag{13.3}$$

$$d_{i,j} = (A^7_{i,j} - a_{i,j}h_{i-1,j-1} - b_{i,j}g_{i,j-1} - 2\alpha a_{i,j}g_{i-1,j-1})(1 + 2\alpha g_{i-1,j})^{-1} \tag{13.4}$$

$$e_{i,j} = A^9_{i,j} - a_{i,j}s_{i-1,j-1} - b_{i,j}h_{i,j-1} - c_{i,j}g_{i+1,j-1} - d_{i,j}f_{i-1,j} + \alpha(2\phi^1_{i,j} + \phi^2_{i,j} + \phi^3_{i,j} + 2\phi^4_{i,j}) \tag{13.5}$$

$$f_{i,j} = (e_{i,j})^{-1}(A^3_{i,j} - b_{i,j}s_{i,j-1} - c_{i,j}h_{i+1,j-1} - 2\alpha(\phi^1_{i,j} + \phi^3_{i,j})) \tag{13.6}$$

$$g_{i,j} = (e_{i,j})^{-1}(A^8_{i,j} - d_{i,j}h_{i-1,j}) \tag{13.7}$$

$$h_{i,j} = (e_{i,j})^{-1}(A^1_{i,j} - d_{i,j}s_{i-1,j} - \alpha\phi^4_{i,j}) \tag{13.8}$$

$$s_{i,j} = (e_{i,j})^{-1}(A^2_{i,j}) \tag{13.9}$$

where α is called partial cancellation parameter which is used to reduce the effect of the auxiliary matrix [P]. One can also think it is convergence acceleration factor. Its

value should range between 0 and 1. For the present coupled system of equation, α is usually chosen between 0 and 0.25.

The definition of $\phi^1_{i,j}$, $\phi^2_{i,j}$, $\phi^3_{i,j}$ and $\phi^4_{i,j}$ are expressed as follows:

$$\phi^1_{i,j} = c_{i,j} f_{i+1,j-1} \tag{13.10}$$

$$\phi^2_{i,j} = a_{i,j} g_{i-1,j-1} \tag{13.11}$$

$$\phi^3_{i,j} = c_{i,j} s_{i+1,j-1} \tag{13.12}$$

$$\phi^4_{i,j} = d_{i,j} g_{i-1,j} \tag{13.13}$$

13.2 Three-Dimensional 7-Point Equations

$$a_{i,j,k} = A^b_{i,j,k}(1 + \alpha_2 h_{i,j,k-1} + \alpha_3 r_{i,j,k-1})^{-1} \tag{13.14}$$

$$d_{i,j,k} = A^s_{i,j,k}(1 + \alpha_3 v_{i,j-1,k} + \alpha_1 h_{i,j-1,k})^{-1} \tag{13.15}$$

$$f_{i,j,k} = A^w_{i,j,k}(1 + \alpha_2 v_{i-1,j,k} + \alpha_1 r_{i-1,j,k})^{-1} \tag{13.16}$$

$$\begin{aligned} g_{i,j,k} = {} & A^p_{i,j,k} + \alpha_2(\phi^1_{i,j,k} + \phi^6_{i,j,k}) + \alpha_3(\phi^2_{i,j,k} + \phi^5_{i,j,k}) \\ & + \alpha_1(\phi^3_{i,j,k} + \phi^4_{i,j,k}) - f_{i,j,k} h_{i-1,j,k} - d_{i,j,k} r_{i,j-1,k} - a_{i,j,k} v_{i,j,k-1} \end{aligned} \tag{13.17}$$

$$h_{i,j,k} = g^{-1}_{i,j,k}(A^e_{i,j,k} - \alpha_2 \phi^2_{i,j,k} - \alpha_1 \phi^3_{i,j,k}) \tag{13.18}$$

$$r_{i,j,k} = g^{-1}_{i,j,k}(A^n_{i,j,k} - \alpha_3 \phi^2_{i,j,k} - \alpha_1 \phi^4_{i,j,k}) \tag{13.19}$$

$$v_{i,j,k} = g^{-1}_{i,j,k}(A^t_{i,j,k} - \alpha_2 \phi^6_{i,j,k} - \alpha_3 \phi^5_{i,j,k}) \tag{13.20}$$

where α_1, α_2 and α_3 are the partial cancellation parameter in the x, y and z directions respectively, which are used to reduce the effect of the auxiliary matrix $[P]$. One can

also think it is convergence acceleration factor. Its value should range between 0 and 1. For the present coupled system of equation, α_1, α_2 and α_3 are set to be equal for simplicity. Usually 0.5 was used for the present three-dimensional calculations. The definition of $\phi^1_{i,j,k}$, $\phi^2_{i,j,k}$, $\phi^3_{i,j,k}$, $\phi^4_{i,j,k}$, $\phi^5_{i,j,k}$ and $\phi^6_{i,j,k}$ are expressed as follows:

$$\phi^1_{i,j,k} = a_{i,j,k} h_{i,j,k-1} \tag{13.21}$$

$$\phi^2_{i,j,k} = a_{i,j,k} r_{i,j,k-1} \tag{13.22}$$

$$\phi^3_{i,j,k} = d_{i,j,k} h_{i,j-1,k} \tag{13.23}$$

$$\phi^4_{i,j,k} = f_{i,j,k} r_{i-1,j,k} \tag{13.24}$$

$$\phi^5_{i,j,k} = d_{i,j,k} v_{i,j-1,k} \tag{13.25}$$

$$\phi^6_{i,j,k} = f_{i,j,k} v_{i-1,j,k} \tag{13.26}$$

The above formulas can be used to solve both scalar and coupled equations. For a scalar equation, they can be used as the form given in the above formulas. For coupled equations, the extension is very straightforward. All the quantities in the formulas become 4×4 matrices (say for four coupled equations in the present study). The quantity 1 becomes an identity matrix and α becomes a diagonal matrix with α being the diagonal element. All multiplications become matrix-matrix multiplications.